



Title	Multi-sensor study of dynamics of atmospheric waves induced by volcanic eruptions
Author(s)	中島, 悠貴
Citation	北海道大学. 博士(理学) 甲第13139号
Issue Date	2018-03-22
DOI	10.14943/doctoral.k13139
Doc URL	<a href="http://hdl.handle.net/2115/69524">http://hdl.handle.net/2115/69524</a>
Type	theses (doctoral)
File Information	Yuki_Nakashima.pdf



[Instructions for use](#)



北海道大学  
HOKKAIDO UNIVERSITY

# Multi-sensor study of dynamics of atmospheric waves induced by volcanic eruptions

(複数センサーで探る火山噴火に伴う大気波動のダイナミクス)

by

Yuki NAKASHIMA

(中島 悠貴)

A thesis submitted in partial fulfillment for the  
degree of Doctor of Philosophy

in the

Graduate School of Science

Department of Natural History Sciences

Division of Earth and Planetary Dynamics

March 2018



# 要旨

中島 悠貴

本論文では、上空約 300 km を中心に分布する電離圏の電子数擾乱を GNSS-TEC 法で解析した結果を軸に、火山噴火に伴う超低周波波動の伝搬について論じる。

おおよそ 10 mHz よりも低い周波数の大気波動は地表から約 300 km 上空の電離圏まで到達し、電離大気を揺さぶることがある。例えば、地震は地動や津波ばかりでなく、大気の擾乱も引き起こす。地震による大気の擾乱には、超低周波音そのものによるもの、地震動による音響重力波やレイリー波とカップリングするもの、津波とカップリングした大気重力波など様々な動態が確認されている。火山噴火に伴うと考えられる電離圏擾乱は、大気重力波の重力波モードや音響モードによる波動、爆発音のうちのとくに低い周波数のものが現れたと考えられるものが報告されてきた。

修士論文では、2014 年ケルト火山噴火に伴う電離圏擾乱について論じた。博士課程では 2015 年口永良部島火山噴火に伴う電離圏擾乱を GNSS-TEC 法で検出すると同時に、地震計や微気圧計の波形を解析し、比較する機会を得ることができた。この 2 つの噴火で引き起こされた電離圏擾乱は違った様相を見せる。2014 年ケルト火山噴火では、いくつかの周波数成分を持ち数時間程度継続する波動が観測された。これは地震計から推定される地表付近の大気擾乱と概ねよく対応していた。2015 年口永良部島火山噴火では、パルス状の波動と約 5 mHz の 15 分程度続く波動が観測された。地上の観測と比較すると、パルス状の波動は地表で観測された気圧変動と同等のものであることがわかった。これまでに行ってきた研究と文献を改めて確認しながら、火山噴火に伴う電離圏擾乱の起源・成因と大気下層から超高層までの伝搬の性質について考えた。その結果、これまでに観測されている電離圏擾乱の動態は噴火の経緯とよく対応することがわかった。



# 各章の概要 英文は各章冒頭に記述。

## 第一章 火山噴火が引き起こす地球大気の擾乱

本章では、火山噴火と大気擾乱、電離圏擾乱についてのこれまでの知見を概観する。火山噴火による大気擾乱は音波や音響重力波として伝搬する。火山噴火で引き起こされた超低周波音を使うと夜間に発生した爆発回数を検出したり、爆発的噴火のメカニズムを解き明かすことができる。超低周波音は、地表の微気圧計やマイクロフォンによって収集されている。一方で、上空約 300km を中心に分布する電離圏の変動は、電波による遠隔通信に影響を与えるため、古くから様々な測器で観測されてきた。火山噴火は、この電離圏まで伝搬しうる低い周波数の音波や大気音響重力波を励起する。その波動はしばしば電離圏の各種測器で検出されてきた。

## 第二章 いかにして大気波動を観測するか

GNSS-TEC (Global Navigation Satellite System Total Electron Content; 全地球衛星測位システム電離圏全電子数)、広帯域地震計、微気圧計の基本的な取り扱い方や調査の際に使ったデータ解析手法を紹介する。GNSS-TEC 法では、電離圏中電子の多寡に応じて、周波数の異なるマイクロ波同士の分散性速度遅延量の差が変動する性質を利用する。算出される量は TEC と呼ばれ、衛星視線に沿って数えた電離圏中に存在する電子の数に相当する。実際上は GNSS 衛星の発する複数周波数電波同士の位相差から算出する。ここでは同時に、実際に今回の調査で行った、広帯域地震計の波形から気圧波動由来の信号を取り出す手法について紹介する。

## 第三章 火山噴火により励起された大気擾乱

主に 2015 年 5 月 29 日 0:59UT に発生した口永良部島火山噴火に伴う大気擾乱を調査した成果について報告する。口永良部島は九州の南約 80km 沖合に位置する、活火山を有する火山島である。GNSS-TEC を得るために国土地理院の展開する GNSS の稠密観測網、GEONET (GNSS Earth Observation Network System) で得られた 1 Hz サンプリングのデータを使用した。地表での観測データとして、防災科学技術研究所が展開している観測網 (F-net・V-net) の広帯域地震計・微気圧計と産業技術総合研究所の微気圧計データを使った。本章では口永良部島の事例に加えて 2014 年 2 月のケルト火山噴火と 2015 年 4 月のカルブコ火山噴火に伴い発生した大気擾乱の成果についても紹介する。

## 第四章 電離圏へ届く火山噴火に起因する大気擾乱の特徴

第三章で紹介した解析結果から、火山噴火に伴う大気擾乱の特徴や励起機構について考える。火山噴火に伴う電離圏擾乱には様々な周波数・波形を持つものが含まれている。火山近傍での電離圏 TEC に生じる擾乱の波形は大きく 2 つに分けられた。一つは火山爆発の約十分後に生じる数分の時間スケールを持つ N 型の波形の変動で、2004 年の浅間山噴火や 2011 年の霧島山新燃岳の噴火で観測された。もう一つは、連続的な火山噴火に伴って生じる特定の周期で長時間継続する波動で、2014 年のケルト火山や 2015 年のカルブコ火山の噴火に伴い確認されている。2015 年の口永良部島火山の噴火では、前者に相当する特徴に加えて、 $\sim 5$  mHz の TEC 振動が 15 分程度継続する様子が検出された。

## 第五章 火山噴火に伴う電離圏擾乱を考える

本章では、火山噴火に伴う電離圏擾乱に関して、本論文全体で論じた項目をまとめ、結論と今後の展望について記した。

# Abstract

by Yuki NAKASHIMA

I discuss the propagation of very low frequency infrasound that come from volcanic eruptions from near surface to the ionosphere based on the observations of GNSS-TEC, broadband seismometers and barometers.

Infrasound or some other atmospheric wave under  $\sim 10$  mHz can reach to the ionosphere and shake the ionized atmosphere. For example, a great earthquake induces not only ground motions or tsunamis but also atmospheric perturbations and some of them propagate upward to the ionosphere. Such waves are interpreted as the acoustic modal wave, the tsunamigenic gravity wave or the atmospheric wave coupled to the seismic Rayleigh wave. Ionospheric perturbations by volcanic eruptions are also sometimes reported.

In my master thesis written in 2015, I discussed the ionospheric disturbances made by the 2014 Kelud volcano eruption. It induced acoustic trap mode by continuous eruption.

In the thesis, I would introduce the investigation about the propagation of the atmospheric disturbance by the 2015 Kuchinoerabujima eruption. I analyzed 1 Hz sampled GNSS-TEC time series, broadband seismograms and barograms installed around the volcano. The features of the ionospheric disturbances observed in the two case are totally different. I can confirm again with more assurance that the difference comes from the sequence of the volcanic eruptions.

# Acknowledgements

I would like to show my sincere gratitude to all of the people who encouraged and advised me in the course of my study.

First of all, I would like to express my hearty appreciation to Prof. Kosuke Heki. He has given me many great advise, always encouraged me, and allowed me to attend various conferences since I came to one of the members of the space geodesy laboratory in Hokkaido University.

I express my sincere gratitude to Dr. Kiwamu Nishida, Dr. Yosuke Aoki and Dr. Akiko Takeo in the Earthquake Research Institute of the University of Tokyo. Dr. Mokhamad Nur Cahyadi in Institute of Technology Sepuluh Nopember and Dr. Arif Aditiya in Geospatial Information Authority of Indonesia (BIG) help me to investigate Indonesian GNSS data. Dr. Kazunori Yoshizawa also helped me. Dr. Giovannni Occhipinti in Institute de Physique du Globe de Paris sometimes discussed my investigation and encouraged me.

My sincere appreciation goes to Prof. Junji Koyama, Prof. Kiyoshi Yomogida, Prof. Masato Furuya and Dr. Yoichiro Takada. I would like to thank the students and the post-doctoral fellows joining to the solid earth science seminar of Hokkaido University in the last six years. They talked about various topics with me and encouraged me.

I express my sincere gratitude to the Geospatial Survey Information Authority of Japan (GSI), the Geospatial Survey Information Authority of Indonesia (BIG), the National Research Institute for Earth Science and Disaster Resilience (NIED), the National Institute of Advanced Industrial Science and Technology (AIST) and the Japan Meteorological Agency (JMA). GSI provided GNSS data collected by GNSS Earth Observation Network System (GEONET). BIG provided GNSS data in Indonesia. NIED provided broadband seismometers and barometers data. AIST provided barometers data. JMA provided microphone data. Also, Instituto Geográfico Nacional de la República Argentina (IGN) provided GNSS observation

data collected by Red Argentina de Monitoreo Satelital Continuo (RAMSAC). I also express my hearty appreciation to that. Section 3.1 is already published as [Nakashima et al \(2016\)](#).

I show my warm gratitude to the Japan Society for the Promotion of Science (JSPS), the Japan Student Services Organization (JASSO) and my parents. JSPS supported me 200,000 yen each month as living cost and about 2,800,000 yen as the research grant in my doctoral course. JASSO lent me 50,000 yen each month in the master course and released me from the payback after I graduated to the course. My parents gave me the continuous support until I got the master degree. Besides, After I started to study in the doctoral course, they also supported me financially for some occasional events.

# Contents

要旨	iii
各章の概要	iv
Abstract	vi
Acknowledgements	vii
Contents	ix
<b>1 Atmospheric disturbances excited by near-surface phenomena</b>	<b>1</b>
1.1 Introduction to ultra low-frequency atmospheric waves . . . . .	2
1.2 Atmospheric waves induced by volcanic eruptions . . . . .	4
1.2.1 The 1883 Krakatau eruption, Indonesia . . . . .	10
1.2.2 The 1980 St. Helens eruption, the USA . . . . .	10
1.2.3 The 1982 El. Chichón eruption, Mexico . . . . .	10
1.2.4 The 1991 Pinatubo eruption, Philippine . . . . .	11
1.2.5 The 2003 Soufrière Hills volcano eruption, Montserrat . . . .	12
1.2.6 The 2004 Asama eruption, Japan . . . . .	13
1.2.7 Explosive eruption style: Vulcanian vs Plinian . . . . .	14
1.3 The objectives of the thesis . . . . .	16
<b>2 How to observe atmospheric waves by seismological and space geodetic methods</b>	<b>19</b>
2.1 Detection of waves propagating near the surface . . . . .	20
2.1.1 Barometer observation . . . . .	20
2.1.2 Broadband seismometer observation . . . . .	20
2.2 Detection of atmospheric waves traveling in Ionosphere: GNSS-TEC method . . . . .	22
2.2.1 How to measure the number of electrons by GNSS? . . . . .	22
2.2.1.1 What is GNSS? . . . . .	23

2.2.1.2	GNSS-TEC method . . . . .	27
<b>3</b>	<b>Atmospheric perturbation made by volcanic eruptions</b>	<b>29</b>
3.1	The 2014 eruption of the Kelud volcano, Indonesia . . . . .	30
3.1.1	Seismic data . . . . .	33
3.1.2	GNSS-TEC data . . . . .	37
3.1.3	Discussion and summary . . . . .	38
3.2	The 2015 Calbuco volcano eruption, Chile . . . . .	40
3.2.1	Duration of ionospheric perturbation observed by GNSS-TEC	44
3.2.2	GNSS-TEC frequency components . . . . .	44
3.2.3	Summary of the section . . . . .	45
3.3	Kuchinoerabujima volcano eruption on 29 May 2015 . . . . .	46
3.3.1	Details of the observation . . . . .	47
3.3.2	Near surface atmospheric perturbation . . . . .	50
3.3.2.1	Near-field observation on the ground . . . . .	50
3.3.2.2	Far-field observation on the ground . . . . .	50
3.3.3	Ionospheric perturbation observed by GNSS-TEC . . . . .	52
3.3.4	Interpretation of wave propagation . . . . .	54
3.3.4.1	Multi-sensor travel time . . . . .	54
3.3.4.2	Tomographic image of TEC perturbation . . . . .	56
3.3.4.3	Summary of the section . . . . .	67
<b>4</b>	<b>Features of atmospheric disturbances by volcanic eruptions</b>	<b>69</b>
<b>5</b>	<b>Conclusions</b>	<b>73</b>
	<b>Bibliography</b>	<b>74</b>

# Chapter 1

## Atmospheric disturbances excited by near-surface phenomena

I would introduce previous studies about ionospheric disturbances and atmospheric waves induced by various surface phenomena including volcanic eruptions in this first chapter.

Explosive eruptions excite atmospheric perturbations: not only as audible sound but also as infrasound or acoustic modal wave, internal gravity wave and Lamb wave. Observations of such perturbations enable us to detect volcanic eruptions occurred during the night time, and allow us to investigate the physical processes in various kinds of volcanic eruptions. On the ground, such atmospheric waves have been observed by microphones or barometers.

In this study, I analyze various observation data of atmospheric waves that can be propagating upward to the upper atmosphere, namely the ionosphere. It is the layer rich in ions and electrons located  $\sim 300$  km above the ground. It makes delays of microwave signals from the GNSS (Global Navigation Satellite System) satellites, and it enable us to study ionospheric dynamics. The value detected by GNSS microwave propagation is called TEC (Total Electron Content). It indicates the number of electrons integrated along the line-of-sight connecting satellites and



ground receivers. I use this GNSS-TEC technique to study atmospheric waves excited by volcanic eruptions and propagating in the ionosphere.

## 1.1 Introduction to ultra low-frequency atmospheric waves

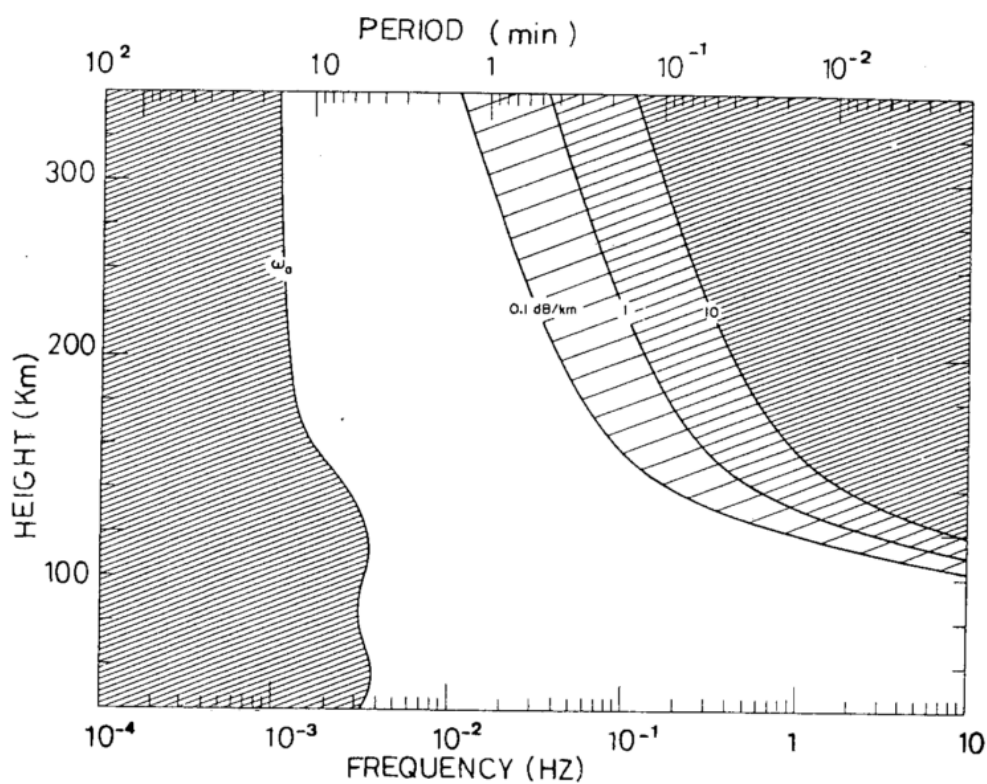


Figure 1.1: Only acoustic waves with frequencies higher than the cut-off frequency can exist. Acoustic waves with frequencies higher than a certain value are highly attenuated by air viscosity. Hence, the Earth's atmosphere works as a band-pass filter (Georges 1968) (cited from [Blanc, 1985](#), Figure 3).

I discuss atmospheric waves excited by volcanic eruptions with frequencies lower than  $\sim 20$  mHz, propagating in the atmosphere. The Earth is composed of the solid part, the ocean and the atmosphere. Majority of such waves propagate within individual layers, and seldom propagate across their boundaries. However,

the lowest frequency atmospheric wave often couples with the other layers, i.e., the solid earth, the ocean, and the upper atmosphere. Atmospheric waves are roughly divided into three categories, acoustic waves, the Lamb waves, and internal gravity waves. Below I briefly introduce their characteristics.

At first, I introduce acoustic waves. I mainly discuss this with ultra-low frequencies often called infrasound. [Blanc \(1985\)](#) summarized the decay of infrasound waves propagating upward from the surface. Figure 1.1 showed that the higher frequency components decay more due to air viscosity, and hardly reach the ionosphere. As for the lowermost frequency waves, acoustic cut-off frequency determines the lower boundary of the frequency reaching the ionosphere. This cut-off occurs because the atmospheric elasticity does not work efficiently as the restoring force for frequencies below a certain threshold; thus, the atmosphere serves as a “band-pass” filter for acoustic waves.

Below this acoustic cut-off frequency, waves in the atmosphere take another form, i.e., internal gravity waves. The restoring force of the internal gravity wave is the atmospheric buoyancy, and its upper-limit frequency of the gravity wave domain is called the Brunt-Väisälä frequency. It indicates the frequency of oscillation by buoyant forces in a stratified fluid, and is often called “buoyancy frequency.”

Between the internal gravity and the acoustic wave domains exists the Lamb wave. It can propagate over a long distance and is occasionally detected by far-field observations after huge volcanic explosions (e.g. [Kanamori et al, 1984](#)).

Such internal gravity waves often couple mechanically with the ocean. For example, there have been reports about tsunamigenic ionospheric disturbances (e.g. [Occhipinti et al, 2008](#)). Volcanic eruptions can also excite tsunami when pyroclastic flow goes into the ocean. The 1883 Krakatau volcano eruption was one of the most explosive eruptions ever recorded in the world (e.g. [Strachey, 1983](#)), and atmospheric internal gravity wave observed after this eruption is considered to have been induced by oceanic gravity wave.

Such atmospheric waves sometimes exert forces perpendicular to the surface of the

solid earth and excite a particular kind of seismic surface waves, i.e., the Rayleigh waves. Large air pressure changes sometimes make observable solid earth displacements, and a few acoustic modes efficiently couple with seismic modes with similar frequencies. Such coupling let these modes be continuously excited by meteorological and oceanographic sources, which is widely recognized as the ambient seismic hum or the Earth's background free oscillations (e.g. [Nishida et al, 2000](#)). Acoustic and internal gravity waves often propagate far upward and disturb the ionosphere. Such resonant oscillations of the lower atmosphere are also observed by GNSS-TEC after large earthquakes. [Choosakul et al \(2009\)](#) reported that the 2004 Sumatra-Andaman earthquake excited  $\sim 4$  mHz oscillation in the ionosphere lasting for hours. [Rolland et al \(2011\)](#) analyzed various types of ionospheric perturbations by the 2011 Tohoku-Oki earthquake. It includes an N-shaped wave excited by the Rayleigh wave, and the 3.7 mHz and 4.4 mHz acoustic-trap-modes excited in the lower atmosphere and leaked into the ionosphere. Then, the internal gravity wave appeared  $\sim 45$  min later and propagated concentrically outward by  $\sim 225$  m/s from the epicenter. [Saito et al \(2011\)](#) detected 3.7 mHz, 4.5 mHz, and 5.3 mHz frequency peaks in the TEC changes. [Nishioka et al \(2013\)](#) reported internal gravity waves and the lower atmospheric trapped waves excited by the 2013 Moore EF5 tornado.

These examples are found in a comprehensive review of atmospheric waves excited by volcanic eruptions and large earthquakes up to 2010 by [Mikumo \(2011\)](#).

## 1.2 Atmospheric waves induced by volcanic eruptions

Volcanic eruptions cause large pressure changes and they can travel as air waves. They have been recorded by various kinds of sensors ([Fee and Matoza, 2013](#),

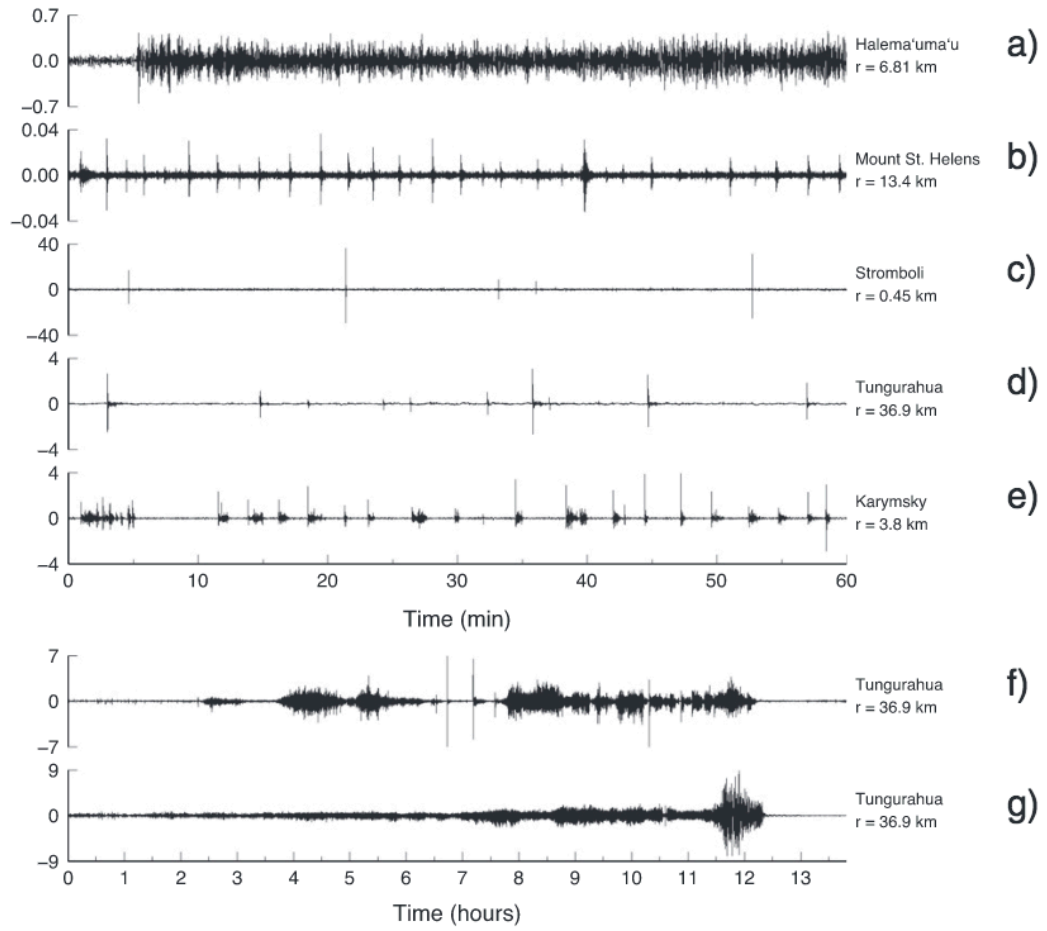


Figure 1.2: Comparison of waveforms of infrasound excited by various kinds of volcanic eruptions, from Hawaiian to Plinian. Vertical axis indicates air pressure (Pa). The distances between volcanoes and sensors ( $r$ ) are given to the right of the waveform. a) 0.1–15 Hz harmonic tremor from the Halema’uma’u Vent, Kilauea Volcano, Hawaii. The tremor begins with an impulsive degassing burst that cleared the vent (Fee et al., 2010a). b) Infrasound pulses associated with LP seismic “drumbeat” events at Mount St. Helens, North America. The events have durations of  $\sim 10$  seconds (Matoza et al., 2009b). Strombolian activity from c) Stromboli Volcano, Italy (Ripepe and Marchetti, 2002), and d) Tungurahua Volcano, Ecuador. Harmonic tremor follows several of the Tungurahua explosions for a couple to tens of minutes (Fee et al., 2010b). e) Complex explosion waveforms from Karymsky Volcano, Kamchatka, Russia. Although the signals could be classified as strombolian, the waveforms are asymmetric and characterized by larger initial compression pulse, smaller subsequent rarefaction pulse, and long-duration sequences possibly due to jetting. f) Subplinian eruption from Tungurahua Volcano showing occurrences of multiple pulses of sustained broadband infrasound, intermixed with large discrete explosions (Matoza et al., 2009a; Fee et al., 2010b). g) Subplinian–Plinian eruption of Tungurahua Volcano, Ecuador. Sustained, broadband, high-amplitude infrasound gradually builds and peaks near hour 11.75 with a  $\sim 45$  minutes paroxysmal Plinian phase (Matoza et al., 2009a; Fee et al., 2010b). Note a–e) represent one hour of data, while f–g) represent 14 hours. (cited from [Fee and Matoza, 2013](#), Figure 2)

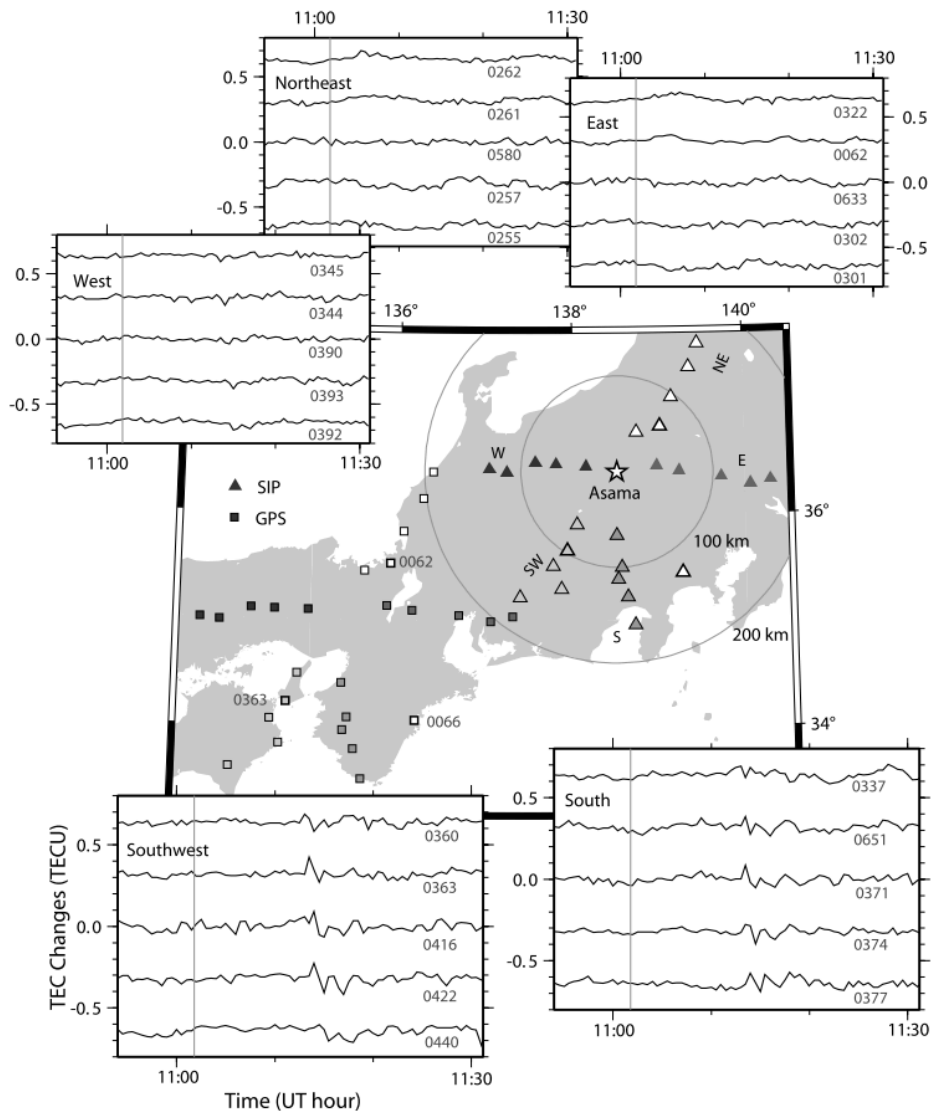


Figure 1.3: Time series of slant TEC (residuals from reference curves, Sat. 15 was used) observed at GPS receivers (squares). Triangles show the ground projections of the ionosphere (height is assumed to be 300 km) piercing points in different azimuths from the Asama volcano indicated as an open star. Clear disturbances are found in southern and southwestern stations about 10 minutes after the eruption (11:02, vertical gray lines). They are less conspicuous in the western stations and absent in northeastern and eastern stations. Numbers in the time series are the station IDs in four digits. TEC time series closer to the volcano are displayed at the top and bottom of the figure. (cited from [Heki, 2006](#), Figure 1)

Figure 1.2). Among others, I focus on a series of investigations about the “bichromatic” seismic waves induced by two huge eruptions ( $> \text{VEI } 5$ ) occurred during 1980s and 1990s.

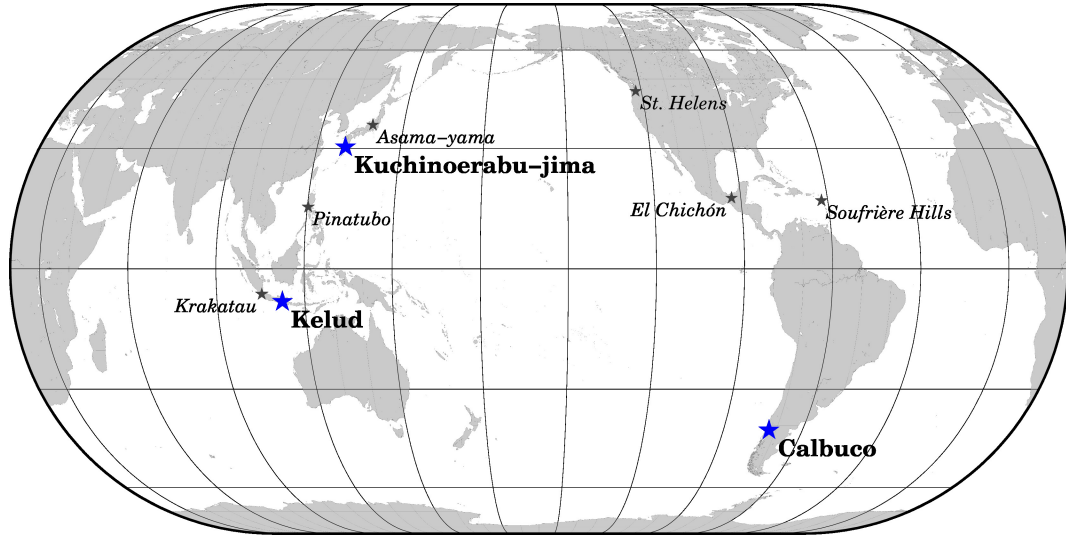


Figure 1.4: Map of volcanoes induced ultra low frequency atmospheric wave.

Table 1.1: Examples of past eruptions with records of ionospheric perturbations. VEI (Volcanic Explosivity Index) is a semi-quantitative scale of explosivity of volcanic eruptions (VEI is cited from [Global Volcanism Program, 2013](#)).

Date	Volcano	VEI
2015/5/29	Kuchinoerabujima	3
2015/4/22–23	Calbuco	4
2014/2/13	Kelud	4
2004/9/1	Asama	2
2003/7/13	Soufrière Hills	3
1991/6/12	Pinatubo	6
1982/4/4	El Chichón	5
1980/5/18	St. Helens	6
1883/8/27	Krakatoa	6

Table 1.2: Previous detection of ionospheric perturbations by volcanic eruptions after GNSS construction. TEC (F) means TEC calculated from Faraday rotation and TEC (D) means TEC calculated from phase difference of GNSS dual carrier wave.

Report	Event	Instruments
<a href="#">Shults et al (2016)</a>	2015 Calbuco	TEC (D)
<a href="#">Aoyama et al (2016)</a>	2015 Calbuco	SWARM (geomag.)
<a href="#">Nakashima et al (2016)</a>	2014 Kelud	TEC (D), Seis.
<a href="#">Dautermann et al (2009b)</a>	2003 Soufrière Hills	TEC (D), Strain
<a href="#">Dautermann et al (2009a)</a>	2003 Soufrière Hills	TEC (D)
<a href="#">Heki (2006)</a>	2004 Asama	TEC (D)
<a href="#">Igarashi et al (1994)</a>	1991 Pinatubo	HF, Baro., TEC (F)
<a href="#">Cheng and Huang (1992)</a>	1991 Pinatubo	HF, TEC (F)
<a href="#">Ogawa et al (1982)</a>	1980 St. Helens	HF, TEC (F)
<a href="#">Roberts et al (1982)</a>	1980 St. Helens	TEC (F)
<a href="#">Roberts and Rogers (1982)</a>	1980 St. Helens	VLBI
<a href="#">Liu et al (1982)</a>	1980 St. Helens	Baro, HF, TEC (F)

TEC (F): TEC using Faraday rotation

TEC (D): GNSS-TEC

Table 1.3: Previous detection of ultra low frequency atmospheric wave by volcanic eruptions mainly observed on the ground.

Report	Event	Instruments
<a href="#">Watada and Kanamori (2010)</a>	1991 Pinatubo	Seis.
<a href="#">Kanamori et al (1994)</a>	1991 Pinatubo, 1982 El. Chichón, 1980 St. Helens	Baro., Seis.
<a href="#">Kanamori and Mori (1992)</a>	1991 Pinatubo	Seis.
<a href="#">Widmer and Zürn (1992)</a>	1991 Pinatubo, 1982 El. Chichón	Grav.
<a href="#">Delclos et al (1990)</a>	1980 St. Helens	others
<a href="#">Mikumo and Bolt (1985)</a>	1980 St. Helens	others
<a href="#">Bolt and Tanimoto (1981)</a>	1980 St. Helens	Baro.
<a href="#">Donn and Balachandran (1981)</a>	1980 St. Helens	Seis., Baro.
<a href="#">Harkrider and Press (1967)</a>	1883 Krakatau	Tide-gauge
<a href="#">Press and Harkrider (1966)</a>	1883 Krakatau	Tide-gauge

Seis.: Broadband seismometer

Baro.: Barometer



### 1.2.1 The 1883 Krakatau eruption, Indonesia

Krakatau volcano is located between the Sumatra and the Java Islands, Indonesia (Figure 1.4). Its 1883 eruption is known as the “Ultra-Plinian” eruption and people located more than 5,000 km away could hear the sound associated with the eruption (e.g. [Strachey, 1983](#)). There have been reports by [Press and Harkrider \(1966\)](#) and [Harkrider and Press \(1967\)](#) of the coupling between the atmospheric modes and ocean recorded by tide gauges.

### 1.2.2 The 1980 St. Helens eruption, the USA

Mt. St. Helens is located between Seattle and Portland, western USA (Figure 1.4). Its explosive eruption on May 18, 1980, made a caldera with diameter of 1.5 km, and its peak altitude decreased from 2,950 meters to 2,550 meters. [Delclos et al \(1990\)](#) detected infrasound from the eruption in far-field. There are reports of the detection of seismic Lamb wave ([Kanamori et al, 1984](#)), atmospheric waves were observed in Japan as disturbances of the ionosphere ([Ogawa et al, 1982](#)). Ionospheric disturbances have also been detected as changes in ionospheric delay of microwave by VLBI (Very Long Baseline Interferometry) as reported in [Roberts et al \(1982\)](#) and [Roberts and Rogers \(1982\)](#).

### 1.2.3 The 1982 El. Chichón eruption, Mexico

El Chichón is an active volcano located in southern Mexico (Figure 1.4). Its disastrous 1982 eruption caused over 2,000 casualties. Large mass of aerosol released to the stratosphere is considered to have temporarily cooled down the Earth for 0.3–0.5 degrees. In this eruption, there are reports of harmonic oscillation caused by the atmospheric modes recorded by seismometers ([Kanamori et al, 1994](#)) and

gravimeters ([Widmer and Zürn, 1992](#)). Ionospheric disturbances by this eruption are also reported in [Cheng and Huang \(1992\)](#).

#### 1.2.4 The 1991 Pinatubo eruption, Philippine

The Pinatubo volcano is located in the western part of the Luzon Island, Philippines (Figure 1.4). Its 1991 June eruption is known as one of the largest volcanic eruptions in the twentieth century, and is considered to have decreased the world average temperature by 0.5 degrees by blocking the sunlight with huge amount of aerosols put into the stratosphere. This eruption also left unique geophysical records for various kinds of sensors. [Widmer and Zürn \(1992\)](#) found some modal waves in the gravity record of black forest observatory. Atmospheric resonance induced the seismic signals by the 1991 Pinatubo eruption as well as the 1982 El Chichón eruption. They found strong “air waves”, and the same waves are detected by the world-wide broadband seismometer arrays ([Kanamori and Mori, 1992](#)). [Kanamori et al \(1994\)](#) proposed the two physical mechanisms behind the observed seismic signatures, i.e. the “mass injection” and “energy injection” into the atmosphere by the eruptions. [Watada and Kanamori \(2010\)](#) investigated atmospheric resonance induced by volcanic eruptions from theoretical consideration, and succeeded in explaining the seismic observations in the 1991 Pinatubo eruption using normal mode theory.

Lower frequency ionospheric disturbances by this eruption ( $\sim 1000$  sec) have been reported by the observations in Taiwan ([Cheng and Huang, 1992](#)) and in Japan [Igarashi et al \(1994\)](#). The ionospheric wave propagated with lower atmospheric perturbation as internal gravity wave about 4000 km away from the volcano.

### 1.2.5 The 2003 Soufrière Hills volcano eruption, Montserrat

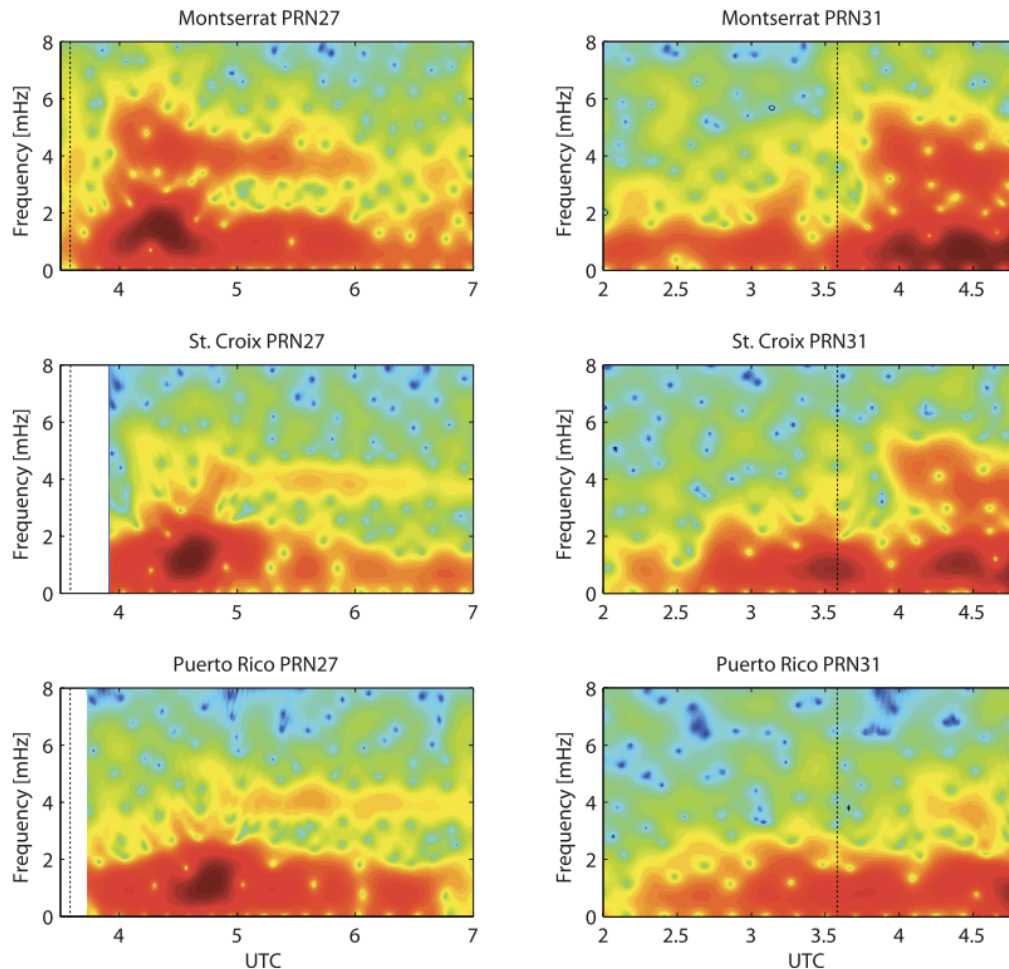


Figure 1.5: Spectrograms of TEC traces stacked by groups of neighboring GPS stations: top = HERM, SOUF, and MVO1 on Montserrat, middle = CRO1 on St. Croix, and bottom = UPRR and UPRH on Puerto Rico. Left spectrograms correspond to satellite PRN27; right, to PRN31. The vertical dotted line indicates the SHV explosion time. The moveout and fade-out of the perturbation at  $\sim 4$  mHz is visible. (cited from [Dautermann et al, 2009b](#), Figure 7).

[Dautermann et al \(2009b,a\)](#) reported ionospheric disturbance using GPS-TEC technique for the 2003 eruption of the Soufrière Hills volcano, Montserrat, Western Indies. They showed continuing TEC oscillation with periods around 4–5

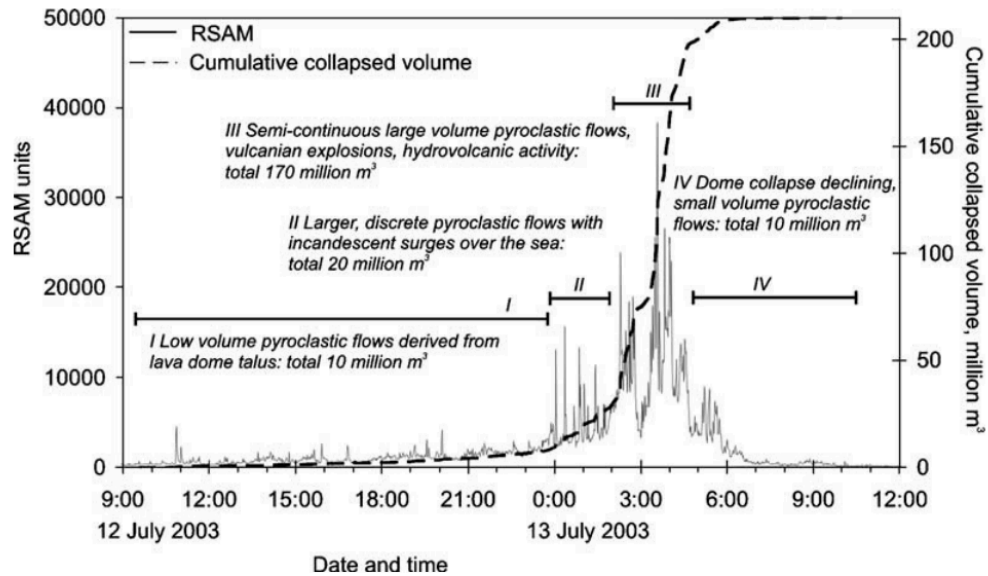


Figure 1.6: RSAM and cumulative volume collapsed over time for the lava dome collapse 12–13 July 2003, showing the various stages of the lava dome collapse. (cited from [Herd et al, 2005](#), Figure 11).

minutes (Figure 1.5). They compared the results with synthetic wave signatures obtained by the normal mode summation, and discussed the lithosphere-atmosphere-ionosphere coupling with GPS-TEC and strainmeter data. [Herd et al \(2005\)](#) investigated the volcano activity by in situ observations (Figure 1.6). They mentioned Soufrière Hills volcano induced tsunami in the Tar River Valley and after that the hydrovolcanic eruption occurred at Soufrière Hills volcano about 2.7 hours.

### 1.2.6 The 2004 Asama eruption, Japan

[Heki \(2006\)](#) presented ionospheric disturbance by a Vulcanian explosion of the Asamayama volcano in 2004 by analyzing the GPS-TEC data. He detected an N-shaped GPS-TEC signal excited by the 2004 explosion of the Asama volcano. The peak-to-peak period of the N-shaped disturbance is  $\sim 120$  sec, although the original GNSS data are 30 sec sampling interval and we cannot discuss signals with periods shorter than 60 sec (Nyquist frequency). He also estimated the acoustic

energy of the explosion from the amplitudes of the ionospheric perturbations by comparing it with the GPS-TEC signals cause by a mine blast with a known amount of explosion energy. The N-shaped signal is similar to ‘shock acoustic waves (SAWs)’ ([Afraimovich et al, 2001](#)), and the signal is considered to come from the atmospheric wave excited by the volcanic explosion. [Ohminato et al \(2006\)](#) suggested that this eruption had an abnormally large amplitude air waves in spite of moderate seismic signatures.

### 1.2.7 Explosive eruption style: Vulcanian vs Plinian

Volcanic eruptions are classified into several styles. Volcanologists have tried to classify volcanic eruption styles by some parameters representing the phenomena. One of such classifications, advocated by [Walker \(1973\)](#), uses “dispersal” and “fragmentation” (see Figure [1.7a](#)). The parameters are calculated by pyroclastic fall deposit. Dispersal and fragmentation almost relate to explosiveness and eruption column height, respectively (see Figure [1.7b](#)). Hawaiian, Strombolian and Plinian eruptions are stationary magma eruptions in the ascending order of explosivity. The most explosive eruption style in them, Plinian eruption, is explosive eruptions continuing several hours, and it makes high plume column and transmits volcanic ash to the stratosphere. Vulcanian eruption is unsteady eruption and explosive relative to the eruption products. Surtseyan and Phreatoplinian eruptions are also called “phreatomagmatic eruption” and occurred by interaction of magma and water.

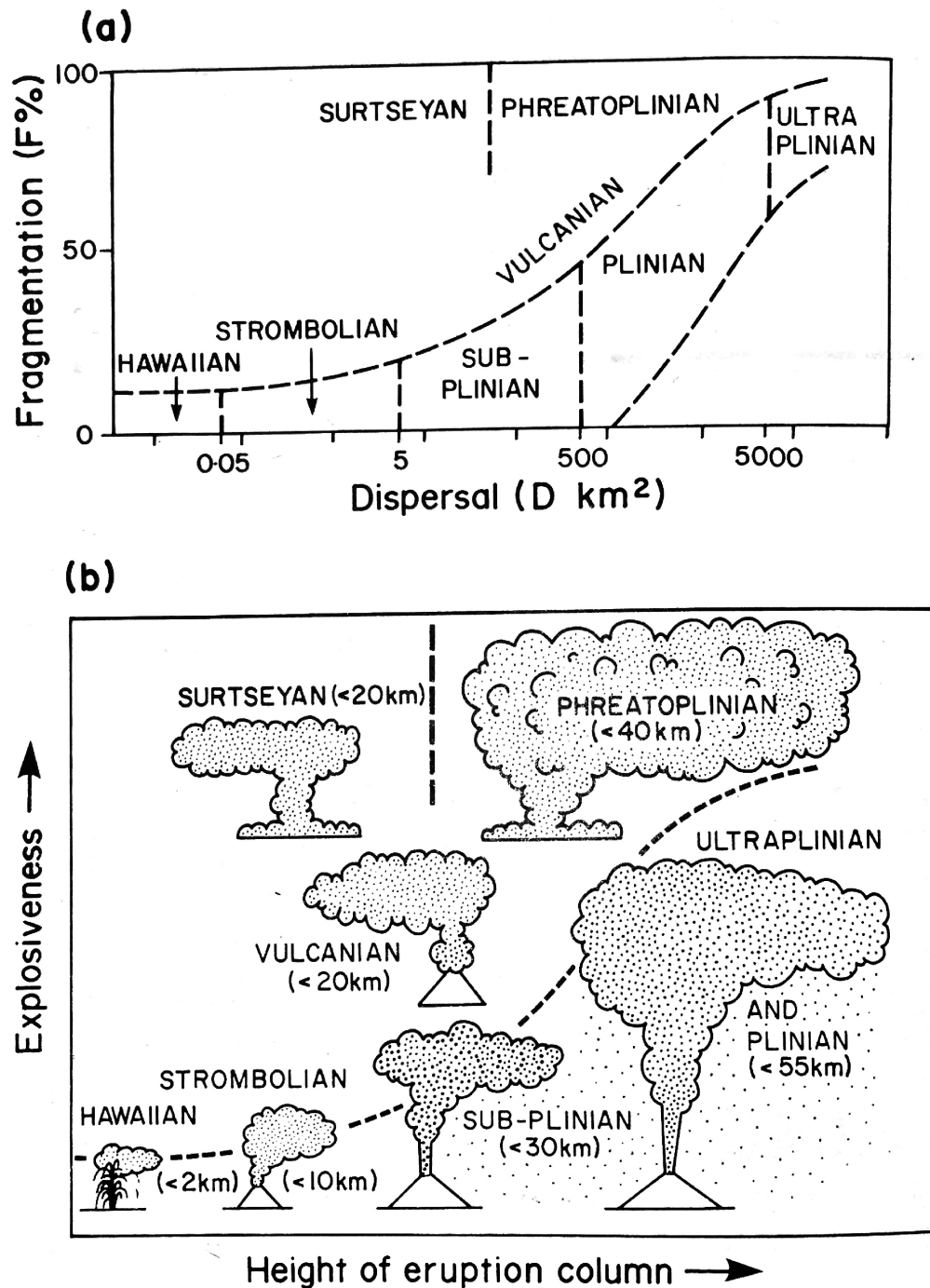


Figure 1.7: (a) D–F plot used to characterise different types of pyroclastic fall deposit (after Walker (1973), and updated in Wright et al. 1980). (b) Cartoon explaining D–F plot in terms of eruption column height and 'explosiveness'. (cited from Cas and Wright, 1987, p.130 Figure 6.2)

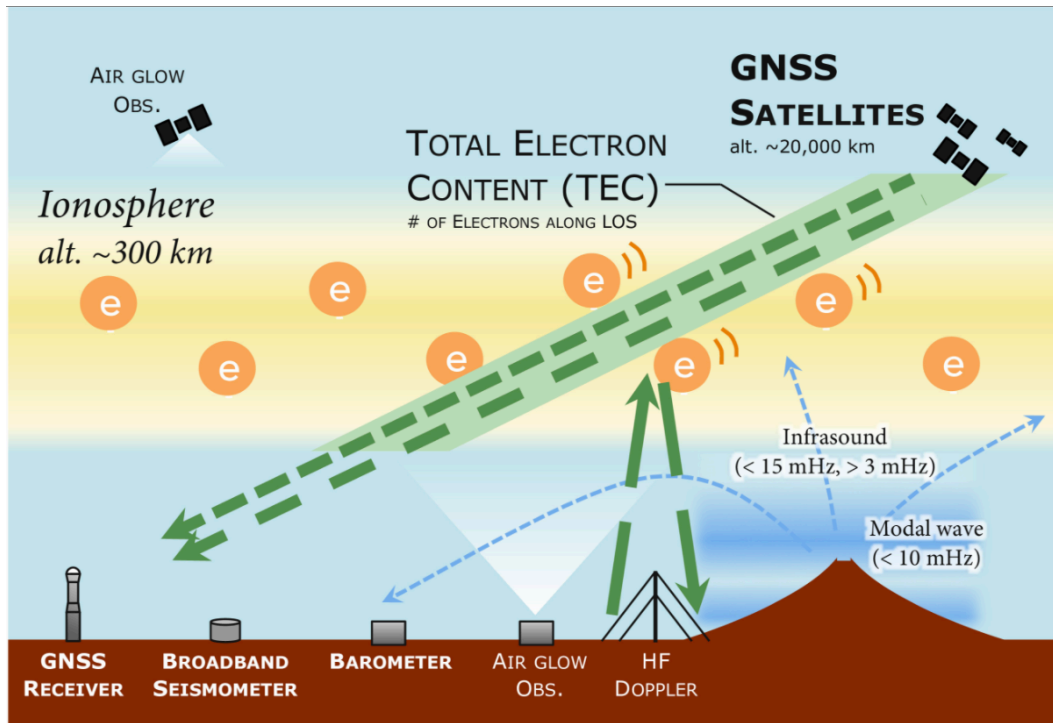


Figure 1.8: Scope of the thesis. A volcanic eruption can induce various atmospheric perturbations and they can be detected by various instruments.

## 1.3 The objectives of the thesis

The objectives of the thesis are as follows:

1. To compile past reports of ionospheric perturbations by large volcanic eruptions, and discuss their common features and differences
2. To analyze GNSS-TEC data of Plinian eruptions, i.e., the 2014 eruption of the Kelud volcano, Indonesia, and the 2015 eruption of the Calbuco volcano, Chile
3. To analyze GNSS-TEC data of Vulcanian eruptions, i.e., the 2015 eruption of the Kuchinoerabujima volcano, Japan

4. To compare GNSS-TEC records by the 2015 eruption of the Kuchinoerabujima volcano with those from multiple conventional sensors such as barometers and broadband seismometers
5. To clarify physical mechanisms of the atmospheric wave excitation and the three-dimensional propagation of such waves in order to understand the disturbance of upper atmosphere due to various kinds of volcanic eruptions in a comprehensive manner





## Chapter 2

# How to observe atmospheric waves by seismological and space geodetic methods

In this chapter, I describe basic procedures to analyze GNSS (Global Navigation Satellite System), the broadband seismometer and the barometer used in the investigation. The main observation techniques is the GNSS-TEC (GNSS Total Electron Contents), where TEC means the number of electrons in the ionosphere along the line-of-sights connecting the GNSS satellites and GNSS receivers. This value is derived from the difference of the GNSS carrier phases between the two microwave carriers. I will also explain the instruments on the ground and how to observe air pressure changes with broadband seismometers.

## 2.1 Detection of waves propagating near the surface

### 2.1.1 Barometer observation

I used arrays of barometers to study the air waves associated with the 2015 Kuchinoerabujima eruption as reported in section 3.2. At first, the most important difference of barometers from microphones is that we can observe low-frequency components, even including the DC (direct current) components.

### 2.1.2 Broadband seismometer observation

The target frequency range of atmospheric waves studied in this thesis is close to the lower corner frequencies of the broadband seismometers. The corner frequencies of STS-1, STS-2 (2.5) and Trillium-240 seismometers are 360 sec, 120 sec, and 240 sec, respectively. I removed the contributions of such frequency-dependent responses from the observed data beforehand.

As introduced in Chapter 1, the atmospheric modes and the solid earth modes can couple with each other. The underlying physical process of such coupling is simple. The increased atmospheric pressure exerts forces perpendicular to the surface and depress the ground. This makes vertical displacement of the surface, and the instruments record such displacements. The response of the solid earth to the atmospheric pressure change is modeled using the following equation ([Ben-Menahem and Singh, 1981](#)).

$$u_z = -\frac{3\hat{c}}{4\omega\lambda'}P_o \quad (2.1)$$

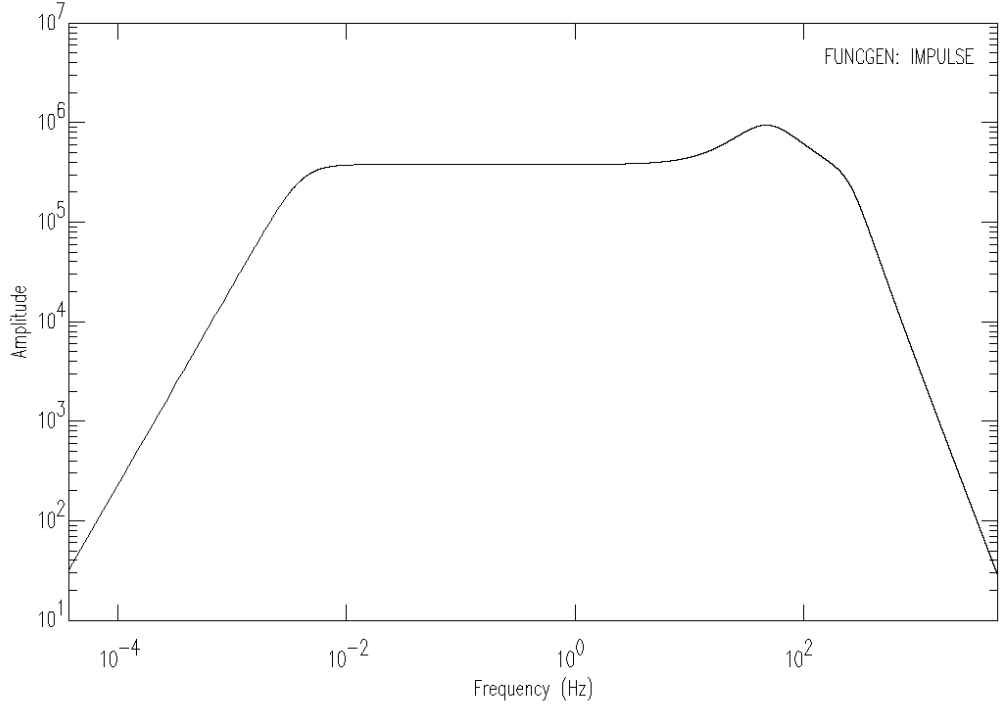


Figure 2.1: Response curve of the Trillium-240 seismometer installed in the V-net stations.

There,  $u_z$ ,  $\hat{c}$ ,  $\omega$ ,  $\lambda'$  indicate vertical displacement, apparent velocity, wave frequency and the Lamé's constant, respectively.  $P_0$  is the change of atmospheric pressure. We confirmed that the deformation obeys this equation using the data collected at a V-net station, KCFV. I input  $\omega = 0.04$  Hz,  $\lambda' = 45$  GPa (PREM),  $\hat{c} = 340$  m/s to the above equation, and obtained the following simplified relationship between the pressure change and vertical crustal displacement:

$$P_o = -0.007u_z \quad (2.2)$$

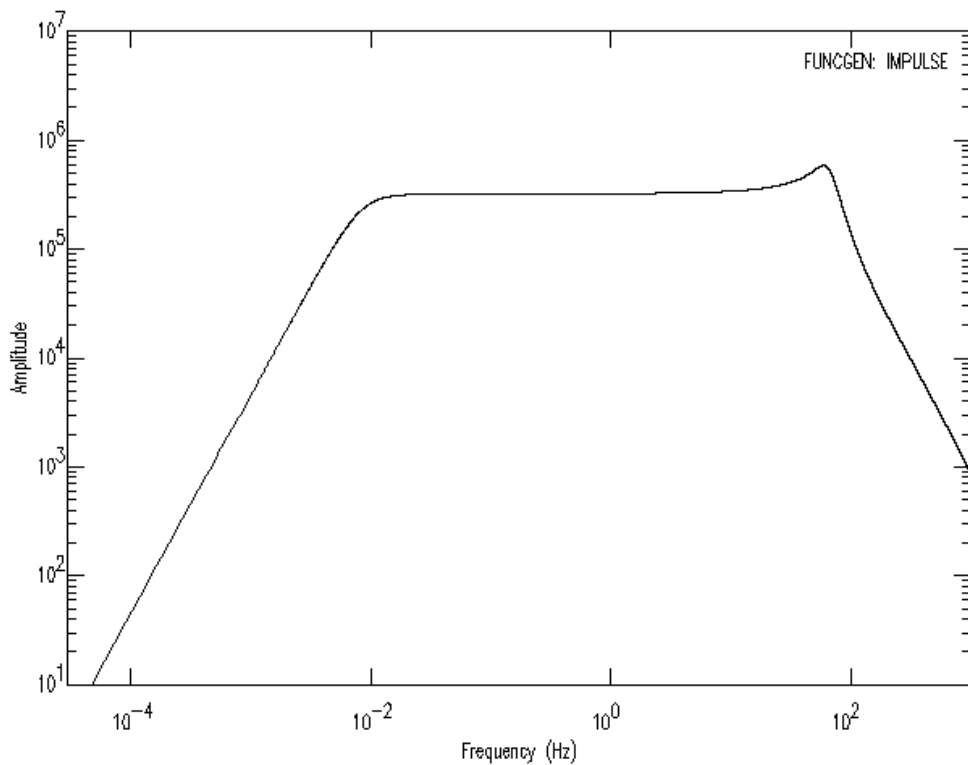


Figure 2.2: Response curve of the STS-2 seismometer installed in the F-net KYK (Nagata, Yakushima island) station

## 2.2 Detection of atmospheric waves traveling in Ionosphere: GNSS-TEC method

GNSS-TEC method is used to measure the number of electrons in the ionosphere. The method utilizes the dispersive nature of microwave signals from GNSS satellites, i.e., the frequency dependence of ionospheric delays.

### 2.2.1 How to measure the number of electrons by GNSS?

GNSS is a system to determine the receiver coordinate by analyzing the code or carrier phase of microwave signals coming from multiple satellites orbiting the Earth. GNSS has been one of the essential infrastructures of not only geophysics

but also surveying in civil engineering over the last several decades. From geophysical point of view, they have become one of the fundamental observation facilities nowadays. Its application field is not limited to positioning, but has expanded to various fields including atmospheric sensing, clock synchronization, precise orbit determination of low earth orbiters, etc.

#### **2.2.1.1 What is GNSS?**

I will briefly explain GNSS and the GNSS-TEC method, a technique to measure TEC, the number of ionospheric electrons integrated along the line connecting a GNSS satellite and a receiver. For details, one can see the RINEX format ICD (Receiver INdependent EXchange format Interface Control Document) (e.g. [IGS and RTCM-SC104, 2012](#)).

#### **GPS** Global Navigation Satellite System

GPS is the first GNSS realized by USA, and had been used as the synonym of GNSS until about 2010.  $\sim 30$  GPS satellites are put into six medium-altitude earth orbits (Figure 2.3). The satellite altitude is 20,000 km and its orbital period is 0.5 sidereal day.

#### **GLONASS** GLObal'naya NAVigatsionnaya Sputnikovaya Sistema

GLONASS is a GNSS operated by the Russian Federation. It was designed independently from GPS over the almost same period, but has not been used widely during 1990s owing to insufficient number of satellites. However, GEONET stations started to track GLONASS satellites after the receiver replacements during 2012, and its importance is growing. GLONASS has several important differences from GPS.

GPS and majority of other GNSS adopt CDMA (Code-Division Multiple Access), which is a technique to identify individual satellites are transmitting microwave signals in the same frequency by using satellite-specific codes.

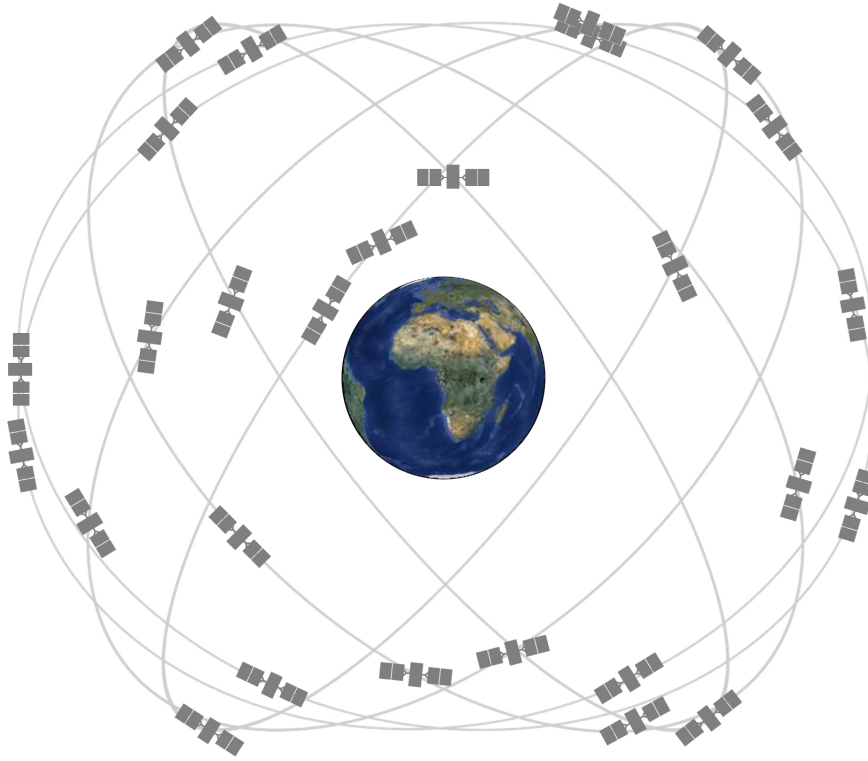


Figure 2.3: GPS constellation image. The GPS space segment has six orbital planes. (The image downloaded from <https://www.gps.gov/multimedia/images/constellation.jpg>)

However, GLONASS adopts FDMA (Frequency-Division Multiple Access) systems to discriminate multiple satellites by frequency differences.

$$f_{G1} = 1602 + k \times 9/16 \text{ (MHz)} \quad (2.3)$$

$$f_{G2} = 1246 + k \times 7/16 \text{ (MHz)} \quad (2.4)$$

There,  $k$  indicates GLONASS frequency number (integer). It is allotted to each GLONASS satellite, and those values could be found in the header of the RINEX observation data file.

## Galileo

Galileo is a GNSS being launched and operated by EU (European Union).

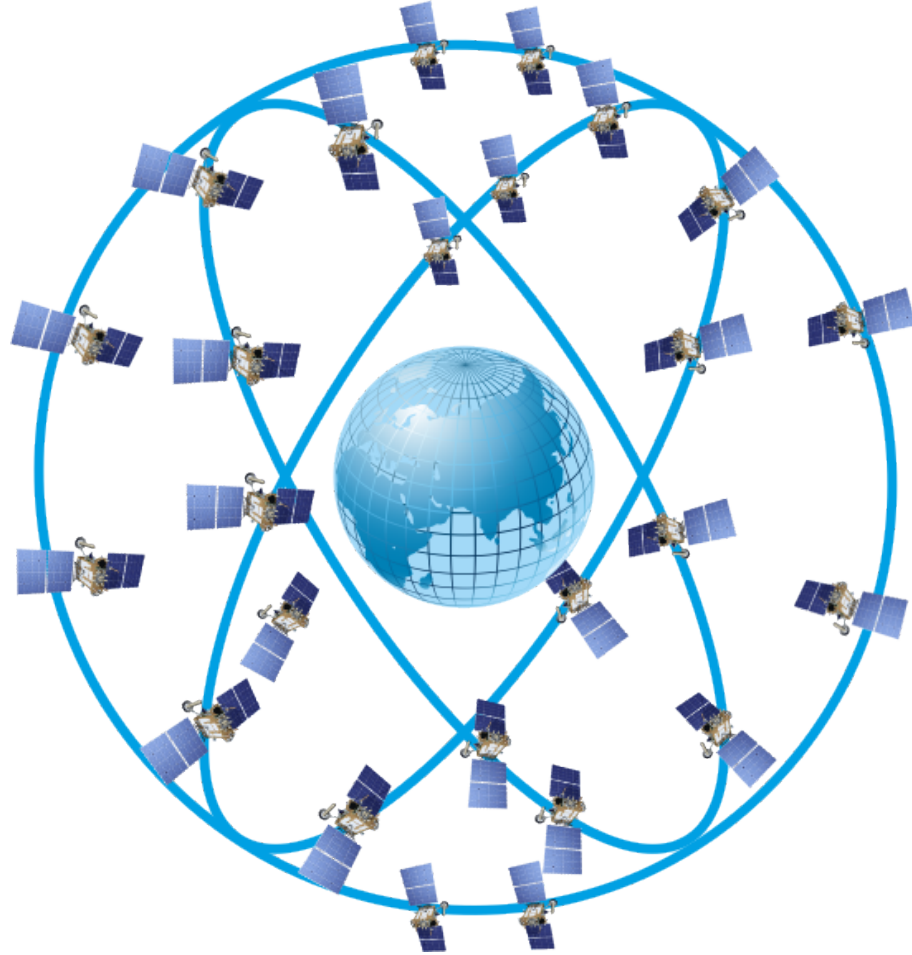


Figure 2.4: GLONASS constellation image. The GLONASS space segment has three orbital planes. (The image is downloaded from <https://www.glonass-iac.ru/guide/gnss/glonass.php>)

In this thesis work, I did not use their data. However, Galileo is expected to occupy an interesting position because of its unique features, e.g. four different carrier wave frequencies. The satellites are in three medium-altitude earth orbits (Figure 2.5). The satellite altitude is about 24,000 km.

### **BeiDou navigation satellite system**

BeiDou is a GNSS operated by China. Its data were not used in this thesis, either. Its space segment (satellites) use three medium-altitude earth orbits, and three satellites are put into the geosynchronous orbit (alt.  $\sim 21,500$  km) (Figure 2.6).





Figure 2.5: Galileo constellation image. (The image is downloaded from <http://www.esa.int/spaceinimages/Images/2000/12/Galileo>)

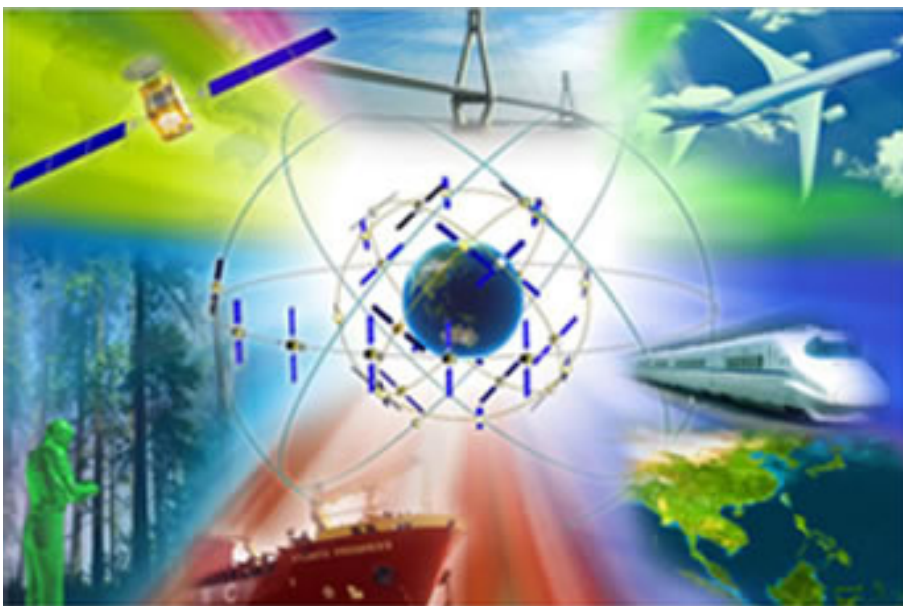


Figure 2.6: BeiDou constellation image. (The image is downloaded from <http://www.beidou.gov.cn/xtjs.html>)

### QZSS Quasi-Zenith Satellite System

QZSS is a navigation satellite system run by the Cabinet Office, the Government of Japan. It is a 'RNSS (Regional Navigation Satellite System),' and includes three quasi-zenith satellites staying near zenith above Japan and one geostationary satellite visible from Japan. The system will be completed in 2018 (Figure 2.7). Quasi-zenith satellites stay over long time periods near zenith (i.e. high elevation angle) of a specific region. The system is optimized for Japan, and we can use the Japanese dense GNSS array, GEONET, to receive their signals. This system is expected to become useful for various kinds of scientific investigations around Japan.

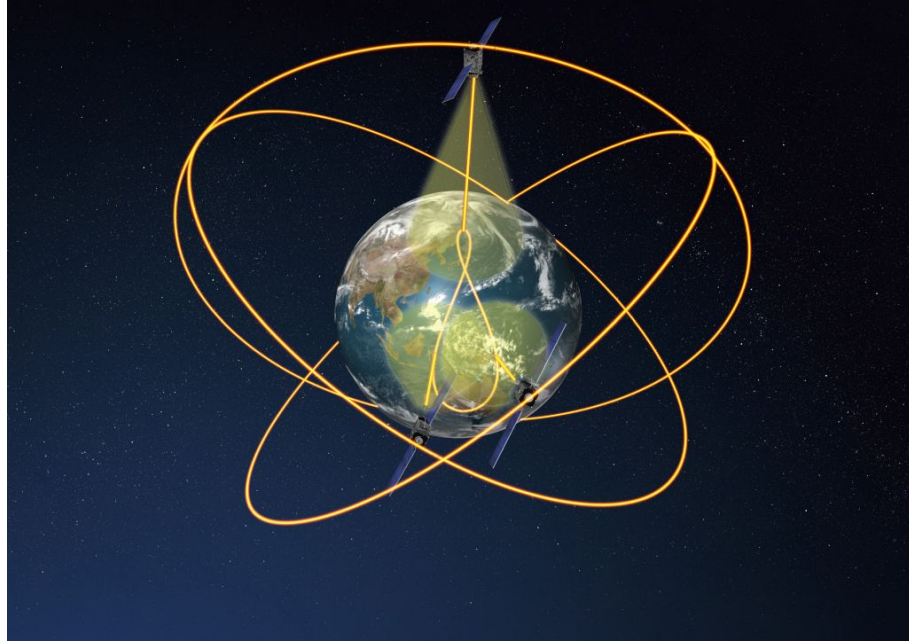


Figure 2.7: QZSS constellation image. The picture indicates just three quasi zenith satellites, but the real QZSS also has one geostationary satellite. (The image is downloaded from <http://jda.jaxa.jp/result.php?lang=j&id=fdd1adb27c03b89224e6699491d9f55a>)

#### 2.2.1.2 GNSS-TEC method

I extracted the TEC information from the difference of the phases of the two microwave carriers of different frequencies  $f_1$  and  $f_2$ :

$$\begin{aligned} TEC &= \frac{1}{40.302} \cdot \frac{f_1^2 f_2^2}{f_1^2 - f_2^2} \cdot \delta\phi \\ \delta\phi &\equiv \phi_1 - \phi_2 \end{aligned} \tag{2.5}$$

These frequencies are different for each GNSS, and we have to put appropriate numbers in this equation. TEC indicates the number of electrons integrated along the line-of-sight connecting satellites and receivers. TECU (TEC unit) is used to express TEC, and 1 TECU corresponds to  $10^{16}$  electrons that exist within a column with the cross-sectional area of  $1 \text{ m}^2$ . TEC changes in time following the changes in the solar zenith angle, and shows strong diurnal variations. In Japan, TEC reaches the maximum value of 10–30 TECU around the noon, and decays to a few TECU before the sunrise. Because TEC indicates the number of electrons integrated along the line-of-sights, and it is often difficult to pinpoint where the electron density anomalies occurred. We often perform three-dimensional tomography to investigate spatial distribution of electron density anomalies using lots of GNSS-TEC data.

## Chapter 3

# Atmospheric perturbation made by volcanic eruptions

In this chapter, I discuss GNSS-TEC disturbance associated with volcanic explosive eruptions. The 2014 eruptions of the Kelud volcano, Indonesia, and the series of the 2015 eruption of the Calbuco volcano, Chile. Where examined I used GNSS data from regional networks in Indonesia and in South America. I also report on the 2015 eruption of Kuchinoerabujima volcano. Kuchinoerabujima is a volcanic island located to the southwest of Kyushu and the eruption occurred at 0:59 UT on 29 May 2015. I used the 1 Hz sampling data of GNSS stations of GEONET (GNSS Earth Observation Network System) run by GSI (Geospatial Information Authority of Japan) to investigate the TEC perturbations. I also compared the data with those from other sensors such as the broadband seismometer and the barometer data observed by NIED (National Institute of Earth Sciences and Disaster Resilience).

### 3.1 The 2014 eruption of the Kelud volcano, Indonesia

This part of the work is already published as Nakashima et al (2016). In this section, I describe the atmospheric disturbances excited by the 2014 eruption of the Kelud volcano quoting the paper.

The Kelud volcano is a very explosive volcano and has erupted eight times

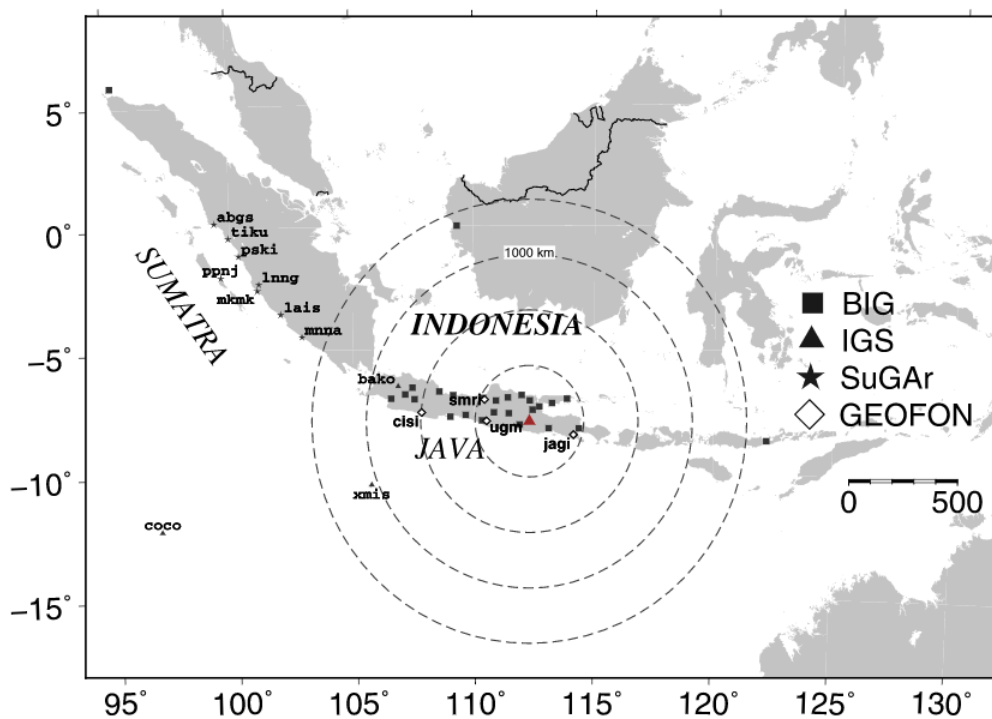


Figure 3.1: Map of the Java island and nearby islands, and the distribution of GNSS stations and broadband seismometers used in this study. The Kelud volcano is marked with the red triangle in the eastern part of the Java Island. Black triangles and stars indicate IGS (International GNSS Service) and SuGAR (Sumatra GPS Array) stations, respectively. I also use 26 stations which are run by BIG (Badan Informasi Geospasial; Geospatial Information Agency, Indonesia). White diamonds show the GEOFON stations whose waveforms are given in Figure 3.3 and Figure 3.4. (drawn from Nakashima et al, 2016, Figure 1) \*The label on the third circle is wrong. It is not 1000 km, 750 km is correct.

during the last one hundred years. The 2014 February eruption fractured the lava dome made by the 2007 eruption and created a new crater (Sulaksana et al,

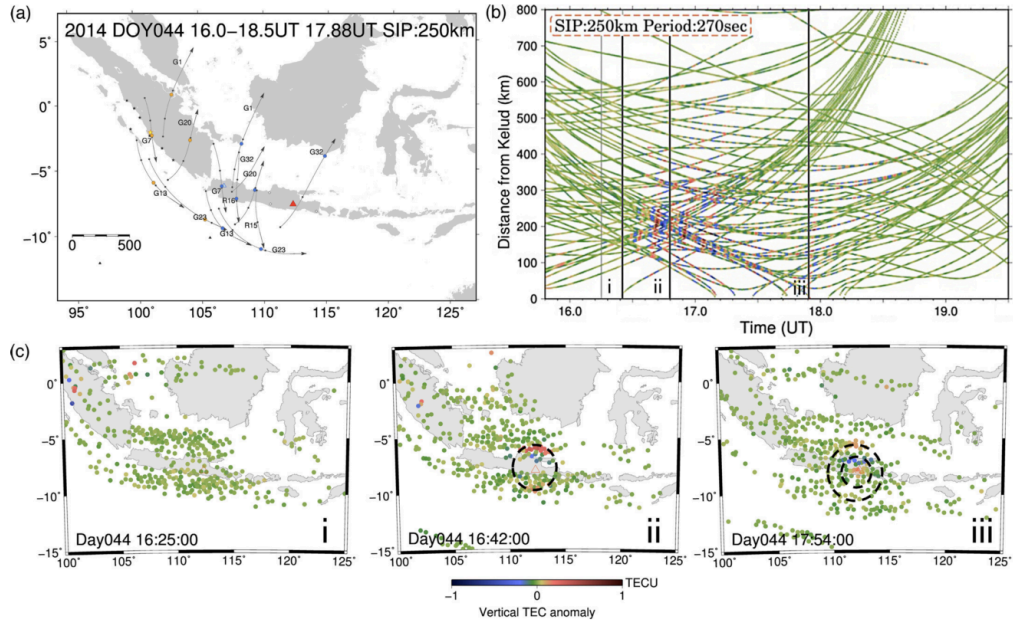


Figure 3.2: (a) Trajectories of SIP (sub-ionospheric point) of the GNSS satellites viewed from the GNSS stations LNNG and BAKO. The red triangle indicates the Kelud volcano. Large and small circles on the SIP tracks indicate those at 17:53 UT, and at 16:00 UT, 17:00 UT and 18:00 UT, respectively. (b) The horizontal and the vertical axes show time in UT and distance from the Kelud volcano, respectively. Colors indicate amplitudes of the component with the period of 270 sec extracted by wavelet transformation (Heki, 2006). (c) Spatial distributions of the 270 sec component TEC oscillations at three epochs, (i) 16:25 UT (ii) 16:42 UT (iii) 17:54 UT. (drawn from Nakashima et al, 2016, Figure 2)

2014). Caudron et al (2015) interpreted the eruption sequence from infrasound and seismic observations. The oscillation in the ionosphere and the lithosphere would have been caused by the lower atmospheric trapped modes excited by this eruption. I compare the results from the two kinds of sensors and discuss how the 13 February 2014 Kelud volcano eruption excited these atmospheric trapped modes, from the oscillations observed in the ionosphere and the solid Earth.

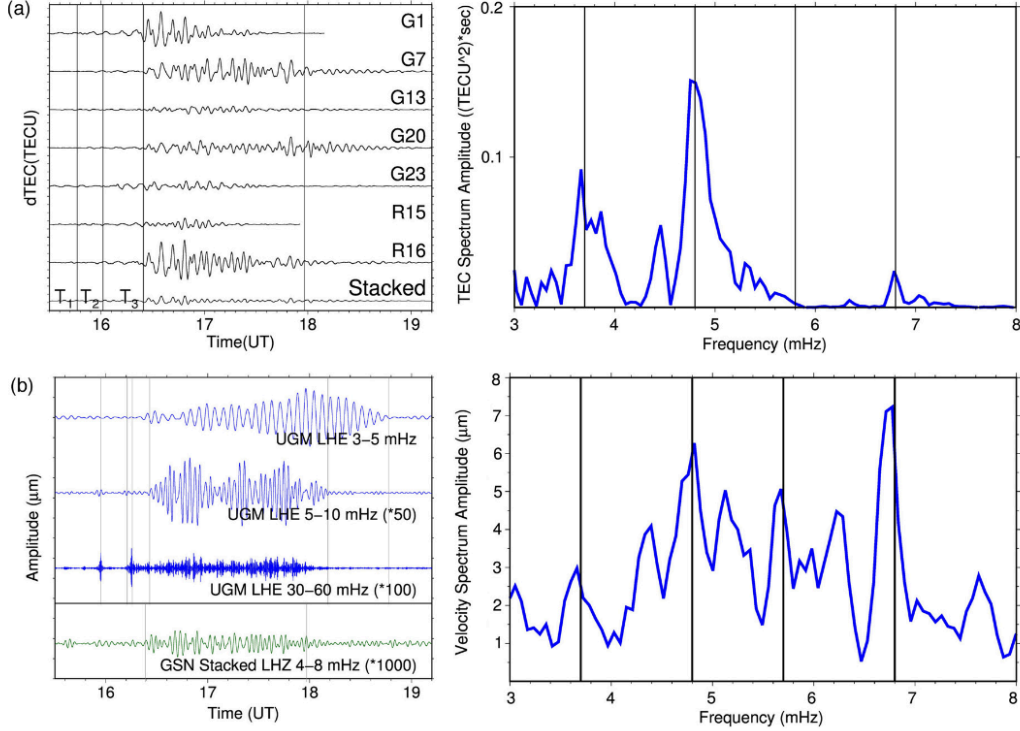


Figure 3.3: (a) The left panel shows the TEC changes observed with seven GNSS satellites, i.e. five GPS (1, 7, 13, 20, 23) and two GLONASS satellites (15, 16). Vertical lines show events indicated in Figure 3.4.

Time series of multiple sites are reduced to those at the source of the disturbance (i.e., Kelud volcano) by adjusting the time axes backward assuming the propagation velocity of 0.8 km/s. These seven time-series are stacked to produce the unified time series at the bottom, whose frequency spectrum is given in the right panel. Gray vertical lines show 3.7 mHz, 4.8 mHz, 5.7 mHz and 6.8 mHz. (b) Blue curves in the left panel show vertical velocity waveforms at the UGM station (200 km from the Kelud) with periods of 200–333 sec (top), 100–200 sec (middle) and 17–33 sec (bottom). The STS-2 seismometer detected these signals as ground motions excited by the lower atmospheric waves. The green curve indicates the source time function calculated from vertical velocity waveforms of 72 STS-1 seismometers of the Global Seismic Network. It shows the Rayleigh waves propagating in the solid earth. Vertical lines show events indicated in Figure 3.4. The frequency spectrum of the source time function is shown in the right panel. Gray vertical lines are the same as the panel (a). (drawn from Nakashima et al, 2016, Figure 3 and the seismic data was analyzed by Dr. Takeo.)



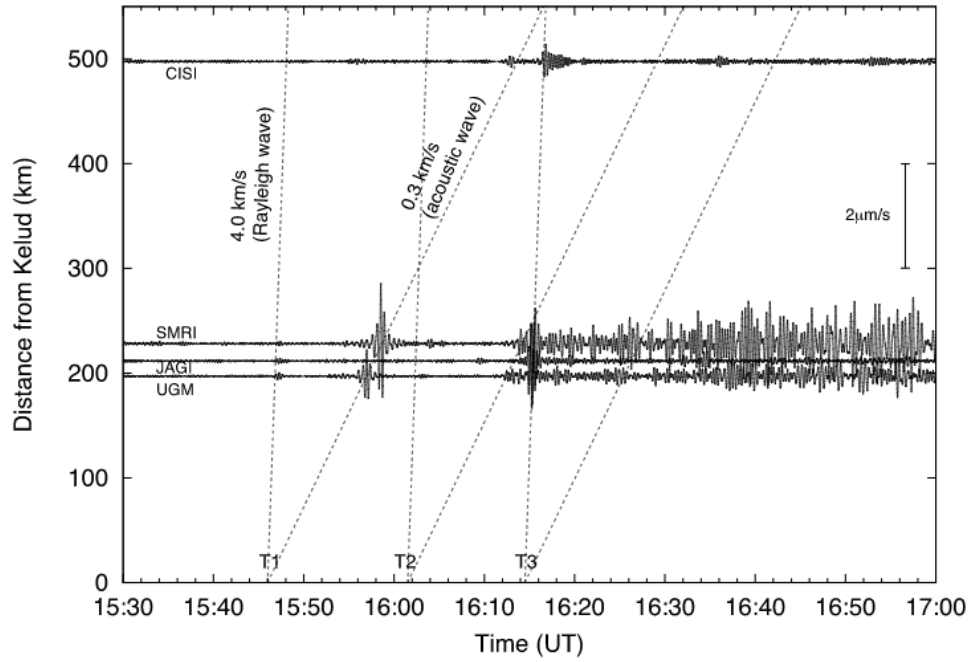


Figure 3.4: Waveforms observed at 4 GEOFON seismic stations on 13 February 2014. Vertical component time series of the raw records are plotted after a bandpass-filter to isolate components with periods of 17–33 seconds. Dashed lines show gradients corresponding to propagation speeds of 0.3 km/s and 4.0 km/s. The signal appearing around 16:00 would be the acoustic wave signal excited at  $T_1=15:46:00$  and propagated from the Kelud volcano. The continuous tremor, also of acoustic wave origin, would have started at  $T_2=16:01:30$ , and lasted for hours. I can also see the wave packet at  $T_3=16:14:30$  propagating with the Rayleigh wave speed of  $\sim 4.0$  km/s. (drawn from Nakashima et al, 2016, Figure 4 and it was made by Dr. Takeo.)

### 3.1.1 Seismic data

The 2014 eruption of the Kelud volcano was very explosive, and caused serious damages to the observation instruments deployed near the volcano. Caudron et al (2015) investigated the eruption sequence with remote ( $> 200$  km) low-frequency-seismic ( $< 0.2$  Hz) and infrasound data. They found three types of seismic signals ( $S_{LL}$ : long lasting wave,  $S_{P1}$ : only visible nearby sites and  $S_{P2}$ : short-duration energetic signal) and two types of infrasound signal ( $I_1$ : first event and  $I_{LL}$ : long lasting second event) and constructed the eruption sequence from difference of these signals.



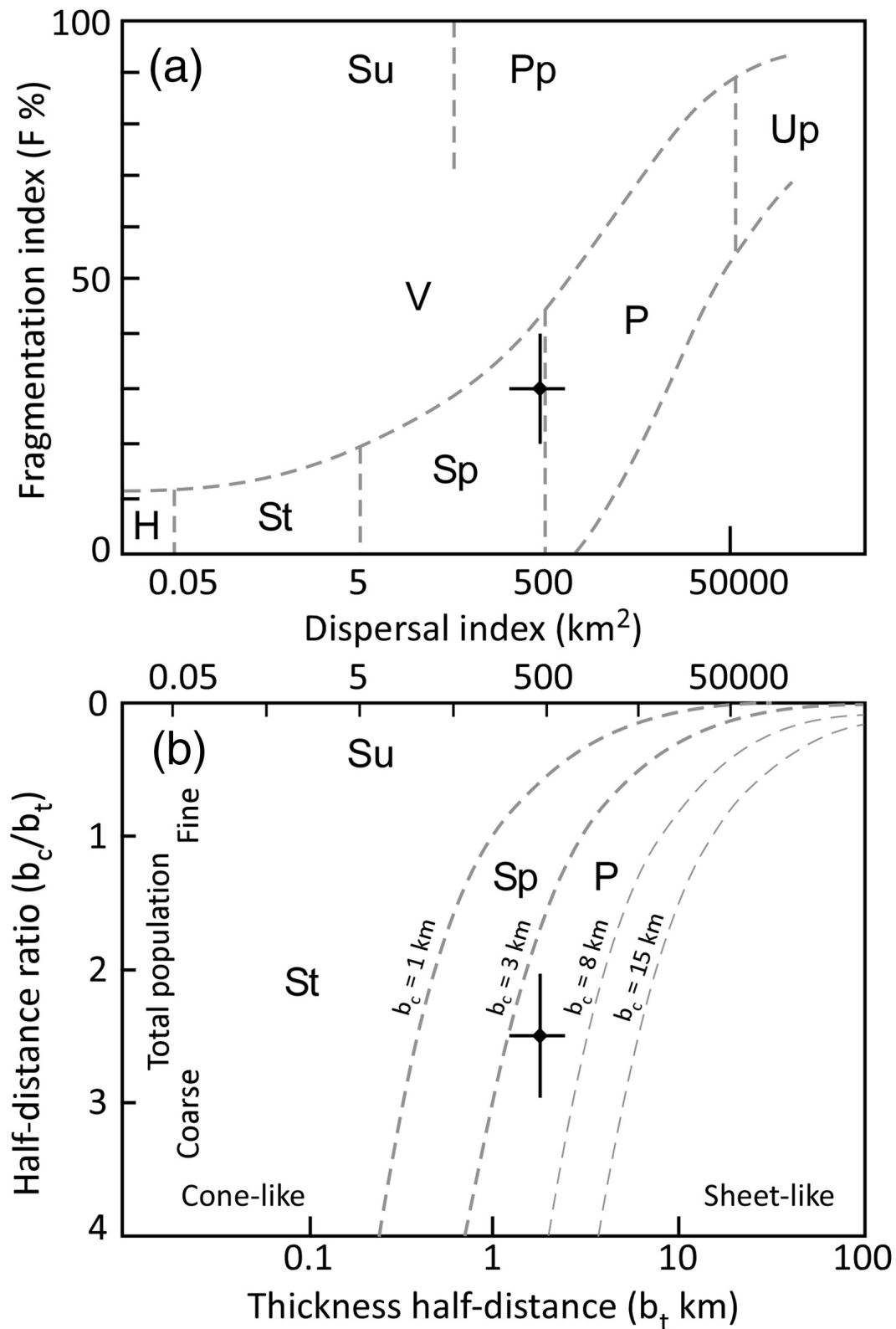


Figure 3.5: Classification of the eruption style of the 2014 Kelud eruption. (a) Walker's (1973) classification using the fragmentation and dispersal indices. (b) Pyle's (1989) classification using clast half-distance ( $b_c$ ) and thickness half-distance ( $b_t$ ). P: Plinian;  $S_p$ : Subplinian;  $P_p$ : Phreatoplinian;  $U_p$ : Ultraplinian;  $S_t$ : Strombolian; H: Hawaiian; V: Vulcanian;  $S_u$ : Surtseyan. Diamonds with error bars indicate the data from the 2014 Kelud eruption. (cited from [Maeno et al, 2017](#), Figure 13)

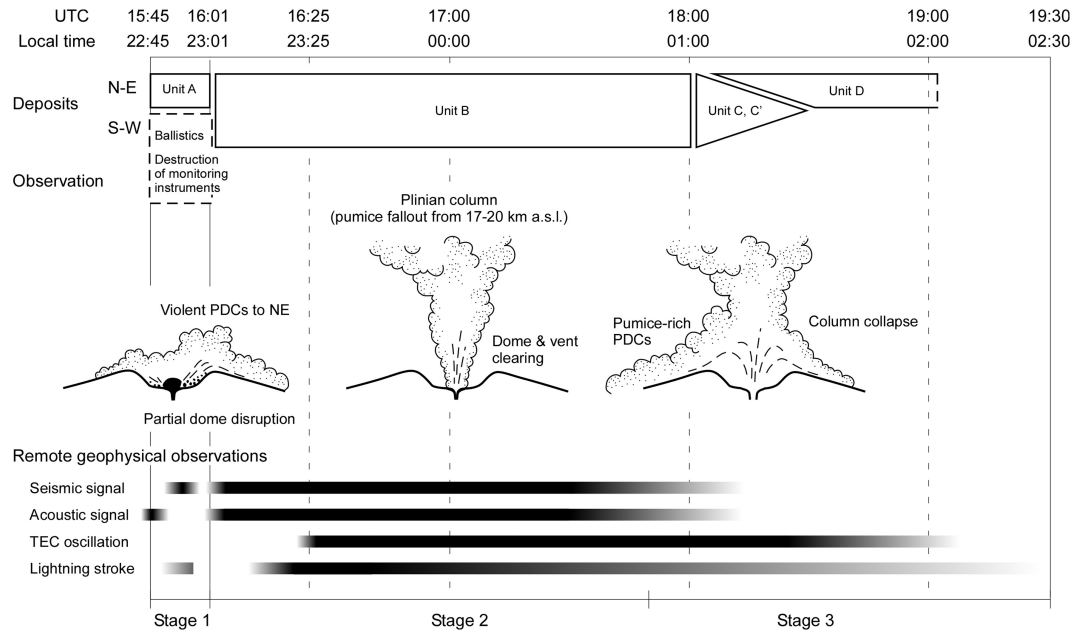


Figure 3.6: Illustration of the eruption sequence of the 2014 Kelud eruption, viewed from geological and geophysical observations. Stage 1 shows a partial, directional dome destruction generating high-energy PDCs toward the NE. Stage 2 depicts the main explosive Plinian column stage. Stage 3 illustrates the Plinian column collapse and generation of pumiceous valley-filled PDCs. The seismic and acoustic signals (bottom) are from [Caudron et al \(2015\)](#). The Total Electron Content oscillation data are from [Nakashima et al \(2016\)](#). The lightning stroke data are from [Hargie et al. \(2017\)](#). Plume height is based on [Kristiansen et al. \(2015\)](#). (cited from [Maeno et al, 2017](#), Figure 15)

Here I look into the eruption timeline from the seismometer records of periods 17–33 sec observed at three stations with the STS-2 broadband sensors of GEOFON ~200 km from the volcano, and another GEOFON station ~500 km from the volcano (Figure 3.4). The signal first appears at around 16 UT at the stations ~200 km from the volcano. The seismic records include both Rayleigh waves and ground motion due to acoustic waves (e.g. [Caudron et al, 2015](#)).

To distinguish different kinds of components in these waves, I used the difference in i) the propagation velocity, and ii) the phase shifts between horizontal and vertical components ([Nakashima et al, 2016](#), S1). The first signal could then be interpreted as the ground motion due to an acoustic wave (i.e., not a wave in the solid earth) that was excited at ~15:46 UT at the volcano, and propagated

outward in the lower atmosphere with the speed of  $\sim 0.3$  km/s. Tremor starting at 16:12 UT would also be of acoustic origin, and would have started at  $\sim 16:01$  UT at the volcano. It continued for more than one hour. Also, a relatively large amplitude wave packet propagating with the Rayleigh wave speed,  $\sim 4$  km/s, seems to have been excited at the volcano at  $\sim 16:14$  UT. From these seismic records, I interpreted that the initial explosion occurred at 15:46 UT, which was followed by the start of the Plinian eruption  $\sim 15$  minutes later. Then, an unknown event occurred at  $\sim 16:14$  UT that generated the Rayleigh wave in the solid earth.

In Figure 3.3(b), I decomposed seismic records at UGM, located  $\sim 200$  km west of the volcano, into three bands of periods, i.e., 17–33 seconds, 100–200 seconds and 200–333 seconds. I interpret that the long-lasting ground oscillation in the long-period band includes the resonant ground motion coupled with the atmospheric oscillation in the lower atmosphere. Components with periods longer than 100 seconds started at 16:25 UT, which is different from the initiation at 16:01 UT of oscillations in shorter periods. It might reflect the increase of volcanic activity due to a certain event in the solid earth at 16:14 UT such as the dome collapse or the vent expansion. Components with periods of 17–33 seconds or 100–200 seconds terminated at  $\sim 18:00$  UT, which possibly reflect the end of the Plinian eruption. On the other hand, the oscillations with periods of 200–333 sec continued until  $\sim 19:00$  UT. This period band includes those of the ionospheric oscillations, which would have been excited by the atmospheric free oscillation that continued  $\sim 1$  hour after the termination of the Plinian eruption.

Seismic signals with periods of 100–1000 seconds were observed at the 78 broadband seismometers (STS-1) of the Global Seismic Network (GSN) around the world (Nakashima et al, 2016, S2). The signal is shown to come from the Kelud volcano (Nakashima et al, 2016, S3) with the speed of the fundamental-mode Rayleigh wave (Nakashima et al, 2016, S4) for the Preliminary Reference Earth Model (PREM) by Dziewonski and Anderson (1981). Assuming the Rayleigh wave

phase velocity, I estimated the source time function at the Kelud volcano by stacking velocity waveforms after correcting for sensor responses (Figure 3.3(b)). The spectrum shows broad source with several clear peaks including those at 3.7 mHz, 4.8 mHz, 5.7 mHz and 6.8 mHz (Figure 3.3(b)). Assuming the atmospheric top free surface boundary at  $\sim 90$  km above ground, the eigenfrequencies of the standing acoustic modes in the atmospheric layer would be 3.7, 4.7, 5.8 and 7.1 mHz for fundamental, first, second, third and fourth overtones in the vertical direction, respectively (Watada and Kanamori, 2010). The altitude of the mesopause ( $\sim 100$  km) calculated from the International Reference Ionosphere (IRI) (Bilitza et al, 2011) is close to this assumption. The continuous spectrum would reflect the turbulent atmospheric waves excited directly by the Plinian eruption. The discrete amplitude peaks are explained by the resonant oscillation of the lower atmosphere and its leakage into the solid Earth as demonstrated by Watada and Kanamori (2010).

### 3.1.2 GNSS-TEC data

I extracted the TEC information before and after the 2014 February eruption of the Kelud volcano from the raw data of 37 GNSS stations in and around Indonesia. The observation data are from three networks, (1) the GNSS network in Java run by the Badan Informasi Geospasial (BIG), (2) Sumatra GPS Array (SuGAR) operated in Sumatra by Indonesian Institute of Science and California Institute of Technology, and (3) International GNSS Service (IGS) stations (Figure 3.1). The SuGAR stations observed only Global Positioning System (GPS) every 15 seconds. Other stations received signals from both GPS and GLONASS every 30 seconds, except for COCO where only GPS data are recorded. I extracted the components with periods around 270 seconds from slant TEC (STEC) time series using the Mexican-hat wavelet. To make it possible to compare amplitudes between different station-satellite pairs, I converted the amplitudes into those in

vertical TEC (VTEC) by multiplying with the cosine of the incidence angle of the line-of-sight with a thin layer at 250 km height. This height is also used to calculate the coordinates of sub-ionospheric points (SIPs).

After extracting the 270 sec components, I estimated their propagation velocity by plotting the time and distance from the volcano of the TEC disturbances following [Rolland et al \(2011\)](#). The estimated propagation velocity was  $\sim 0.8$  km/s, close to the acoustic wave speed in the F region of the ionosphere, and the oscillation in this period continued from 16:25 UT to 19:00 UT (Figure 3.2). The SIPs of the disturbance in this frequency show clear concentric wavefronts propagating outward from the volcano (Figure 3.2(c), [Nakashima et al, 2016](#), Animation S1). I obtained the frequency spectrum of the TEC oscillations. First, I extracted components with frequencies 2.0–8.0 mHz with a band-pass filter for the stations within 1,000 km from the volcano. At first, for individual satellites, I adjusted the time axes of the time series of different stations assuming 0.8 km/s as the propagation velocity. The TEC data obtained with the same satellite results have similar geometry. I confirmed that the data with different satellite possess similar signal structures, and then I further stacked them (Figure 3.3(a)). Finally, the master time series obtained by the double stacking were converted into the frequency domain. The spectrum showed two clear peaks at 3.7 mHz and 4.8 mHz (Figure 3.3(a)).

### 3.1.3 Discussion and summary

First, I discuss the duration of the various observed phases of the eruption. For the initial explosion at  $\sim 15:46$  UT, I could not identify the N-shaped pulsation in ionospheric TEC which may appear  $\sim 10$  min later. As shown in the short period (17–33 seconds) seismic signals (Figure 3.3(b)) possibly caused by the ground vibration in the continuous eruption, the Plinian eruption may have started at  $\sim 16:01$  UT and lasted for  $\sim 2$  hours. After the termination of the Plinian eruption

at  $\sim 18$  UT, long period signals (200–333 seconds) were observed until  $\sim 19$  UT both in the ionosphere (Figure 3.3(a)) and on the ground (Figure 3.3(b), the top signal). It would indicate the atmospheric free oscillation that continued even after the termination of the Plinian eruption and decayed slowly in one hour.

The seismic signals from 16:25 UT to 18:00 UT showed peaks at 3.7 mHz, 4.8 mHz, 5.7 mHz and 6.8 mHz, suggesting that the lithosphere–atmosphere coupling also occurred along with the ionosphere–atmosphere coupling. The oscillations of TEC started at  $\sim 16:25$  UT,  $\sim 20$  min after the start of the Plinian eruption at  $\sim 16:01$  UT. This time lag would reflect the time for the growth of the lower atmospheric oscillation to reach the ionospheric F layer ( $\sim 300$  km). The Plinian eruption ended at  $\sim 18$  UT. However, the ionospheric and lower atmospheric oscillations continued until  $\sim 19:00$  UT due to relatively large quality factor ( $Q$ ). The atmospheric  $Q$  at 3.7 and 4.6 mHz are about 150 and 20, respectively (Rolland et al, 2011), and these  $Q$ s are high enough for the atmospheric free oscillation to continue for one hour without further excitation.

Here I studied ionospheric signatures made by the eruption of the Kelud volcano on 13 February 2014, with regional networks of continuous GNSS receivers. This study gives the detailed report of spatial distribution and time evolution of ionospheric disturbances by a Plinian eruption. First, the Plinian eruption would have caused atmospheric turbulence in its plume. The turbulence itself had broad frequency spectrum, and standing waves or acoustic fundamental and overtone modes trapped in the lower atmosphere were excited. Then, some part of the energy of these standing waves would have leaked into the ionosphere and lithosphere, resulting in spectral peaks in TEC and seismograms. This Plinian eruption that drove the multisphere oscillations ended at  $\sim 18$  UT, and only low-frequency oscillation continued for one more hour in the ionosphere and lower atmosphere.

This study can be summarized as follows.

- (1) With the GNSS-TEC technique, I observed ionospheric oscillations forced by lower atmospheric natural vibration after the start of the 2014 February Plinian

eruption of the Kelud volcano, Indonesia. The Plinian eruption lasted from  $\sim 16:01$  UT to  $\sim 18:00$  UT while the TEC oscillation lasted from  $\sim 16:25$  to  $\sim 19:00$  UT. The TEC oscillations showed frequency peaks at 3.7 mHz and 4.8 mHz.

(2) Spectra of the seismic records showed peaks of a series of atmospheric acoustic modes, 3.7 mHz and 4.8 mHz, and two higher modes. These frequency peaks suggest that the harmonic ground motions are excited by the coupling between the solid Earth and the lower atmosphere.

After the publication of our letter, [Maeno et al \(2017\)](#) reported the sequence of the eruption by geological approach. They showed that the eruption is Plinian eruption in Walker's and Pyle's classifications (Figure 3.5; also see Figure 1.7). They compiled their geological investigation with several geophysical results including our results (Figure 3.6). The TEC oscillation may be sustained by the collapse or pyroclastic density currents (PDCs), not only by a large Q value.

## 3.2 The 2015 Calbuco volcano eruption, Chile

The eruptions occurred twice at the Calbuco volcano in Chile during the period from 22 to 23 Apr. 2015 ([Van Eaton et al, 2016](#)). Figure 3.7 reports the ground oscillation from seismometers and the growth of the umbrella cloud radius from satellite observations associated with the two eruptions. The first eruption continued for about 1.5 hour from 22 Apr. 21:04 UT to 22:35 UT. The second one was longer, and lasted from 23 Dec. 04:00 UT to 10:00 UT, and several pyroclastic flows were observed at about 07:00 UT on 23 Dec. [Shults et al \(2016\)](#) analyzed the GNSS-TEC observations, and reported the overview of the event and estimated secondary wave source that disturbed the ionosphere. [Aoyama et al \(2016\)](#) reported the geomagnetic fluctuations in frequencies 3.84 and 4.65 mHz detected by the SWARM satellites, possibly caused secondarily by ionospheric disturbances. I used 15 sec and 1 sec sampling GNSS data collected by RAMSAC, Argentina

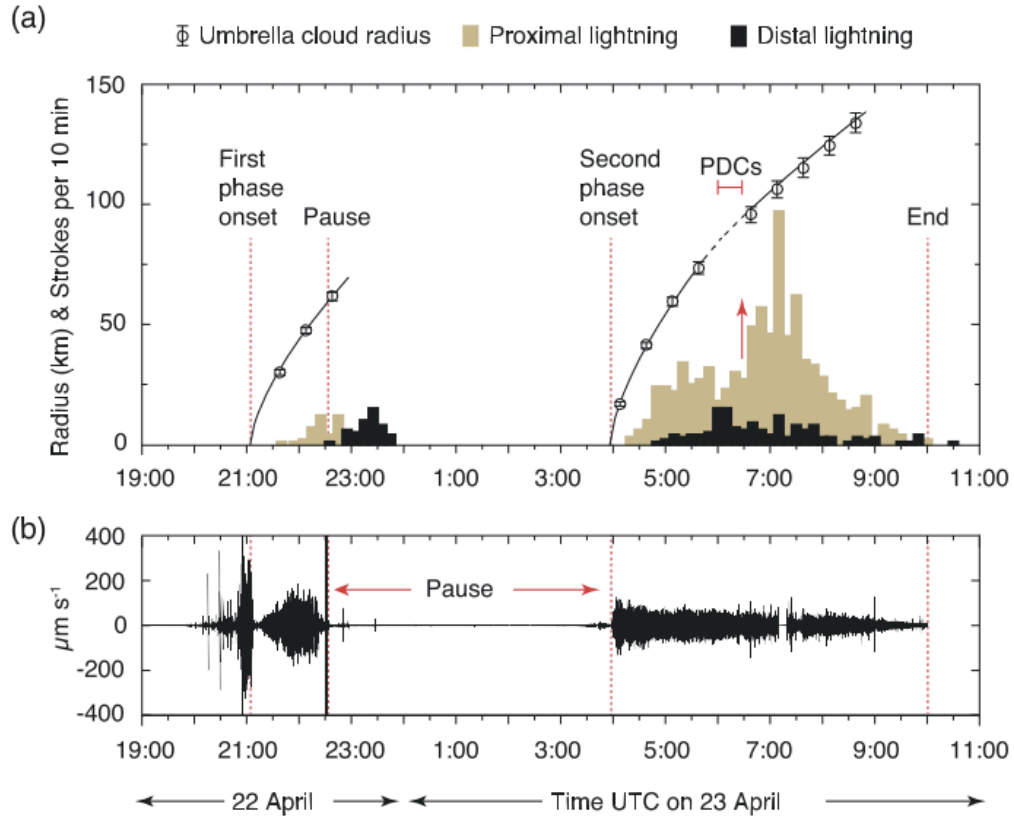


Figure 3.7: Time series of the cloud images from GOES-13, lightning, and seismic observations for the 2015 Calbuco volcano eruption. (a) Symbols show mean and range of the radius of the “umbrella cloud” made by the eruption. defined by the GOES-13 brightness temperatures of  $-3$  and  $-13$   $^{\circ}\text{C}$ . Black curves show best fit theoretical expression for expansion rates of the umbrella cloud. WWLLN-detected lightning stroke rates are given at 10 min intervals for proximal ( $<20$  km) and distal lightning ( $>20$  km from the volcano). Red lines indicate eruption processes described in the text of the original paper. Note the shift to slower umbrella expansion rates after  $\sim 5:30$  on 23 April (dashed line) and sharp increase in proximal lightning (red arrow), when the formation of significant pyroclastic density currents (PDCs) is inferred. (b) Seismic amplitude filtered between 0.5 and 5 Hz, from station  $\sim 3$  km from the summit. Gap in seismic data occurs  $\sim 7:15$  due to temporary lapse in communications. (cited from [Van Eaton et al, 2016](#), Figure 2)



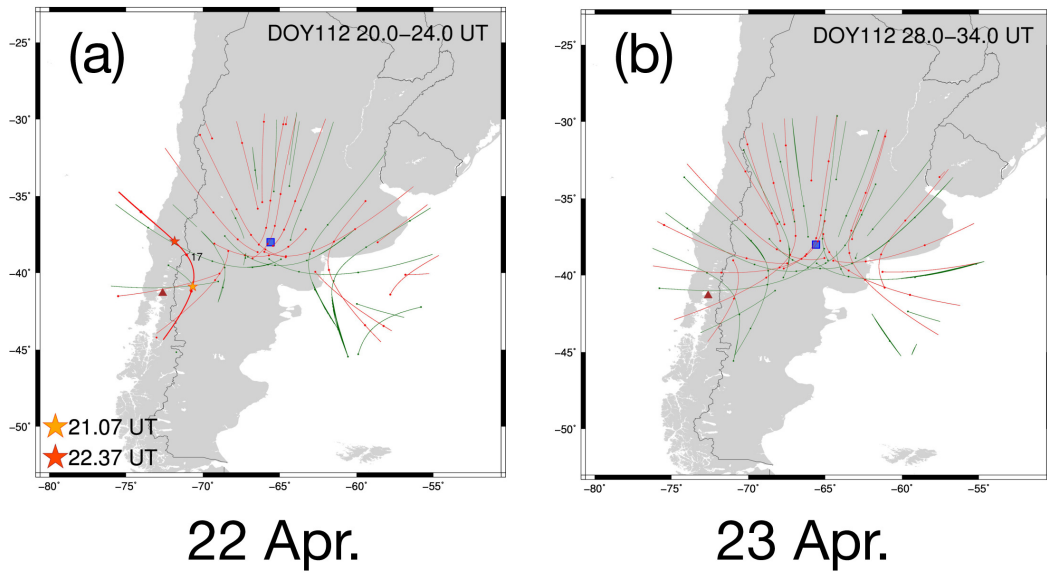


Figure 3.8: SIP tracks for each satellite observed at station LHCL. Red curves show GPS-SIP tracks and the green curve indicates GLONASS-SIP tracks. (a) 20–24 UT, 22 Apr. 2015. Yellow and Red stars indicate eruption start and end times, respectively. (b) 4–10 UT, 23 April 2015.

GNSS array (Figure 3.8). Here, I mainly discuss the frequency components and the duration of the ionospheric disturbances.

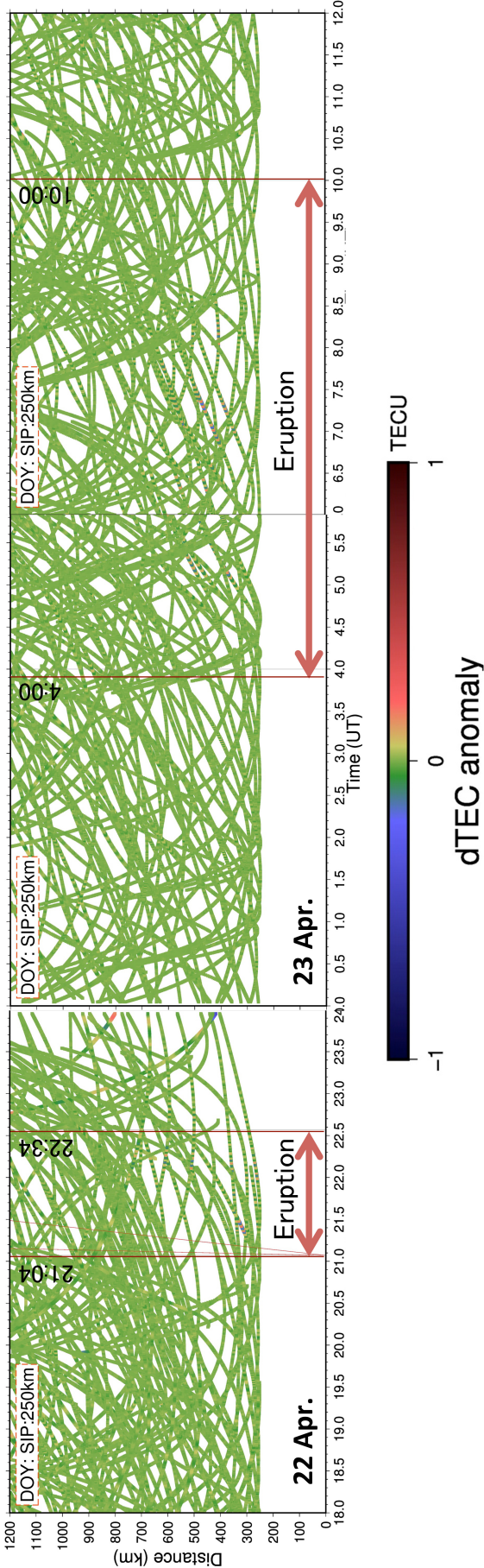


Figure 3.9: Ionospheric disturbances by the 2015 eruption of the Calbuco volcano, Chile. The vertical axis indicates distance between the volcano and SIP, and the horizontal axis shows time in UT. Vertical red lines are start and end times of the eruptions. The TEC oscillations started over 25 minutes later than the eruption start times.

### 3.2.1 Duration of ionospheric perturbation observed by GNSS-TEC

Similar observation results have been derived by GNSS-TEC for the 2015 eruption of the Calbuco volcano, Chile by [Nakashima et al \(2016\)](#) and [Shults et al \(2016\)](#). They found acoustic trap modes generated by this eruption (volcanic explosivity index (VEI) was 3–4). [Aoyama et al \(2016\)](#) found a magnetic ripple induced such TEC fluctuation by the 2015 Calbuco volcano eruption. The overall signatures are similar to the 2003 Soufrière Hills volcano eruption, but the continuous harmonic oscillation of TEC lasted much longer reflecting the stronger/longer eruption sequence.

[Shults et al \(2016\)](#) did not discuss the duration of the oscillation in TEC. I found that the oscillation continued until the eruption stopped (Figure 3.9). Durations of the ionospheric disturbances mostly overlap with the periods of high volcanic activity (Figure 3.7), but smaller amplitude TEC oscillations seem to have continued for an hour or so even after the end of the eruption.

### 3.2.2 GNSS-TEC frequency components

I found frequency components in the TEC oscillations not reported in [Shults et al \(2016\)](#). In the upper panels of Figure 3.10, I show that peaks are found at 3.94, 4.40, 4.89, and 5.78 mHz (first eruption) and 3.92, 4.28, and 5.08 mHz (second eruption). These frequency peaks have some common frequencies to the case in the 2014 Kelud eruption (Figure 3.3 right panels). The difference might come from the different atmospheric structures between Indonesia and Chile, but needs further studies to interpret. I would also like to note that a short-lived weak peak of about 10 mHz is seen at 21.4–21.5 UT. This might correspond to the initial N-shaped perturbation in TEC associated with the propagation of the shock-acoustic wave excited by the explosion.

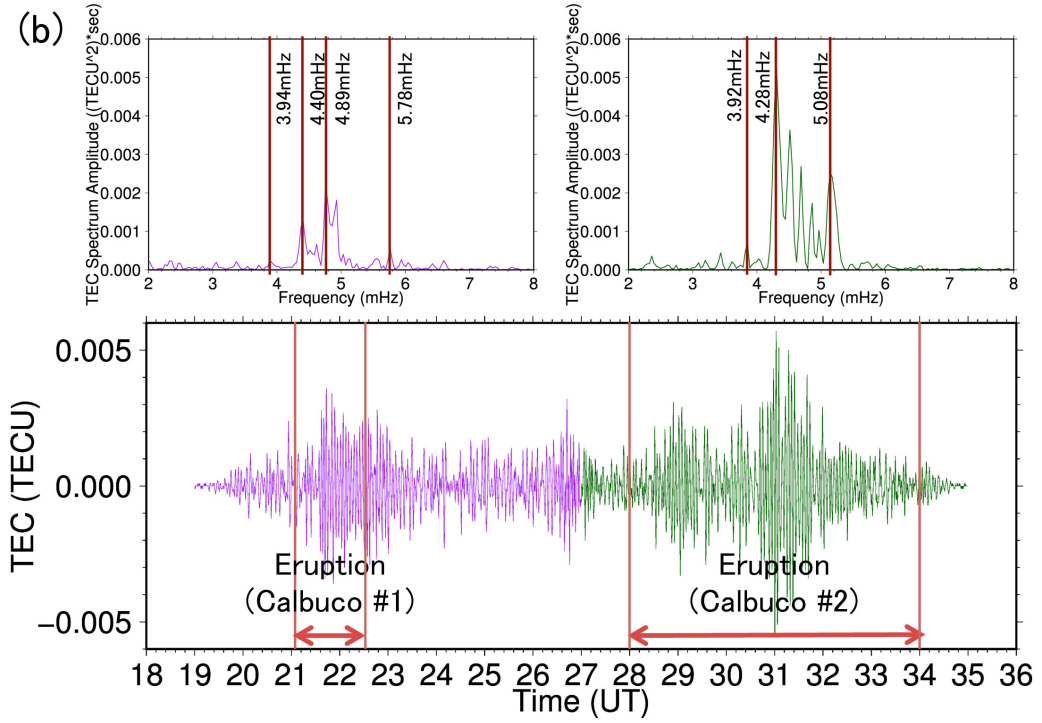


Figure 3.10: Ionospheric disturbances by the 2015 eruption of the Calbuco volcano. Vertical red lines are eruption start and end times. The TEC oscillations started 25 minutes or more later than the eruption start times. In the upper part, I show frequency spectra of TEC changes during the two eruption periods. I added vertical red lines with frequency values for prominent frequency peaks.

### 3.2.3 Summary of the section

1. The two long-lasting eruptions in the 2015 eruption sequence of the Calbuco volcano, Chile, excited acoustic trap modes in the ionosphere with three or four different frequencies.
2. The initial part may include a higher frequency N-shaped impulsive signal.
3. The atmospheric mode took about 25 minutes to start after the initiation of the continuous eruptions. This would be the time required for the descending and the ascending waves to interfere and to make a standing wave.
4. The atmospheric modes lasted for one hour or so even after the terminations of the two continuous eruptions.

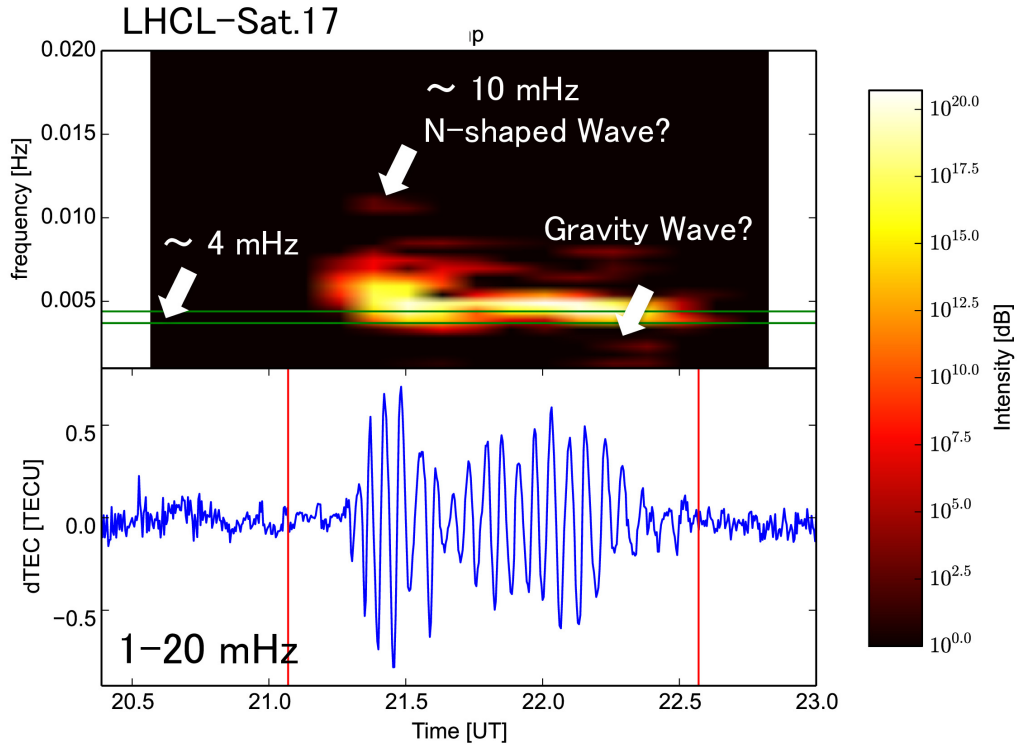


Figure 3.11: Top: Spectrogram and waveform observed at the station LHCL and GPS satellite 17, which has the largest amplitude in the observed data. The spectrogram shows the peaks corresponding to the normal mode of acoustic trap mode of about 4 mHz and additional higher modes around 5 mHz. Bottom: The waveform is derived by stacking all the observed data from 19:00 UT, 22 Apr. to 11:00 UT, 23 Apr, 2015. It is band-pass filtered to 2–10 mHz. The vertical axis is the time in hour from 0:00 UT, 22 Apr. Upper two figures show the spectrum of the stacked waveform shown at the bottom. Left one represents 18:00–27:00 (3:00 UT, 23 Apr.) and right one represents 27:00–35:00 (3:00–11:00 UT 23 Apr).

5. TEC perturbation grew larger after 5:10 UT, and it may indicate the increasing intensity of the eruption

### 3.3 Kuchinoerabujima volcano eruption on 29 May 2015

Kuchinoerabujima is a volcanic island located about 100 km off the southern tip of Kyushu, the westernmost island of the four main islands in Japan. The explosive

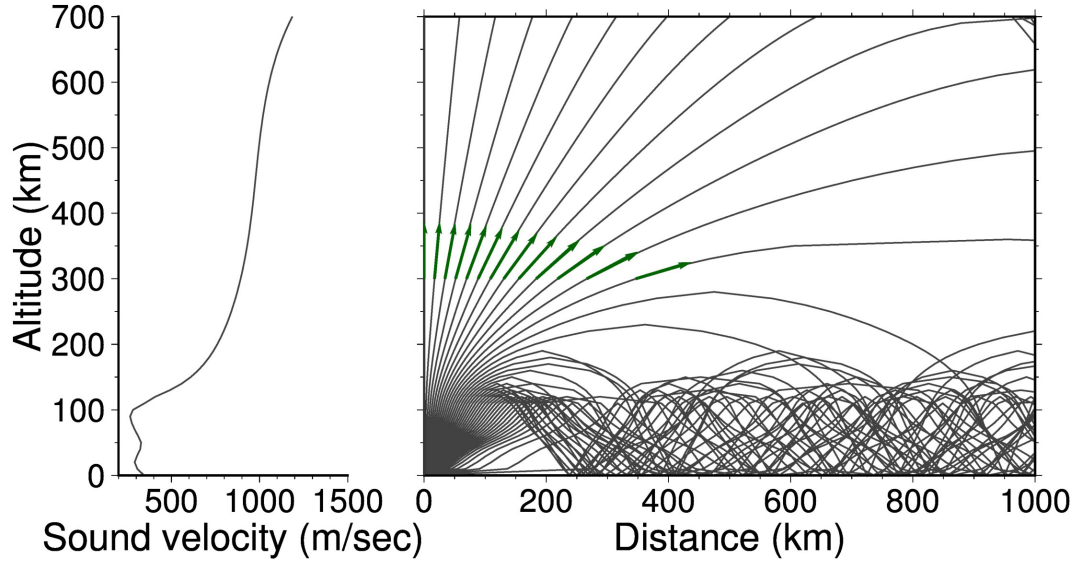


Figure 3.12: Left: Sound velocity calculated from the NRLMSISE-00 atmospheric model. Right: Ray path calculated by the ray tracing technique using the sound velocity profile indicated to the left.

eruption of the volcano occurred at 0:59 UT (9:59 LT) May 29, 2015, with the eruption magnitude VEI 3 ([Global Volcanism Program, 2013](#)). [Matsuzawa et al \(2016\)](#) calculated the seismic source time function of this eruption using seismic records with periods 10–20 sec from the F-net, a Japanese dense broadband seismometer (STS-1, 2, 2.5) array operated by NIED (National Institute of Earth Sciences and Disaster Resilience). [Yamada et al \(2017\)](#) estimated volume flux of the eruption using infrasound signals with periods 10–50 seconds.

In this study, I discuss the GNSS-TEC observation data showing the propagation of acoustic waves with frequencies  $< 0.01$  Hz in the ionosphere. I also compare them with the records taken near surface using multiple instruments such as barometers and broadband seismometers.

### 3.3.1 Details of the observation

I used arrays of broadband seismometers and barometers to study the air waves associated with the 2015 Kuchinoerabujima eruption. At first, I briefly introduce



features of the instruments used in this section.

I used several kinds of instruments for air pressure change observations. Such

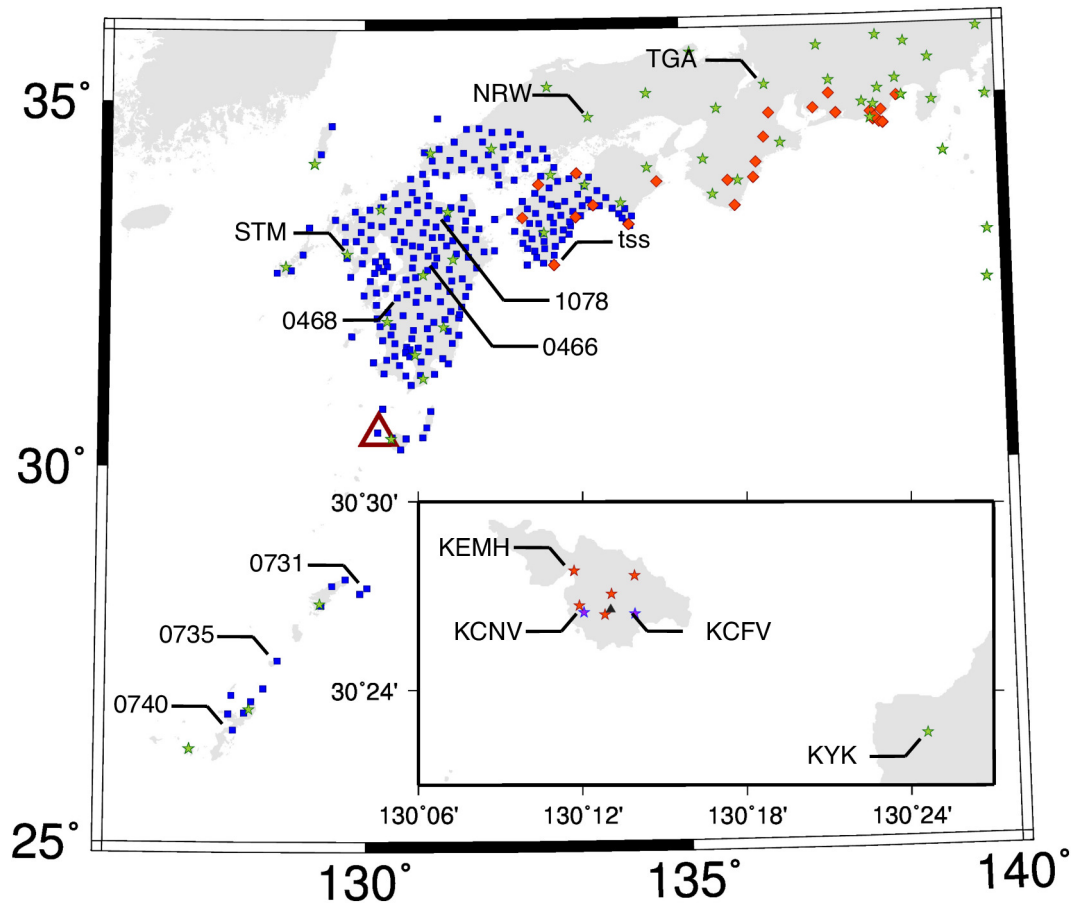


Figure 3.13: Map around Kuchinoerabujima volcano and stations. The red triangle indicates the Kuchinoerabujima volcano. Blue squares are GEONET stations. Red diamonds show the AIST barometers. Green stars denote the F-net broadband seismometers. Red stars are JMA volcano observation stations. Blue stars show V-net stations installed by NIED.

instruments are suitable to detect sound waves with the frequency higher than 0.02 Hz. Such waves do not reach the upper atmosphere due to large attenuation. I use data from the three arrays, i.e., V-net, JMA (Japan Meteorological Agency) stations, and the barometer array deployed by AIST (National Institute of Advanced Industrial Science and Technology). V-net is an array of all-in-one geophysical observatories installed around active volcanoes in Japan. V-net includes the Vaisala PTB100 (VAISALA, 1997) barometer. Their measurement range is about 800–1100 hPa and the accuracy is about  $\pm 0.3$ – $0.5$  hPa.

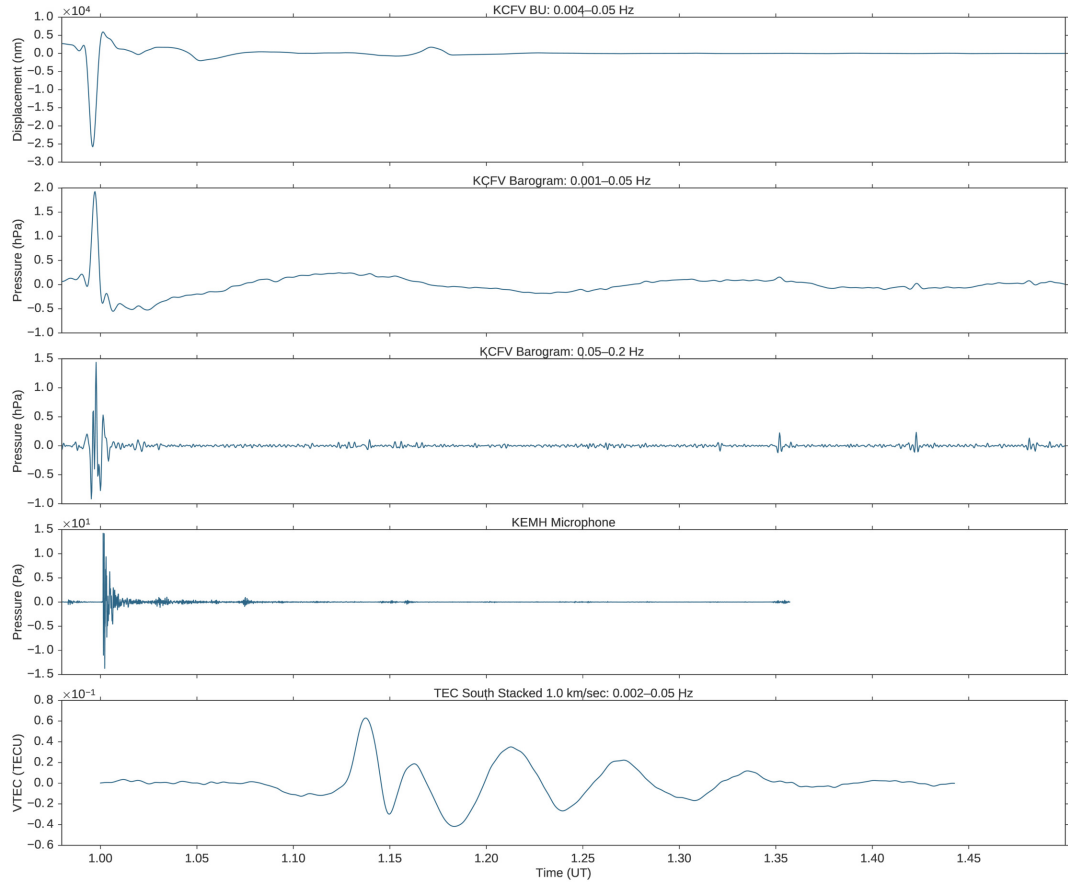


Figure 3.14: Atmospheric waves, and induced vertical crustal movements, observed with various instruments. The panels indicate, from top to bottom, the vertical surface displacement at KCFV (0.004–0.05 Hz), the air pressure change at KCFV (0.001–0.05 Hz), the air pressure change at KCFV (0.05–0.2 Hz), infrasound at KEMH (0.02 Hz) and the stacked TEC perturbation (0.002–0.05 Hz).

The AIST barometer array uses the Paroscientific Model 1000 (except type) and Yokogawa F4711 (type). Their range is 800–1100 hPa and the accuracy is  $\pm 0.08$  hPa.

I analyzed the two broadband seismometer array data operated by NIED (National Research Inst. Earth Sci. Disaster Resilience), F-net and V-net. F-net is an array composed of 74 broadband seismometers deployed in Japan. F-net consists of the Streckeisen STS series broadband seismometers. In the two V-net stations on Kuchinoerabujima, they installed the Trillium 240 as broadband seismometers (Nanometrics Inc., 2005).



### 3.3.2 Near surface atmospheric perturbation

#### 3.3.2.1 Near-field observation on the ground

First, I discuss the eruption signatures recorded by two broadband seismometers (Trillium 240), and two barometers (PTB100) installed as a part of the V-net on the island. Both of the instruments detected the air waves excited by this volcanic eruption (Figure 3.14).

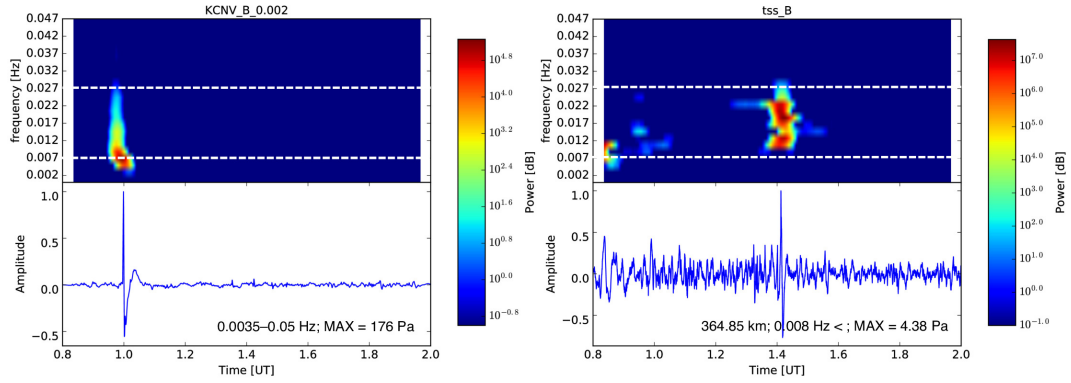
Air wave signals in seismograms and barograms are extracted using a low-pass filter because they had different responses to the dominant frequency components of the airwaves. I applied the band-pass filter to them to isolate frequency components 0.01–0.04 Hz and found similar signals in both of the barograms and the seismograms.

I assumed that the solid earth deformation was caused by changes in the atmospheric pressure and estimated the amplitudes of pressure changes from displacements inferred from seismic records. Please see the section 2.1.2 for the detail of the relationship between the barometer and seismometer records. From the vertical displacement,  $-200\mu\text{m}$ , I estimated the air pressure change as 140 Pa at the seismometer station KCFV. Considering that the barometer recorded a pulse of 120 Pa at the same station, the air pressure change inferred from the seismometer is consistent with the direct measurement by barometers. Next, I try to extract the initial atmospheric perturbation signals propagating farther away from a series of seismograms in Japan using the same method.

#### 3.3.2.2 Far-field observation on the ground

I also checked the records from the seismometer array, F-net, and the barometer array (Digiquartz Pressure Instrumentation Series 1000 and F4711) installed by

## Barometer



## Seismometer (0.01–0.04 Hz)

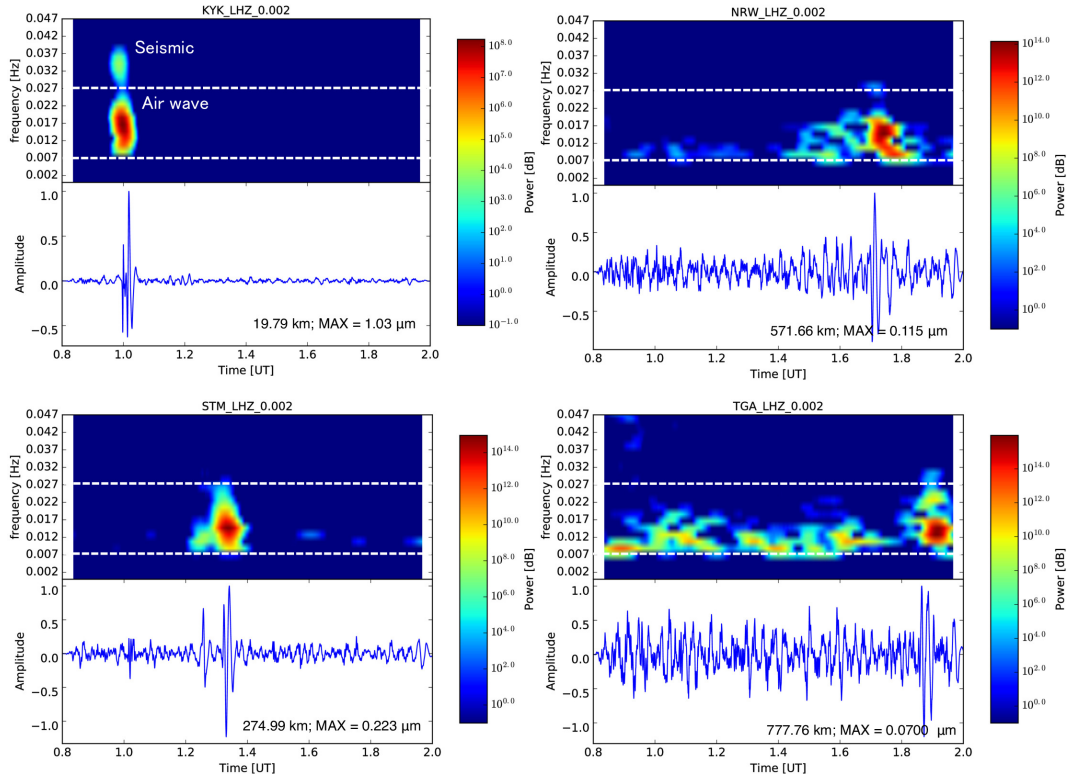


Figure 3.15: Spectrograms of barometer and seismometer records derived by moving the time window for the Fourier transformation. They are computed over 512 second intervals and the consecutive windows overlap with each other by 500 sec. Top: Barometer results Bottom: Seismometer results

AIST (here I refer to it as the AIST barometer array) to detect the propagation of the air wave from the Kuchinoerabujima eruption (Figure 3.14). I found similar signals in the band-pass filtered (0.01 to 0.02 Hz) records of the F-net and the AIST barometer array (Figure 3.16). The travel time curves of seismogram are

similar to the barogram. The surface vertical displacements were driven by air pressure changes associated with the passage of the air waves, which were also detected by barometers.

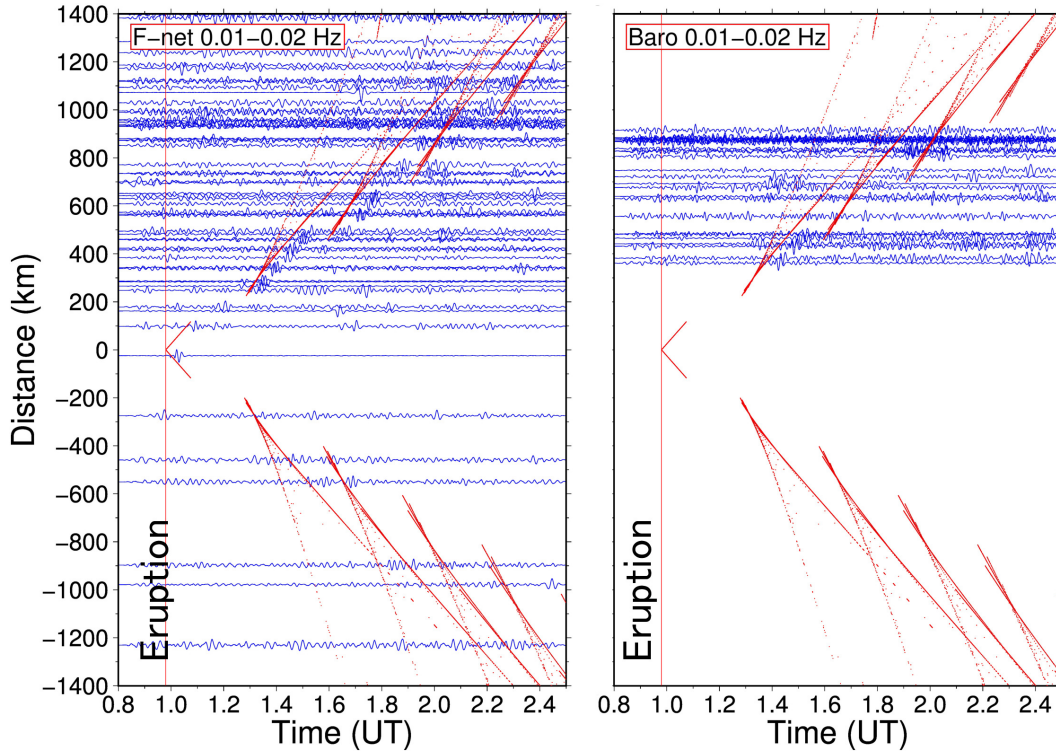


Figure 3.16: Travel time diagrams for ground observations, Dotted curves in red indicate travel times synthesized by ray tracing. Left: F-net Right: AIST barometers.

### 3.3.3 Ionospheric perturbation observed by GNSS-TEC

I detected TEC perturbations caused by atmospheric waves propagating through the ionosphere by analyzing the 1 Hz sampling GNSS carrier phase data from GNSS Earth Observation Network (GEONET) (Figure 3.17), the Japanese dense array of GNSS receivers operated by Geospatial Information Authority of Japan (GSI).

The disturbances caused by the explosion were detected by three GNSS satellites,

i.e., GPS Sat.14, 25 and GLONASS Sat.2. The signals propagating southward were  $\sim$  ten times as strong as the signals propagating northward due to the interaction with the local geomagnetic fields. The horizontal wavelength of the TEC perturbations was  $\sim$ 200 km (Figure 3.18).

Next, I discuss the spectrograms of the signals derived by the consecutive (moving

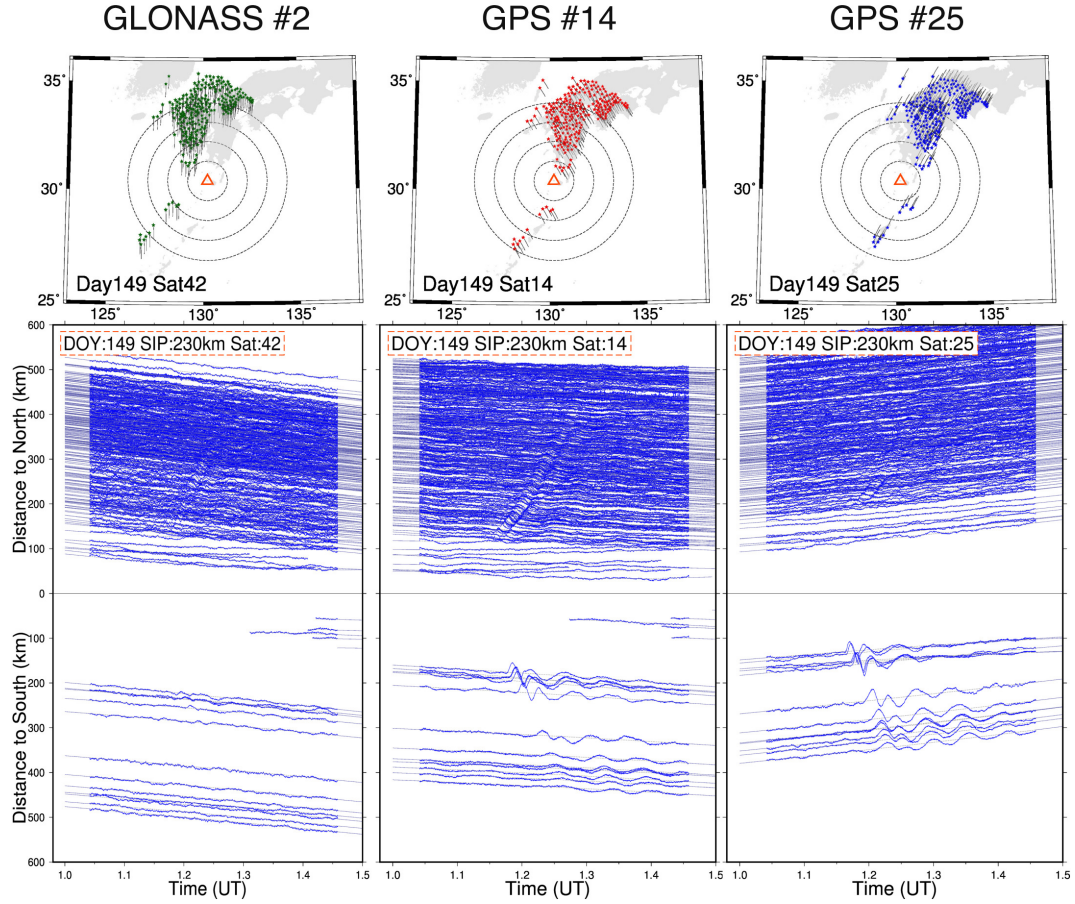


Figure 3.17: The figure shows the observation results by GLONASS Sat.2, GPS Sat.14 and GPS Sat.25 from left to right. Top: Tracks of SIPs 1.0–1.5 UT May 29, 2015. Stars indicates the SIPs at 1.0 UT. Bottom: GNSS-TEC travel time diagrams for individual pairs of satellites and ground stations.

time window) Fourier transformation. The TEC signals were found to include two strong components (Figure 3.19). One is an impulsive signal of about 0.012 Hz (period  $\sim$ 83 sec), and the other is the continuous oscillation with frequencies of a few mHz lasting for 15 minutes. The former component is the N-shaped wave or shock acoustic waves (SAWs), often observed about ten minutes after Vulcanian

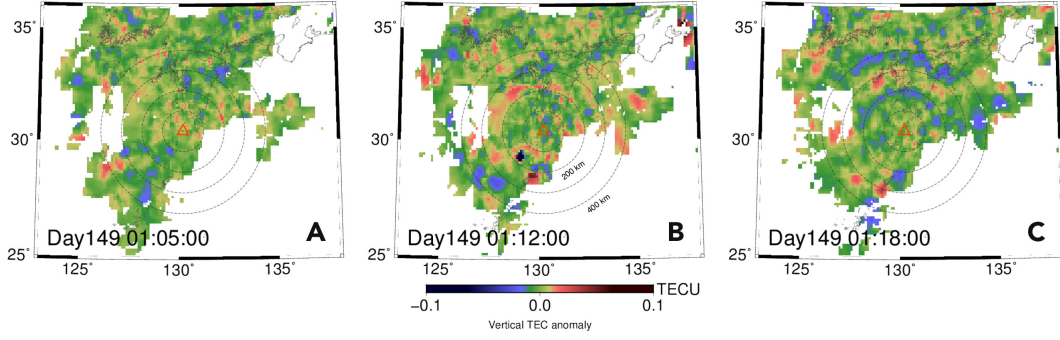


Figure 3.18: Horizontal TEC perturbation distribution at three different time epochs, 6 minutes (A), 13 minutes (B), and 19 minutes (C) from the explosive eruption. Clear concentric wavefronts are visible at the later two epochs. IPP altitude is assumed at 230 km.

explosions. This wave in ionosphere lacks higher frequency components as seen in ground sensors. Such a difference in frequency spectrum would be due to the atmospheric filtering effect as shown in Chapter 1.

On the other hand, although the broadband seismometers and the barometers detected a pulse including shorter periods, they lack low frequency oscillation lasting for several minutes or more in TEC records (Figure 3.14). There would be two possibilities. At first, the broadband seismometers may not have detected the signal of this frequency range because of the instrumental limitation. Secondly, atmospheric waves with  $\sim 5$  mHz may not have been excited or have poor energy near the surface.

### 3.3.4 Interpretation of wave propagation

#### 3.3.4.1 Multi-sensor travel time

I detected the direct and the reflected waves propagating between the ground surface and the atmospheric boundary located  $\sim 100$  km above (mesopause) using the AIST barometers and the F-net broadband seismometers (Figure 3.16). The frequency components of 10–20 mHz have been isolated using a band-pass filter.



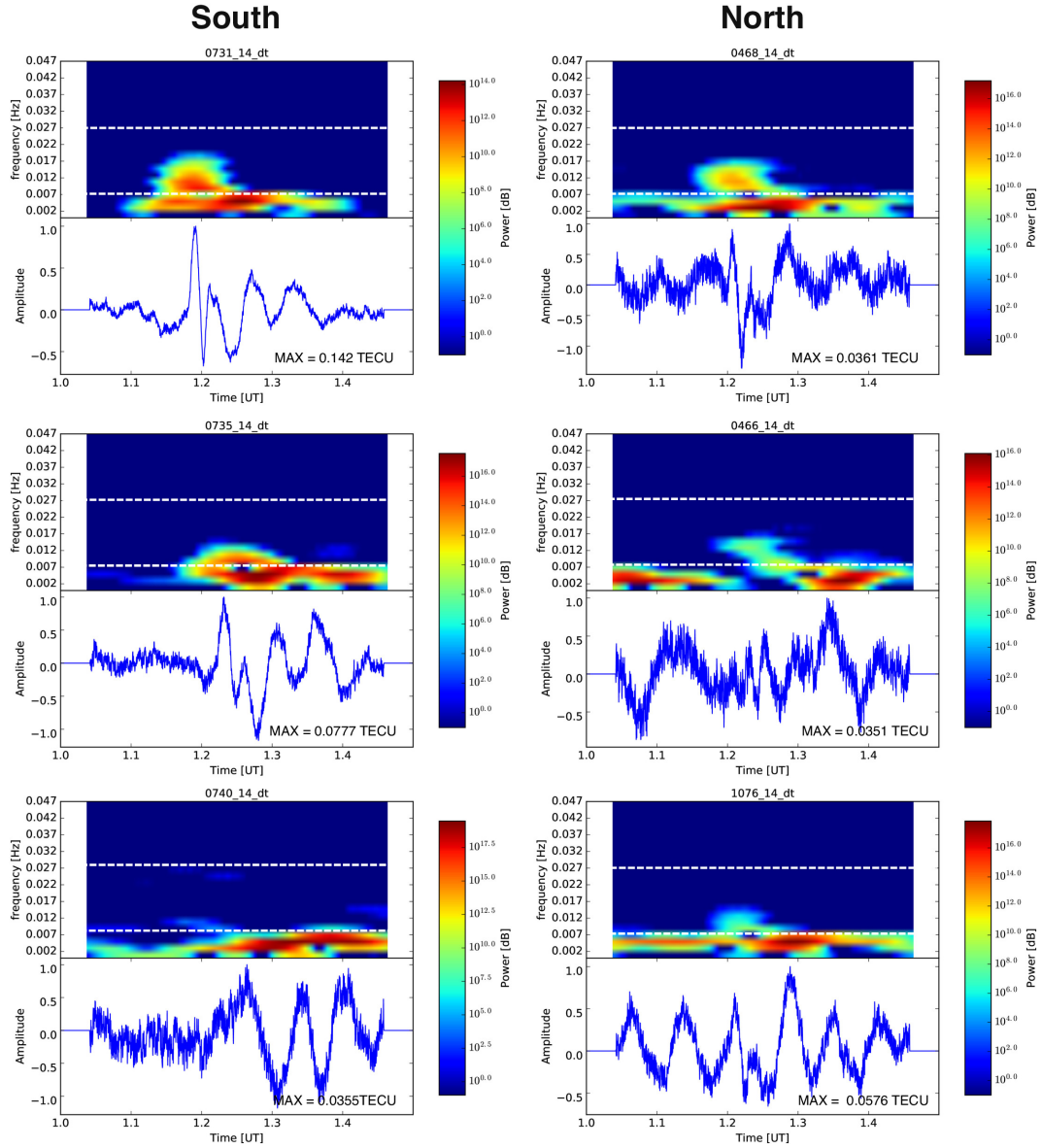


Figure 3.19: Spectrograms plotted by consecutive (moving time window) Fourier transformation of the GNSS-TEC time series. They are computed using time windows as long as 512 sec, and moving the windows with an overlap of 500 sec.

The very low-frequency acoustic wave may be influenced by the gravity. I evaluated its influence by the ray theory, and found that it does not cause serious problems in discussing the travel time of the acoustic wave signals.

I compared travel time curves of the ionospheric disturbances using the synthetic ray paths. I found that the observed travel times of the southward propagating waves are mostly consistent with those inferred from the ray tracing (red curves

in Figure 3.18). However, the arrival times of the northward propagating TEC disturbances showed more difference from calculated travel times (Figure 3.20). The blue curves in these figures assume that the disturbances occur at the uniform altitude. The discrepancy would be due to the difference in the height where the ionospheric perturbations are recorded. The geometry of the line-of-sight relative to the wave front may also cause such discrepancy.

#### 3.3.4.2 Tomographic image of TEC perturbation

I try to extract the structure of the wavefront to interpret the travel time by the GNSS 3D tomography method. The method adopted here is somewhat similar to Garcia et al (2005), who investigated ionospheric disturbances due to horizontal and vertical propagation of waves excited by the passage of seismic Rayleigh wave using the GNSS-TEC data.

I briefly explain technical details of my 3D tomography method. I set up blocks with dimensions of  $0.5^\circ \times 0.5^\circ \times 25$  km in north-south, east-west, and up-down, over the region covering the latitude, longitude, and altitude range of  $(28.15^\circ - 32.65^\circ \times 127.5^\circ - 132.9^\circ \times 75 - 375$  km). The blocks that lack observations are excluded from the calculation (see Figure 3.21 bottom panels). Electron density anomalies are considered as uniform within the individual blocks.

The observation equation of the slant TEC (STEC) residual is described as:

$$\mathbf{y} = \mathbf{A}\mathbf{x} \tag{3.1}$$

Where  $\mathbf{y}$  indicates the observed STEC anomalies obtained using band-pass filter of 4–15 mHz. We collected 2000–3000 GNSS station-satellite pairs at the each time epoch.  $\mathbf{x}$  is a model vector that contains the parameters to be estimated, which corresponds to the electron density anomalies within the blocks.  $\mathbf{A}$  indicates the

Jacobian matrix composed of the line-of-sight (LoS) penetration length through individual blocks.

The parameters can be estimated by solving the normal equation. To solve this, I calculate the inverse of the normal matrix and put it into the equation below.

$$\mathbf{x} = \mathbf{B}^{-1}\mathbf{b} \quad (3.2)$$

$$\begin{aligned} \mathbf{B} &= \mathbf{G}'_{continuity} + \frac{\mathbf{A}^T \mathbf{A}}{\sigma^2} \\ \mathbf{b} &= \mathbf{A}^T \mathbf{y} \end{aligned}$$

The matrix  $\mathbf{G}'_{continuity}$  indicates the continuity constraint to regularize the normal matrix, and I used the continuity constraint of  $0.15 \times 10^9 \text{ electrons}/m^3$ . To derive  $\mathbf{B}^{-1}$ , I used the Cholesky decomposition algorithm.  $\mathbf{y}$  indicates the assumed standard deviation of the observation. I assumed it as 0.1 TECU.

Here I show the 3D tomography results at three time epochs. Together with the results with the real data set, the results of the checkerboard resolution test are shown for reference (Figure 3.21). Because the results of the test constantly change with time because the satellites move in the space. So I always put the resolution test results next to those with the real data to confirm which parts of the results are more/less reliable.

(a) 01:08:30–01:09:15

At the epoch 01:08:45 UT, Figure 3.20 indicates that the wave did not reach the altitude of  $\sim 300$  km above the surface. In the 3D tomography results with the real data set show clear wave front only at the southern side of the volcano. This reflects the north-south signal strength asymmetry due to interaction of electrons with geomagnetic fields, i.e., the signal of



the southward propagating wave is  $\sim 10$  times as large as those propagating northwards.

(b) 01:11:00–01:11:45

At the epoch of 01:11:00 UT, the wave front is thought to have reached the height of the largest electrons density (around 300 km above) (Figure 3.25). The amplitude of the positive anomaly is larger than in Figure 3.22, reflecting the higher electron density at the F region. The wavefront is again clear only at the southern side of the volcano. Another notable feature is that the wavefront is more vertical than in the previous epoch. This is consistent with the ray tracing results shown in Figure 3.10 where the ray paths are nearly parallel with the ground at the F region height.

(c) 01:17:45–01:18:30

At this epoch, the tomography results show the negative part of the initial N-shaped wave, and the succeeding oscillation with the atmospheric mode frequency. The wavefront is, however, not so clear as in earlier epochs. (Figure 3.18).

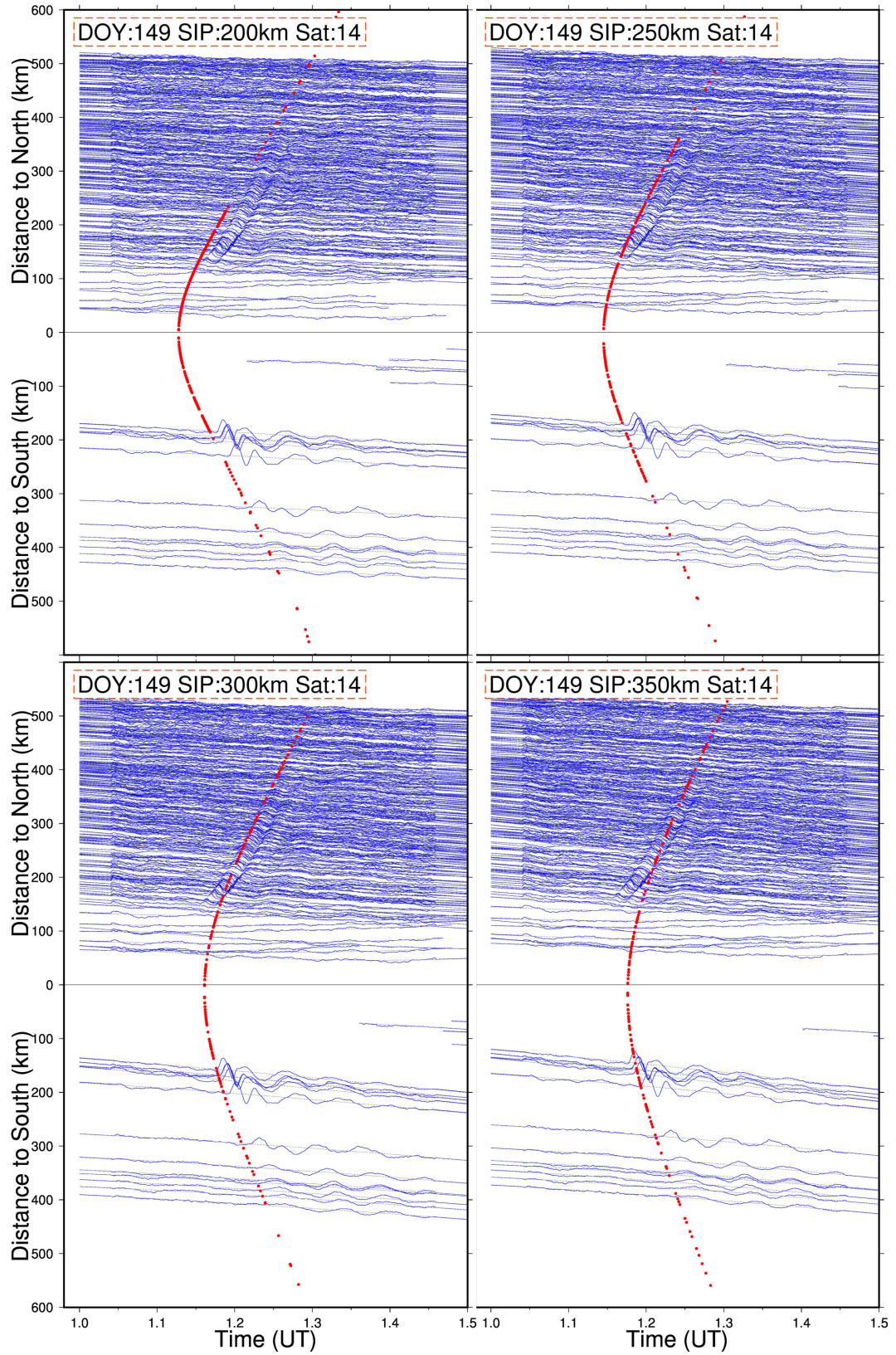


Figure 3.20: Blue curves show travel time diagrams of TEC perturbations from GPS Sat.14 assuming the height of the IPPs at 200, 250, 300 and 350 km. Curves in red indicate arrival times of waves calculated by ray tracing as shown in Figure 3.10.

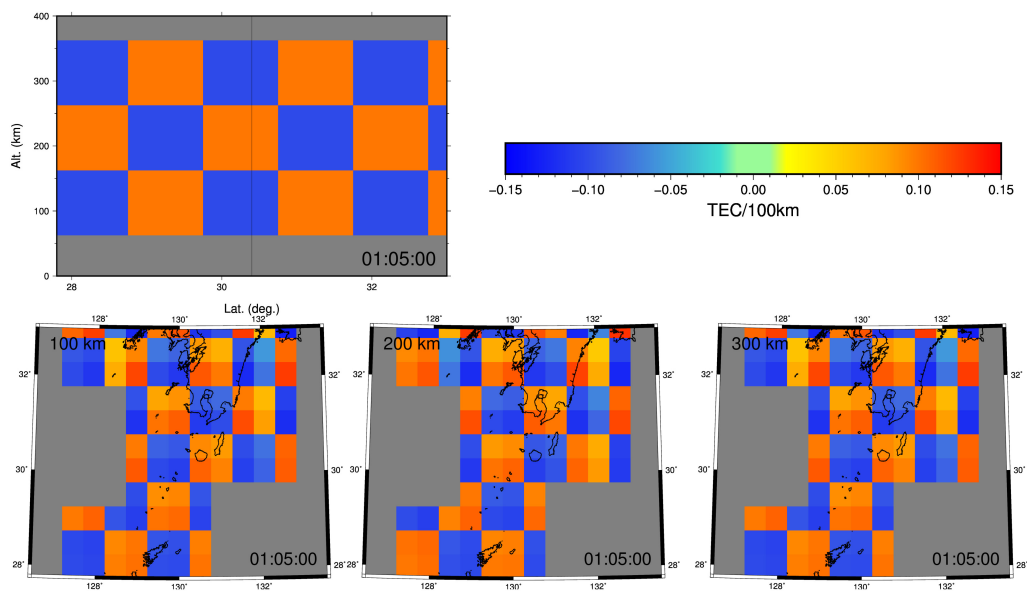


Figure 3.21: The input image of the checker board test (top: north-south profile, bottom: map view at three different altitudes). The grid interval is  $1 \text{ degree} \times 1 \text{ degree} \times 100 \text{ km}$ .

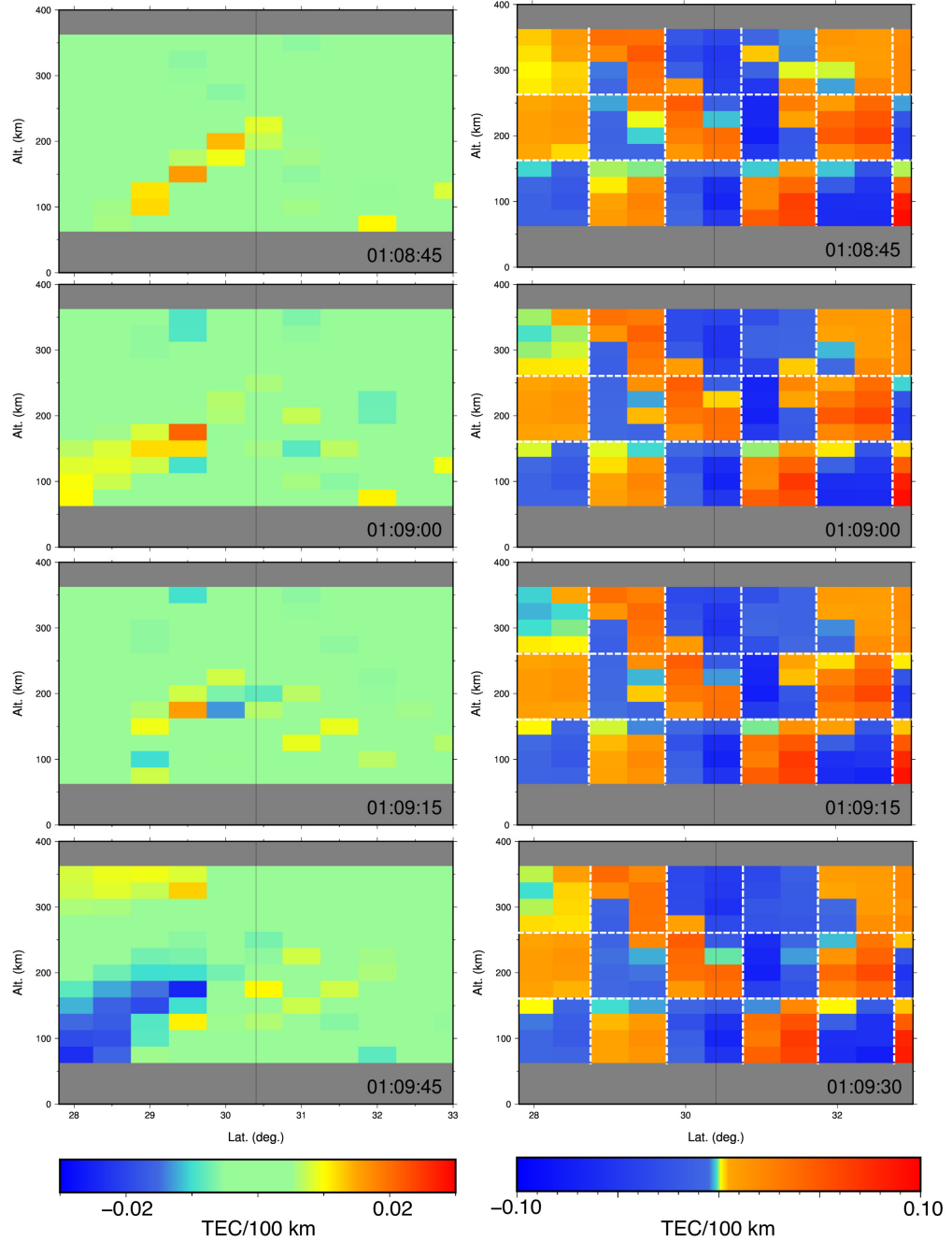


Figure 3.22: North-South profile of the results of the 3D tomography of electron density anomalies from 01:08:45 to 01:09:15 UT using the STEC residuals derived by GNSS-TEC observations as the input. Right: Checkerboard test results using the synthetic data. Left: Results with the real observation data.

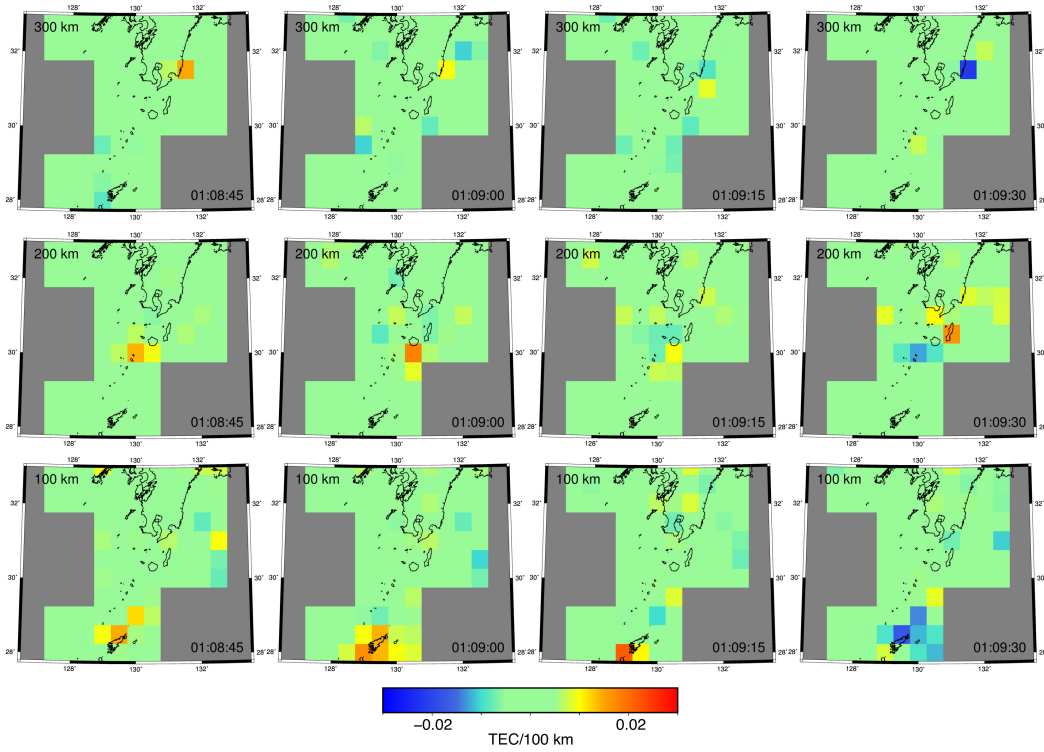


Figure 3.23: Map view of the results of the 3D tomography of electron density anomalies from 01:08:30 to 01:09:15 UT. They are all results with the real observation data.

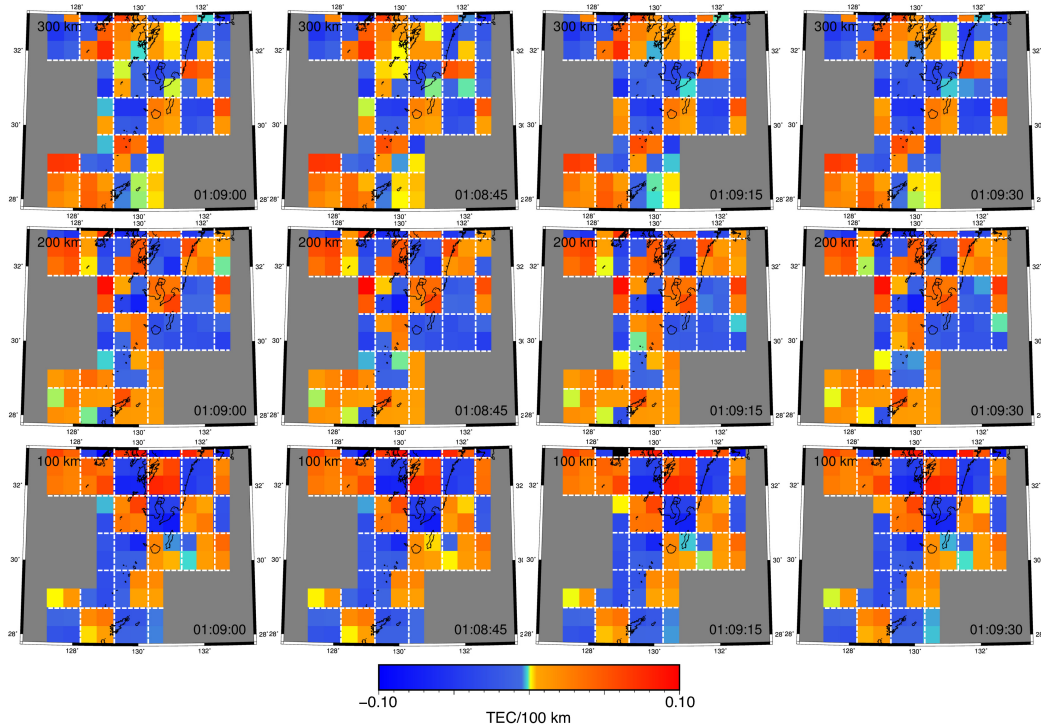


Figure 3.24: Map view of the results of the 3D tomography of electron density anomalies from 01:08:30 to 01:09:15 UT. They are all results of the checkerboard test results with synthetic data.

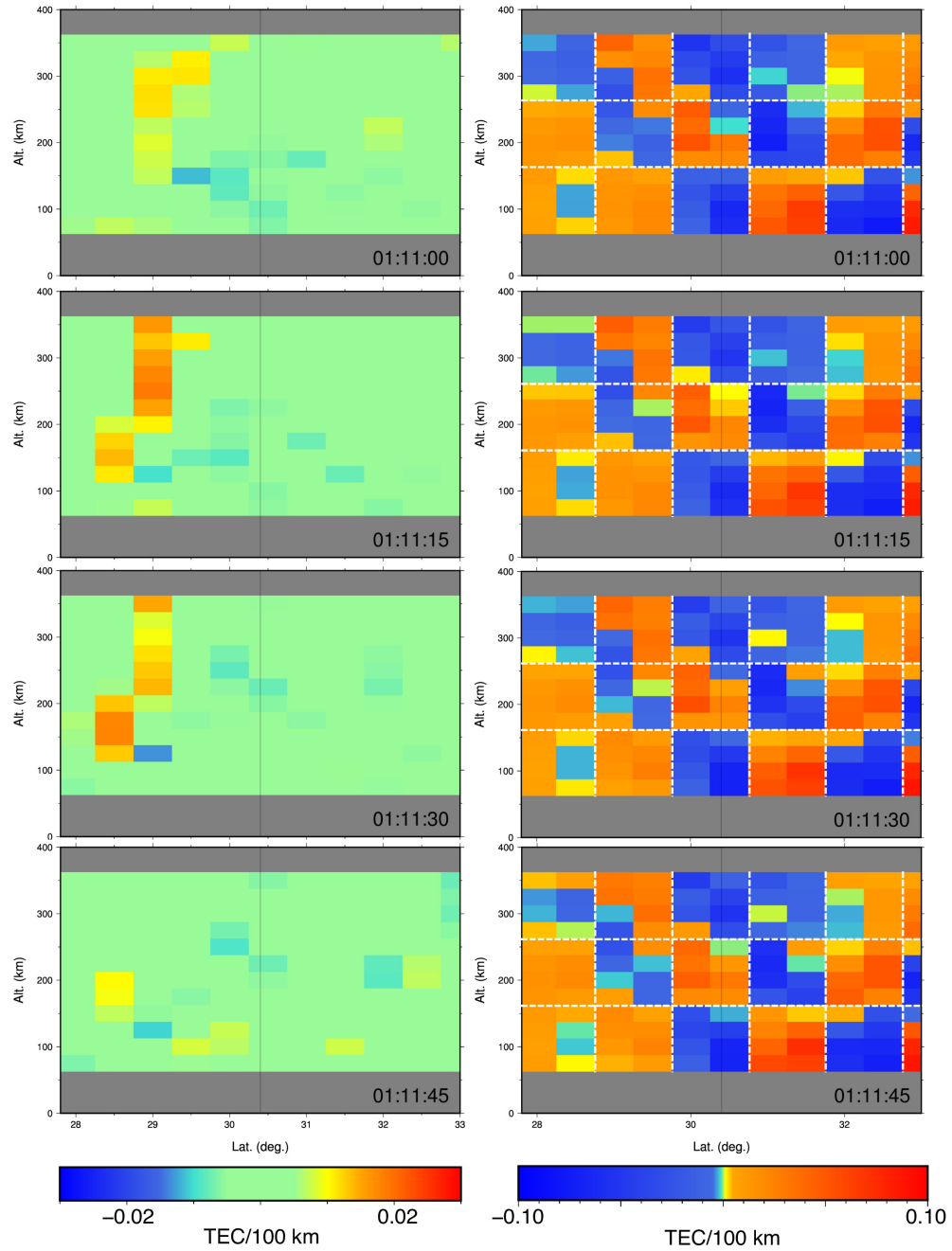


Figure 3.25: North–South profile of the results of the 3D tomography of electron density anomalies from 01:11:00 to 01:11:45 UT. Left: Results with real observation data. Right: Checkerboard test results.



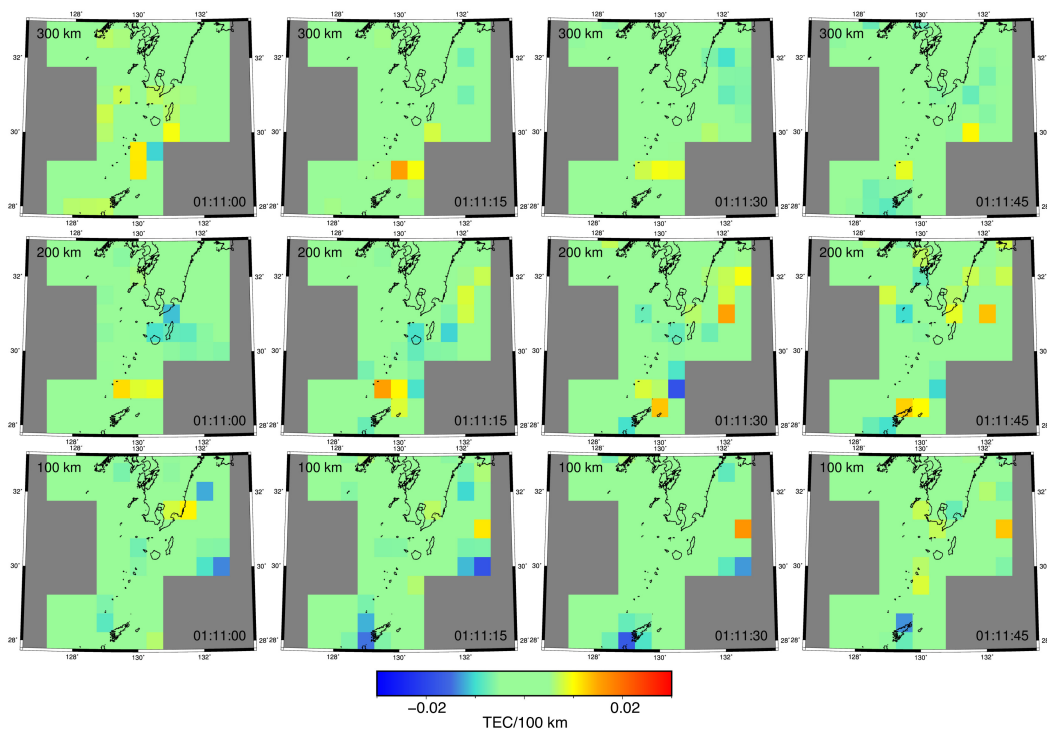


Figure 3.26: Map view of the results of the 3D tomography of electron density anomalies from 01:11:00 to 01:11:45 UT. Results with real observation data.

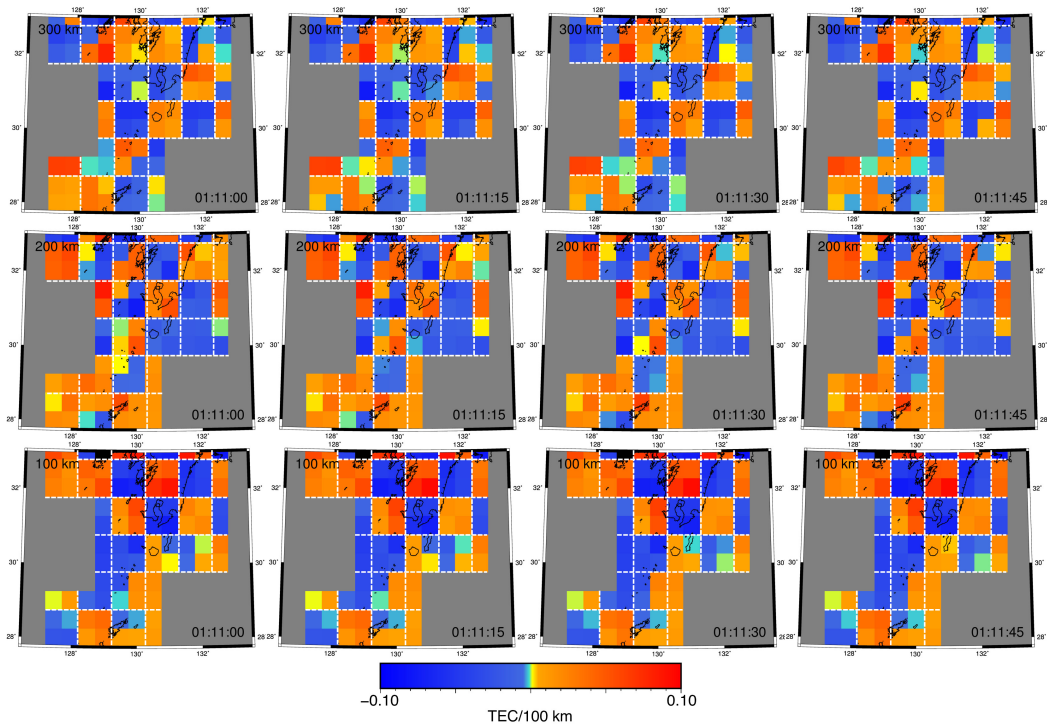


Figure 3.27: Map view of the results of the 3D tomography of electron density anomalies from 01:11:00 to 01:11:45 UT. Checkerboard test results.

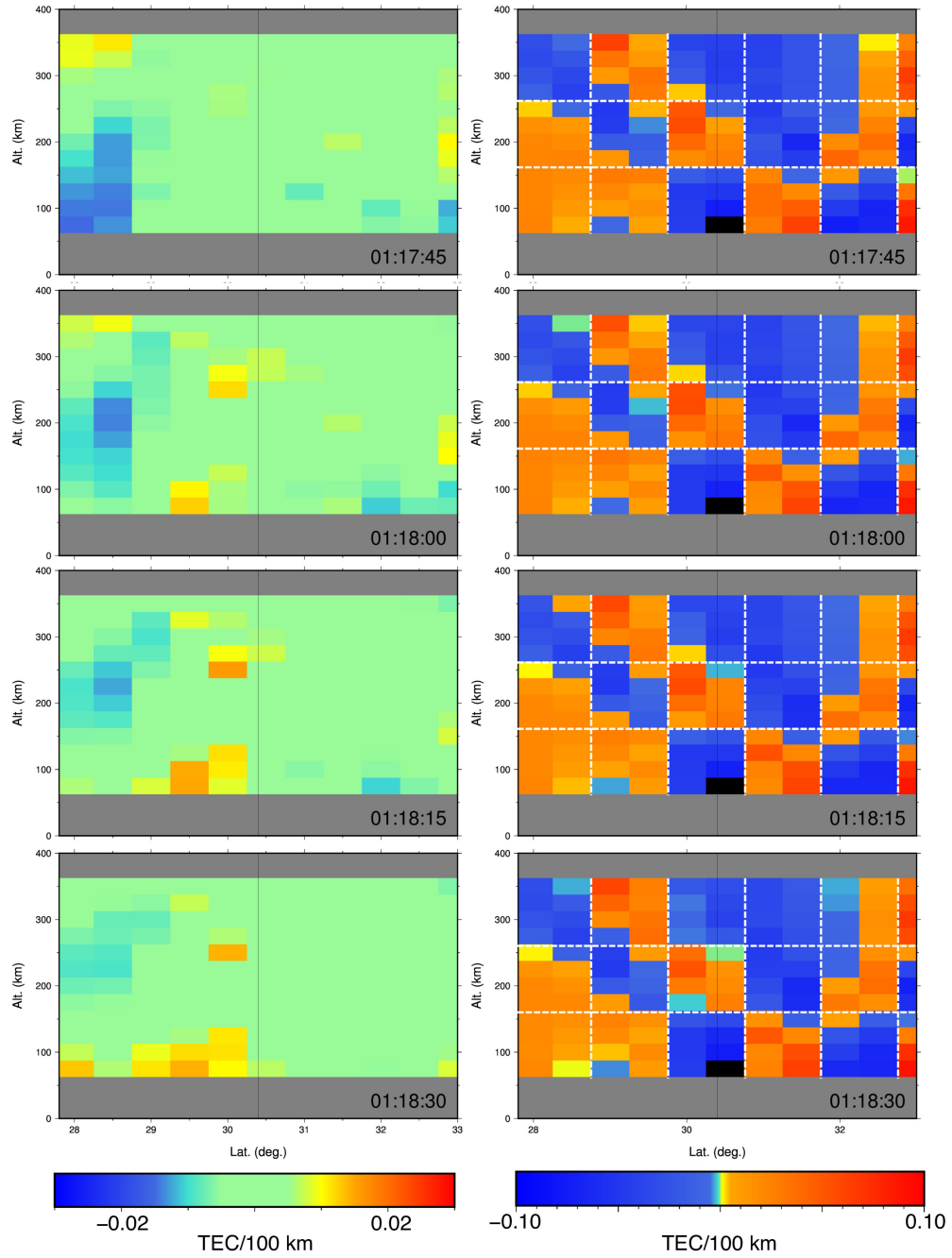


Figure 3.28: North–South profile of the results of the 3D tomography of electron density anomalies from 01:17:45 to 01:18:30 UT. Top: Checkerboard test results. Bottom: Results with real observation data.



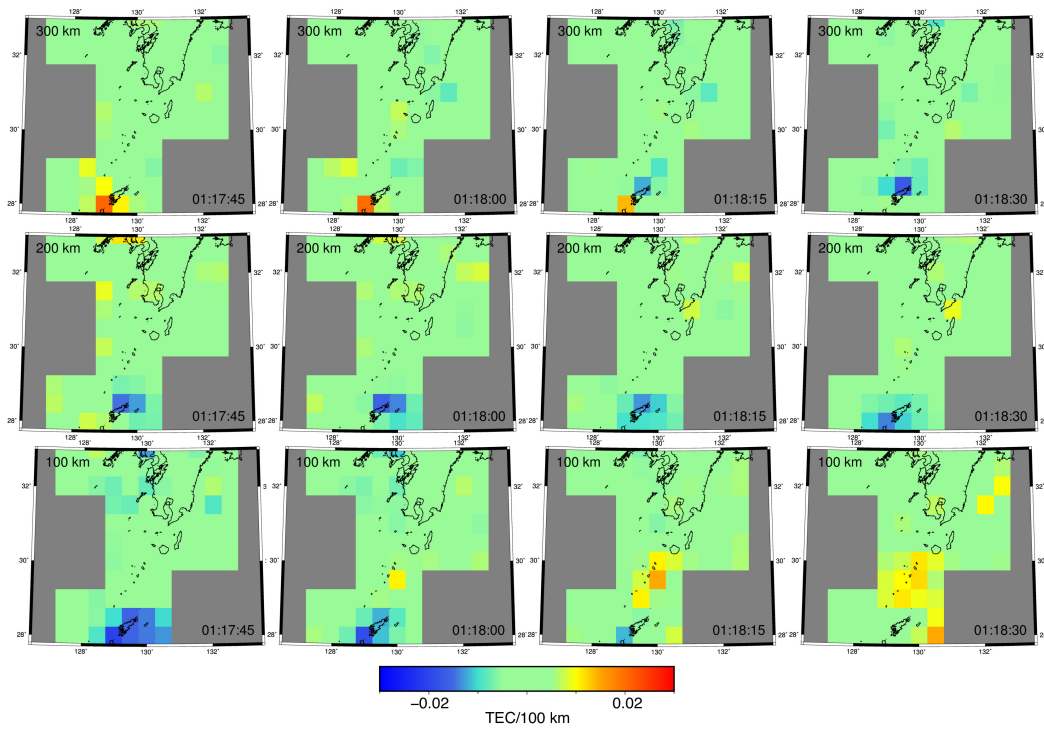


Figure 3.29: Map view of the results of the 3D tomography of electron density anomalies from 01:17:45 to 01:18:30 UT. Results with real observation data.

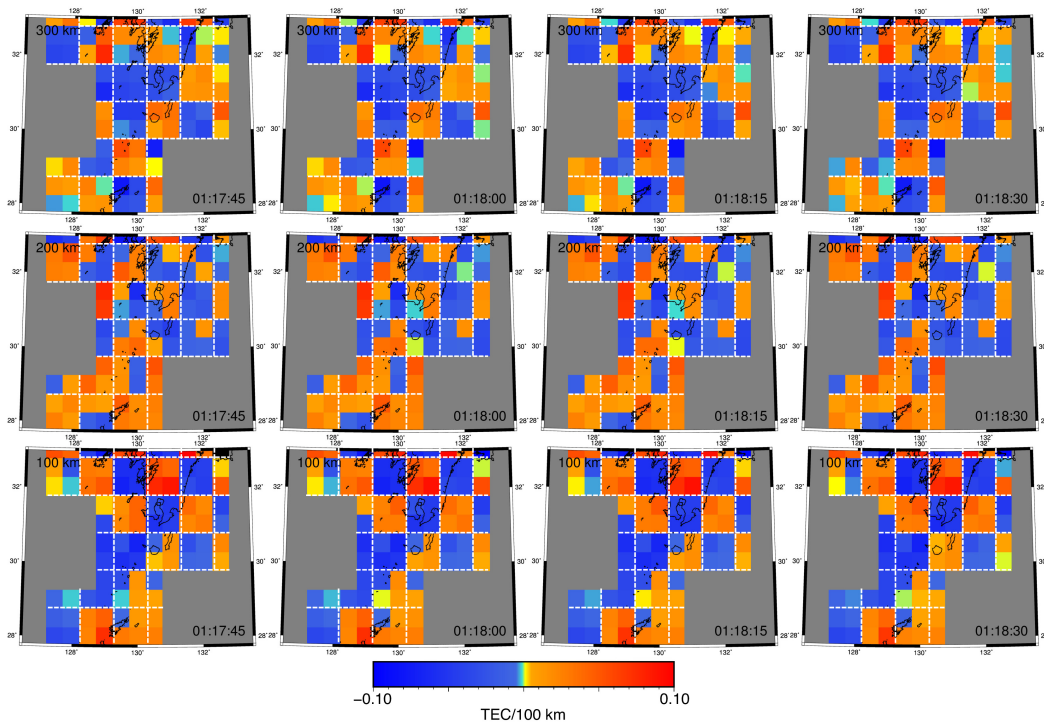


Figure 3.30: Map view of the results of the 3D tomography of electron density anomalies from 01:17:45 to 01:18:30. Checkerboard test results.

### 3.3.4.3 Summary of the section

The signals of the 2015 Kuchinoerabujima volcano eruption recorded in multiple sensors were found to have a simple pattern: an acoustic pulse followed by resonance signals lasting for a few tens of minutes. We could consider this as the typical atmospheric response to a single point-source explosion.

1. Atmospheric perturbations by the 2015 Kuchinoerabujima volcano eruption were detected near surface by barometers and broad-band seismometers. Subsidence in the seismometer record corresponds to the pressure increase in the barometric record suggesting the elastic crustal response to the enhanced pressure.
2. Seismometer records are composed of fast components and slow components, and the latter corresponds to the crustal response to the atmospheric waves.
3. Travel times of the atmospheric wave signatures in both the barometer and the seismometer were consistent with the simple ray tracing results.
4. The upward propagating atmospheric wave was detected as ionospheric TEC disturbances in the near field ( $< 500$  km) using the dense GNSS array, GEONET.
5. The initial N-shaped TEC perturbation with the frequency of about 0.01 Hz would correspond to the positive (subsidence) pulse in the barometric (seismometric) observations. The change in the period (pulse width is about 30 seconds near the surface, and longer than one minute in ionosphere) would reflect the atmospheric band-pass filtering effect as shown in Figure 1.1.
6. The travel times of the ionospheric TEC oscillations were compared with those calculated by ray tracing of an acoustic wave from a point source.

7. The N-shaped TEC perturbation was followed by the oscillation with frequency of about 5 mHz and lasting about 15 minutes. This would be the atmospheric mode excited by the explosive atmospheric perturbation. This 5 mHz wave was not observed in the barometric or seismometric records.

## Chapter 4

# Features of atmospheric disturbances by volcanic eruptions

In Chapter 4, I describe the features of atmospheric waves by volcanic eruptions and their excitation mechanisms, interpreting the observation results given in Chapter 3. Ionospheric disturbances by volcanic eruptions include various frequency components and characteristic waveforms. Atmospheric waves observed in the near field, especially TEC perturbations discussed in Chapter 3, have two styles: one is the  $> \sim 10$  mHz N-shaped pulses and the other is the several mHz continuous modal waves. According to past studies, the former type wave was excited by the 2004 Asamayama volcano eruption, and the latter type wave was detected when the Soufrière Hills volcano, the West Indies, erupted in 2013.

At the beginning of the thesis, I reviewed reports of ionospheric disturbances excited by a number of past volcanic eruptions, and showed that they have various styles of waveforms, frequency components, and durations. Such diversities reflect the eruption sequences of individual volcanoes. An explosive eruption represented by Vulcanian eruptions makes a strong pressure pulse in the air. The pulse often

emerges as an N-shaped disturbance not only near the volcano but also in the ionosphere hundreds of kilometers away as TEC changes. Typical examples, recently observed in Japan, include the 2004 eruption of the Asama volcano and the 2015 eruption of the Kuchinoerabujima volcano.

On the other hand, a Plinian eruption causes continuous jet flow lasting for several hours. This style of eruption can excite continuous oscillation of TEC with a few distinct frequency components corresponding to the acoustic trap modes. I reported a typical example from the 2015 eruption of the Calbuco volcano, Chile, and compared it with the earlier case of the 2014 eruption of the Kelud volcano, Indonesia.

Fortunately, ionospheric disturbances of the 2015 eruption of the Kuchinoerabujima volcano were recorded by 1 Hz sampling with the dense network of GNSS stations in Japan. This allowed me to find two different kinds of waves, i.e., not only N-shaped initial disturbances, but also harmonic oscillation lasting for half an hour in the TEC time series. Hence, this is the first example of the hybrid case composed of the initial pressure pulse, often accompanying Vulcanian eruptions, and later atmospheric modes that have been found only after Plinian eruptions so far.

The higher frequency ( $> \sim 10$  mHz) components of TEC oscillation by the 2015 Kuchinoerabujima eruption is similar to the signal excited by the 2004 Asama eruption (Heki, 2006). Using the ray tracing results, I demonstrated that the atmospheric waves in the ionosphere and the air shock pulse near the surface, observed by barometers and seismometers on the ground, come from the same point source. Volcanic N-shaped TEC signals have periods shorter than the typical periods of shock acoustic wave signals ( $\sim 240$ – $360$  sec) made by large earthquakes. The difference seems to stem from the source time functions of the phenomena. A Volcanic eruption makes a short atmospheric pulse, and it would become an N-shaped TEC pulse by going through the atmospheric band-pass filter. On the other hand, vertical crustal movement in a large earthquake is a step function, and

causes an atmospheric wave with components extending to much lower frequencies. Such waves might become a pulse with the frequency close to the acoustic cut-off by going through the atmospheric band-pass filter.

Now I further discuss the TEC oscillation following the N-shaped pulse after

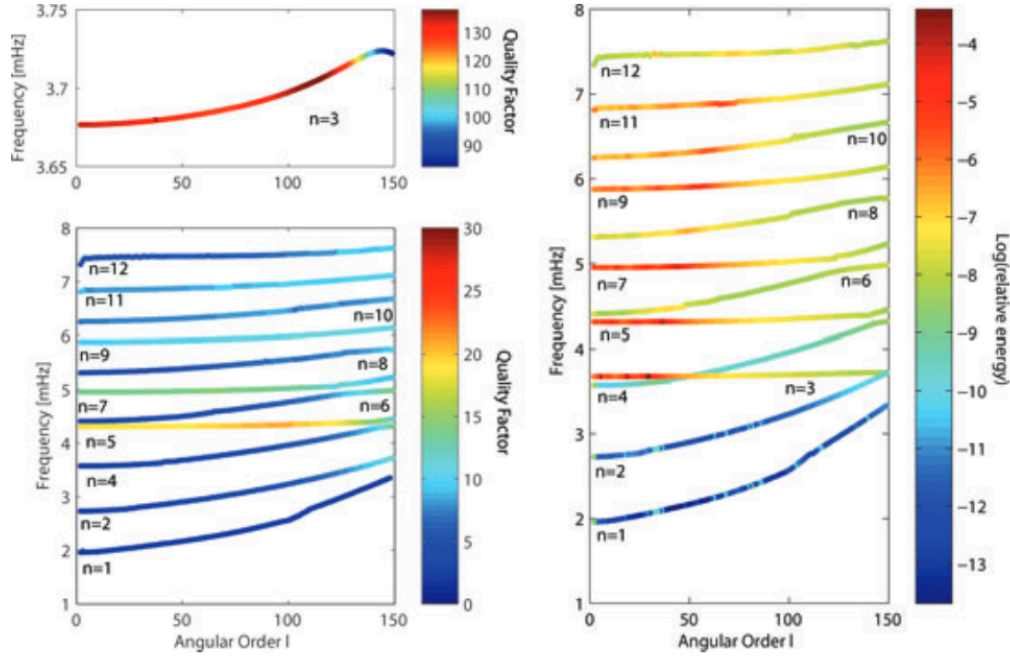


Figure 4.1: Left-hand panels: quality factor ( $Q$ ) for the atmospheric modes. High values of  $Q$  correspond to low damping. Mode branch  $n = 3$  is separated out in the top left panel, since  $Q$  is one order of magnitude higher for this branch. Right-hand panel: normalized energy for the atmospheric modes. (cited from [Dautermann et al, 2009b](#), Figure 5)

the Kuchinoerabujima volcano eruption. The continuous TEC oscillation has a similar frequency,  $\sim 5$  mHz, to past examples of Plinian eruptions, and is considered to represent the atmospheric trap mode. I also showed in Chapter 3 that it propagated with spherical wavefronts. However, this oscillation has a distinct difference from past examples, i.e. it has a much shorter duration, and did not last for a long time. This might be because the eruption was a single explosive event and not a continuous excitation of atmospheric turbulences. The situation might represent the results of the calculation done by [Dautermann et al \(2009a\)](#), who showed the  $Q$  values of multiple overtones (Figure 4.1). Their calculation assumed

an explosive source and failed to reproduce the duration of the TEC oscillation. According to their results, the eruption seems to have excited the acoustic trap modes whose  $Q$  values are not so large, e.g.  $n = 7$  or  $n = 5$  (Figure 4.1).

The TEC oscillation observed after the 2003 eruption of the Soufrière Hills volcano investigated by [Dautermann et al \(2009b\)](#) and [Dautermann et al \(2009a\)](#) is also interesting. The waveform resembles to a Plinian type TEC perturbation:  $\sim 4$  mHz oscillation lasting about 2–3 hours. Furthermore, this atmospheric oscillation appears to have coupled with solid earth exciting ground oscillation lasting about 1 hour. Another interesting feature is that they cannot find any N-shaped pulses like the one observed in the 2015 Kuchinoerabujima eruption. Volcanologist did not report any Plinian eruptions about the 2003 event ([Herd et al, 2005](#)). Figure 1.6 indicates that the harmonic oscillation of TEC occurred when the eruption sequence reached the most violent period. The eruption duration is not clearly reported in the literature, and they reported only water-associated events. It suggests that the eruption excited the TEC oscillation as a result of phreatomagmatic eruption that lasted for a while in a sub-Plinian style. Another possibility might be a semi-continuous occurrence of a pyroclastic flow by collapsing volcanic column. Such events are known to occur frequently in that volcano. This process might be able to cause enough turbulence and excite acoustic modal waves just like the 2014 Kelud eruption case.

# Chapter 5

## Conclusions

In this chapter, I will describe the conclusions.

The main conclusions of this thesis can be summarized as follows:

1. I performed a systematic and comprehensive study of atmospheric disturbances by recent volcanic eruptions, e.g., the 2015 Vulcanian explosion of the Kuchinoerabujima volcano, Japan, Plinian eruptions of the Kelud volcano, Indonesia, in 2014 and the Calbuco volcano, Chile, in 2015
2. I used barometers and seismometers to observe waves near the ground, and the GNSS-TEC technique to observe those in the ionosphere; for the Kuchinoerabujima case, I used high-rate (1 second sampling) GNSS carrier phase data
3. By comparing signals propagating in the lower and upper atmosphere, I confirmed that they originate from the same source
4. After Vulcanian explosions, I found N-shaped impulsive disturbances occur  $\sim 10$  minutes after the explosions
5. In the Kuchinoerabujima case, I also detected 5 mHz continuous wave propagating in the ionosphere



6. I tried to visualize spherical wave fronts by performing 3D tomography of ionospheric electron density anomalies for the Kuchinoerabujima case
7. For the two Plinian eruption cases, I observed that continuous fluctuations of TEC lasted for hours with frequencies consistent with known atmospheric resonance frequencies

# Bibliography

- Afraimovich EL, Perevalova NP, Plotnikov AV, Uralov AM (2001) The shock-acoustic waves generated by earthquakes. *Annales Geophysicae* 19(4):395–409, DOI 10.5194/angeo-19-395-2001, [0007041](#)
- Aoyama T, Iyemori T, Nakanishi K, Nishioka M, Rosales D, Veliz O, Safor EV (2016) Localized field-aligned currents and 4-min TEC and ground magnetic oscillations during the 2015 eruption of Chile’s Calbuco volcano. *Earth, Planets and Space* 68(1):148, DOI 10.1186/s40623-016-0523-0
- Ben-Menahem A, Singh SJ (1981) *Seismic Waves and Sources*, 1st edn. Springer New York, New York, NY, DOI 10.1007/978-1-4612-5856-8
- Bilitza D, McKinnell LA, Reinisch B, Fuller-Rowell T (2011) The international reference ionosphere today and in the future. *Journal of Geodesy* 85(12):909–920, DOI 10.1007/s00190-010-0427-x
- Blanc E (1985) Observations in the upper atmosphere of infrasonic waves from natural or artificial sources - A summary. *Annales Geophysicae* 3:673–687
- Bolt BA, Tanimoto T (1981) Atmospheric oscillations after the May 18, 1980 eruption of Mount St. Helens. *Eos, Transactions American Geophysical Union* 62(23):529–530, DOI 10.1029/EO062i023p00529

- Cas RAF, Wright JV (1987) Volcanic successions, modern and ancient : a geological approach to processes, products, and successions. London ; Boston : Allen & Unwin
- Caudron C, Taisne B, Garcés M, Alexis LP, Mialle P (2015) On the use of remote infrasound and seismic stations to constrain the eruptive sequence and intensity for the 2014 Kelud eruption. *Geophysical Research Letters* 42(16):6614–6621, DOI 10.1002/2015GL064885
- Cheng K, Huang YN (1992) Ionospheric disturbances observed during the period of Mount Pinatubo eruptions in June 1991. *Journal of Geophysical Research* 97(A11):16,995, DOI 10.1029/92JA01462
- Choosakul N, Saito A, Iyemori T, Hashizume M (2009) Excitation of 4-min periodic ionospheric variations following the great Sumatra-Andaman earthquake in 2004. *Journal of Geophysical Research* 114(A10):A10,313, DOI 10.1029/2008JA013915
- Dautermann T, Calais E, Lognonné P, Mattioli GS (2009a) Lithosphere-atmosphere-ionosphere coupling after the 2003 explosive eruption of the Soufriere Hills Volcano, Montserrat. *Geophysical Journal International* 179(3):1537–1546, DOI 10.1111/j.1365-246X.2009.04390.x
- Dautermann T, Calais E, Mattioli GS (2009b) Global Positioning System detection and energy estimation of the ionospheric wave caused by the 13 July 2003 explosion of the Soufrière Hills Volcano, Montserrat. *Journal of Geophysical Research* 114(B2):B02,202, DOI 10.1029/2008JB005722
- Delclos C, Blanc E, Broche P, Glangeaud F, Lacoume JL (1990) Processing and interpretation of microbarograph signals generated by the explosion of Mount St. Helens. *Journal of Geophysical Research* 95(D5):5485, DOI 10.1029/JD095iD05p05485

- Donn WL, Balachandran NK (1981) Mount St. Helens Eruption of 18 May 1980: Air Waves and Explosive Yield. *Science* 213(4507):539–541, DOI 10.1126/science.213.4507.539
- Dziewonski AM, Anderson DL (1981) Preliminary reference Earth model. *Physics of the Earth and Planetary Interiors* 25(4):297–356, DOI 10.1016/0031-9201(81)90046-7
- Fee D, Matoza RS (2013) An overview of volcano infrasound: From hawaiian to plinian, local to global. *Journal of Volcanology and Geothermal Research* 249:123–139, DOI 10.1016/j.jvolgeores.2012.09.002
- Garcia R, Crespon F, Ducic V, Lognonné P (2005) Three-dimensional ionospheric tomography of post-seismic perturbations produced by the Denali earthquake from GPS data. *Geophysical Journal International* 163(3):1049–1064, DOI 10.1111/j.1365-246X.2005.02775.x
- Global Volcanism Program (2013) *Volcanoes of the World*, v. 4.6.3. DOI 10.5479/si.GVP.VOTW4-2013
- Harkrider D, Press F (1967) The Krakatoa Air-Sea Waves: an Example of Pulse Propagation in Coupled Systems. *Geophysical Journal International* 13(1-3):149–159, DOI 10.1111/j.1365-246X.1967.tb02150.x
- Heki K (2006) Explosion energy of the 2004 eruption of the Asama Volcano, central Japan, inferred from ionospheric disturbances. *Geophysical Research Letters* 33(14):L14,303, DOI 10.1029/2006GL026249
- Herd RA, Edmonds M, Bass VA (2005) Catastrophic lava dome failure at Soufrière Hills Volcano, Montserrat, 12–13 July 2003. *Journal of Volcanology and Geothermal Research* 148(3-4):234–252, DOI 10.1016/j.jvolgeores.2005.05.003
- Igarashi K, Kainuma S, Nishimuta I, Okamoto S, Kuroiwa H, Tanaka T, Ogawa T (1994) Ionospheric and atmospheric disturbances around Japan caused by

- the eruption of Mount Pinatubo on 15 June 1991. *Journal of Atmospheric and Terrestrial Physics* 56(9):1227–1234, DOI 10.1016/0021-9169(94)90060-4
- IGS, RTCM-SC104 (2012) RINEX : The Receiver Independent Exchange Format Version 3.03. Tech. Rep., International GNSS Service
- Kanamori H, Mori J (1992) Harmonic excitation of mantle Rayleigh waves by the 1991 eruption of Mount Pinatubo, Philippines. *Geophysical research letters* 19(7):721–724
- Kanamori H, Given JW, Lay T (1984) Analysis of seismic body waves excited by the Mount St. Helens eruption of May 18, 1980. *Journal of Geophysical Research: Solid Earth* 89(B3):1856–1866, DOI 10.1029/JB089iB03p01856
- Kanamori H, Mori J, Harkrider DG (1994) Excitation of atmospheric oscillations by volcanic eruptions. *Journal of Geophysical Research: Solid Earth* 99(B11):21,947–21,961, DOI 10.1029/94JB01475
- Liu CH, Klostermeyer J, Yeh KC, Jones TB, Robinson T, Holt O, Leiting R, Ogawa T, Sinno K, Kato S, Ogawa T, Bedard AJ, Kersley L (1982) Global dynamic responses of the atmosphere to the eruption of Mount St. Helens on May 18, 1980. *Journal of Geophysical Research* 87(A8):6281, DOI 10.1029/JA087iA08p06281
- Maeno F, Nakada S, Yoshimoto M, Shimano T, Hokanishi N, Zaennudin A, Iguchi M (2017) A sequence of a plinian eruption preceded by dome destruction at Kelud volcano, Indonesia, on February 13, 2014, revealed from tephra fallout and pyroclastic density current deposits. *Journal of Volcanology and Geothermal Research* 1951, DOI 10.1016/j.jvolgeores.2017.03.002
- Matsuzawa T, Matsumoto T, Tanada T (2016) Seismic inversion analysis of the 2014 and 2015 Kuchinoerabujima volcanic eruptions, using F-net broadband seismometers. *Journal of Natural Disaster Science* 37(2):91–103

- Mikumo T (2011) Atmospheric Pressure Waves Generated from Large Earthquakes, Tsunamis and Large Volcanic Eruptions. *Zisin* (Journal of the Seismological Society of Japan 2nd ser) 64(1):47–62, DOI 10.4294/zisin.64.47
- Mikumo T, Bolt BA (1985) Excitation mechanism of atmospheric pressure waves from the 1980 Mount St Helens eruption. *Geophysical Journal International* 81(2):445–461, DOI 10.1111/j.1365-246X.1985.tb06412.x
- Nakashima Y, Heki K, Takeo A, Cahyadi MN, Aditiya A, Yoshizawa K (2016) Atmospheric resonant oscillations by the 2014 eruption of the Kelud volcano, Indonesia, observed with the ionospheric total electron contents and seismic signals. *Earth and Planetary Science Letters* 434:112–116, DOI 10.1016/j.epsl.2015.11.029
- Nanometrics Inc (2005) Trillium 240 Seismometer User Guide. Tech. Rep., Nanometrics Inc., Kanata, Ontario, Canada
- Nishida K, Kobayashi N, Fukao Y (2000) Resonant Oscillations Between the Solid Earth and the Atmosphere. *Science* 287(5461):2244–2246, DOI 10.1126/science.287.5461.2244
- Nishioka M, Tsugawa T, Kubota M, Ishii M (2013) Concentric waves and short-period oscillations observed in the ionosphere after the 2013 Moore EF5 tornado. *Geophysical Research Letters* 40(21):5581–5586, DOI 10.1002/2013GL057963
- Occhipinti G, Kherani EA, Lognonné P (2008) Geomagnetic dependence of ionospheric disturbances induced by tsunamigenic internal gravity waves. *Geophysical Journal International* 173(3):753–765, DOI 10.1111/j.1365-246X.2008.03760.x
- Ogawa T, Kumagai H, Sinno K (1982) Ionospheric disturbances over Japan due to the 18 May 1980 eruption of Mount St. Helens. *Journal of Atmospheric and Terrestrial Physics* 44(10):863–868, DOI 10.1016/0021-9169(82)90039-3

- Ohminato T, Takeo M, Kumagai H, Yamashina T, Oikawa J, Koyama E, Tsuji H, Urabe T (2006) Vulcanian eruptions with dominant single force components observed during the Asama 2004 volcanic activity in Japan. *Earth, Planets and Space* 58(5):583–593, DOI 10.1186/BF03351955
- Press F, Harkrider D (1966) Air-Sea Waves from the Explosion of Krakatoa. *Science* 154(3754):1325–1327, DOI 10.1126/science.154.3754.1325
- Roberts D, Rogers A (1982) Radio interferometric detection of a traveling ionospheric disturbance excited by the explosion of Mount St. Helens. *Journal of Geophysical Research: Space Physics* 87(A8):6302, DOI 10.1029/JA087iA08p06302
- Roberts DH, Klobuchar JA, Fougere PF, Hendrickson DH (1982) A large-amplitude traveling ionospheric disturbance produced by the May 18, 1980, explosion of Mount St. Helens. *Journal of Geophysical Research* 87(A8):6291, DOI 10.1029/JA087iA08p06291
- Rolland LM, Lognonn P, Astafyeva E, Kherani EA (2011) The resonant response of the ionosphere imaged after the 2011 off the Pacific coast of Tohoku Earthquake. *Earth, Planets and Space* 63(7):853–857, DOI 10.5047/eps.2011.06.020
- Saito A, Tsugawa T, Otsuka Y, Nishioka M, Iyemori T, Matsumura M, Saito S, Chen CH, Goi Y, Choosakul N (2011) Acoustic resonance and plasma depletion detected by GPS total electron content observation after the 2011 off the Pacific coast of Tohoku Earthquake. *Earth, Planets and Space* 63(7):863–867, DOI 10.5047/eps.2011.06.034
- Shults K, Astafyeva E, Adourian S (2016) Ionospheric detection and localization of volcano eruptions on the example of the April 2015 Calbuco events. *Journal of Geophysical Research A: Space Physics* 121(10):10,303–10,315, DOI 10.1002/2016JA023382

- Strachey R (1983) Explosive air waves and sounds. In: Simkin T, Fiske RS (eds) Krakatau, 1883–the volcanic eruption and its effects, 1st edn, Smithsonian, pp 368–374
- Sulaksana N, Sukiyah E, Sudradjat A, Syafri I (2014) The Crater Configuration of Kelud Volcano, East Java, Indonesia after the 2014 Eruption. *International Journal of Science and Research* 3(3):419–422
- VAISALA (1997) PTB100 Series Analogue Barometers PTB100 SERIES ANALOGUE BAROMETERS. Tech. Rep., VAISALA, Helsinki, Finland
- Van Eaton AR, Amigo Á, Bertin D, Mastin LG, Giacosa RE, González J, Valderama O, Fontijn K, Behnke SA (2016) Volcanic lightning and plume behavior reveal evolving hazards during the April 2015 eruption of Calbuco volcano, Chile. *Geophysical Research Letters* 43(7):3563–3571, DOI 10.1002/2016GL068076
- Walker GPL (1973) Explosive volcanic eruptions —a new classification scheme. *Geologische Rundschau* 62(2):431–446, DOI 10.1007/BF01840108
- Watada S, Kanamori H (2010) Acoustic resonant oscillations between the atmosphere and the solid earth during the 1991 Mt. Pinatubo eruption. *Journal of Geophysical Research* 115(B12):B12,319, DOI 10.1029/2010JB007747
- Widmer R, Zürn W (1992) Bichromatic excitation of long-period Rayleigh and air waves by the Mount Pinatubo and El Chichon volcanic eruptions. *Geophysical Research Letters* 19(8):765–768
- Yamada T, Aoyama H, Nishimura T, Iguchi M, Hendrasto M (2017) Volcanic eruption volume flux estimations from very long period infrasound signals. *Geophysical Research Letters* 44(1):143–151, DOI 10.1002/2016GL071047